UNIVERSITÀ DEGLI STUDI DI PALERMO
Corso di DOTTORATO DI RICERCA in FISICA APPLICATA –
Indirizzo a) Fisica Applicata – Internazionale
Dipartimento di Fisica e Chimica
SSD: Fis02

NOISY DYNAMICS IN LONG AND SHORT JOSEPHSON JUNCTIONS

IL DOTTORE
CLAUDIO GUARCELLO

IL COORDINATORE
BERNARDO SPAGNOLO

IL TUTOR
BERNARDO SPAGNOLO

CO TUTOR
ANDREY PANKRATOV

CICLO XXV
2015

UNIVERSITÀ DEGLI STUDI DI PALERMO

Contents

Abstract

The study of nonlinear dynamics in long Josephson junctions and the features of a particular kind of junction realized using a graphene layer, are the main topics of this research work. The superconducting state of a Josephson junction is a metastable state, and the switching to the resistive state is directly related to characteristic macroscopic quantities, such as the current the voltage across the junction, and the magnetic field through it. Noise sources can affect the mean lifetime of this superconducting metastable state, so that noise induced effects on the transient dynamics of these systems should be taken into account. The long Josephson junctions are investigated in the sine-Gordon framework, stressing the relations beetwen nonlinear excitations travelling into the medium and switching dynamics towards the resistive state. Nonlinear travelling wave solutions of the sine-Gordon equation are solitons and antisolitons (and their combinations), breathers and plasma waves.

The effect of a non-Gaussian noise source is considered, by changing peculiar system parameters, such as the junction length or the frequency and the amplitude of an applied oscillating bias current, and features of the noise sources, such as the amplitude and the statistic of the stochastic signal. *Fortran* codes are implemented to integrate the nonlinear stochastic differential equations for the order parameter of these systems. Typical noise induced effects, such as the noise enhanced stability and the resonant activation, are evident exploring the mean switching time from the superconducting regime, as a function of the noise amplitude and driving frequency, respectively. Attention is given to the soliton evolution in connection with the escape dynamics from the superconducting metastable state. Moreover, noise induced breathers are detected. Breathers are special solutions of the sine-Gordon equation, composed by a coupled soliton-antisoliton pair, oscillating in an internal frame with a proper frequency. These solutions are highly unstable, and their detection in long Josephon junctions is an open challenge.

The possibility to generate only breathers into a junction properly excited is the main focus of the second part of this work. The phenomenon of nonlinear supratransmission in long Josephson junction stimulated by an external signal is analyzed. In correspondence of precise combinations of values of amplitude A and frequency ω of the external sinusoidal pulse, the generation of only breathers emerges. Variations of the pulse durations, both of the applied bias current and of the damping parameter affect the localizations of breathers on a (A, ω) 2D parametric space. The robustness of the generated breathers is tested inserting into the model a thermal noise source to mimic the environmental influence.

The last part of this work deals with the characteristics of a Josephson junctions designed suspending over a graphene layer two superconducting electrodes. The resistively and capacitively shunted junction model is used to analyze the dynamics of this system, including the Josephson current affected by the graphene. The mean escape times under the influence of a colored noise source are calculated varying the noise intensity and driving frequency, and setting different values of the mean bias current. Noise enhanced stability characterizes the mean escape times as a function of the noise intensity. Dynamic

and stochastic resonant activation effects can be clearly distinguished in different noise amplitude ranges. A complete probability density function analysis shades light on the features and the details of all these noise induced effects. The experimental implications of this work are finally discussed, togheter with its possible future developments.

Acknowledgements

This work is the result of three years of study, collaborations, challenges and many people contributed to its successful realization.

The first thanks is for my tutor, professor Bernardo Spagnolo, to gave me the opportunity to attend this PhD, to discover new scientific topics, to produce the scientific publications related to this work and to enlarge my international perspective. I thank him to the priceless opportunity to know and come in contact with foreign cultures, to start and carry on the International russian PhD.

I wish to thank doctor Davide Valenti for the support, for the fruitfull discussions and for the incomparable opportunities to go deeply in every questions, arguments or curiosity regarding my work in these years.

A very special thanks to my colleague and friend, Luca Magazzú, for the stimulating discussion (scientific and not), for the moments spent in good company during my PhD course and for a lot of other aspects of this experience.

I wish to thank my Russian friends, Anna, Irina and Ekaterina. I was really lucky in gaining first three wonderful friends and then three colleagues. Thank You.

I wish to thank professor Alexander Dubkov for his hospitality and helpfulness during my russian journey.

I wish to strongly thank the professor Alexey Ustinov, Kirill Fedorov and the KIT "Karlsruhe Institute of Technology" for the hospitality at the laboratory of Professor Ustinov in the spring of 2013, where the original idea developed in the 3th chapter of my thesys has been developed.

I wish to thank my family, that allow me to complete these years of study and for the support provided me in every moment of my life.

I wish to thank Pierpaolo and Daniela, for the help, the friendship and support they use to provide me whenever I need.

A special thank to Giovanna and Luisa, thanks for a lot of reasons, too many to list in a few words. Is not easy to find friendships so true nowadays.

I wish to thank a lot of friends and relatives (really a lot, too many to mention here without fill many pages), that contributed in these years to joyful and happy my life.

List of Figures

List of Tables

Glossary of acronyms

BCS	-	Bardeen, Cooper and Schrieffer
CL	-	Cauchy-Lorentz
CΦR	-	Current Phase Relation
FBG	-	Forbidden Band Gap
G	-	Gaussian
JJ	-	Josephson Junction
K-A	-	kink-antikink
KG	-	Klein-Gordon
LJJ	-	Long Josephson junction
LS	-	Lévy-Smirnov
MFPT	-	Mean First Passage Time
MQT	-	Macroscopic Quantum Tunneling
MST	-	Mean Switching Time
NES	-	Noise Enhanced Stability
NLRT	-	Non Linear Relaxation Time
NST	-	Nonlinear SupraTransmission
OU	-	Ornstein-Uhlenbeck
PDF	-	Probability Density Function
RA	-	Resonant Activation
RCSJ	-	Resistively and Capacively Shunted Junction
RMS	-	Root Mean Square
SD	-	Standard Deviation
SG	-	sine-Gordon
SGS	-	Superconductor-Graphene-Superconductor
SIS	-	Superconductor-Insulator-Superconductor
SJJ	-	Short Josephson junction
SNS	-	Superconductor-Normal conductor-Superconductor
SQUID	-	Superconducting Quantum Interference Device
ST	-	Switching Times
TA	-	Thermal Activation
VCO	-	Voltage Controlled Oscillator

Glossary of mathematical terms

Chapter 1

ω_c	-	characteristic frequency
I_c	-	critical current
$T^{\star}_{CO}$	-	crossover temperature
Φ_0	-	fluxon
t_{ox}	-	interlayer thickness
I_{φ}	-	Josephson current
λ_J	-	Josephson penetration depth
L	-	lenght of the junction
$\lambda_{L_{1,2}}$	-	London penetration depths
β	-	McCumber parameter
C	-	Normal capacitance of the junction
R_N	-	Normal resistance of the junction
φ	-	phase - order parameter
ω_P	-	plasma frequency
ω_{p_0}	-	plasma frequency in absence of applied bias current
V	-	potential difference across the junction
$\bar{c}$	-	speed of light in the medium
U	-	washboard potential

Chapter 2

A	-	amplitude of the oscillating bias current
$i_b(x,t)$	-	bias current
$i_b(x)$	-	bias current - initial slope
i_0	-	bias current - initial slope, constant value
ω_c	-	characteristic frequency
I_c	-	critical current
$T^{\star}_{CO}$	-	crossover temperature
E_b	-	energy of a breather
E_s	-	energy of a soliton
$i_f(x,t)$	-	fluctuating current density
Φ_0	-	fluxon
ω_b	-	frequency of breathers
ω	-	frequency of the oscillating bias current
$i_T(x,t)$	-	Gaussian thermal noise source
L_P	-	inductance per unit lenght
γ	-	intensity of noise
γ_{CL}	-	intensity of Cauchy-Lorentz noise
γ_G	-	intensity of Gaussian noise

t_{ox} - interlayer thickness
$\mathcal{H}_{\mathrm{SG}}$ - Hamiltonian density (sine-Gordon)
H - Hamiltonian (sine-Gordon)
I_{φ} - Josephson current
λ_J - Josephson penetration depth
$\mathcal{L}_{\mathrm{KG}}$ - Lagrangian density (Klein-Gordon)
$\mathcal{L}_{\mathrm{SG}}$ - Lagrangian density (sine-Gordon)
L_c - lenght of the critical nucleus
L - lenght of the junction
β - Lévy distribution - asymmetry parameter
σ - Lévy distribution - shape parameter
μ - Lévy distribution - shape parameter
α - Lévy distribution - stability parameter
$\lambda_{L_{1,2}}$ - London penetration depths
γ_{ℓ} - Lorentz factor
t_{MAX} - maximum time
β - McCumber parameter
τ - mean first passage time
$i_{nG}(x,t)$ - non-Gaussian noise source
C - normal capacitance of the junction
R_N - normal resistance of the junction
Γ - normalized external magnetic field
N_{cells} - number of cells
N - number of numerical realizations
φ - phase - order parameter
$\Delta U^{\pm}$ - potential barrier heights
$\overline{\Delta U}$ - potential barrier heights - time average
$P(t)$ - probability that $\varphi \in [-\pi, \pi]$
P_{ij} - probability that in the ith realization for the jth cell $\varphi \in [-\pi, \pi]$
R_P - resistance per unit lenght
ω_{thr} - threshold frequency for trapping phenomena
U - washboard potential
W - width of the junction

Chapter 3

i_b - bias current
B_s - bifurcation threshold - continuous chain
$\widetilde{B}_s$ - bifurcation threshold - continuous chain, refined expression
A_s - bifurcation threshold - discrete chain
C - coupling factor
γ - damping parameter
$\sigma_{\overline{\varphi}}$ - dispersion of the φ of a reference cell from their average value
$A(t)$ - driving amplitude
ω - driving frequency
E_i - energy injected into the system
$i_{TN}(x,t)$ - Gaussian thermal noise source
T_{max} - maximum observation time
L_{max} - maximum distance covered by a breather in a time $t \to \infty$
C - Normal capacitance of the junction

R_N - Normal resistance of the junction
φ - phase - order parameter
φ_b - phase of a breather
u_n - phase of the nth oscillator of a discrete SG chain
ω_P - Plasma frequency
$f(t)$ - pulse
T_{exp} - pulse duration
$v(t)$ - velocity of a breather
v_0 - velocity of a breather, initial value
$\overline{\varphi}_{x_{ref}}$ - time average of φ of a reference cell
σ - width of the Gaussian envelopes of the pulse

Chapter 4

A - amplitude of the oscillating bias current
$i_b(t)$ - bias current
i_0 - bias current - initial slope, constant value
$i_b^{\pm}$ - bias current - maximum and minimum values
ω_c - characteristic frequency
τ_c - correlation time
I_c - critical current
T_c - critical temperature
$T_{CO}^{\star}$ - crossover temperature
t^{esc} - escape times
Φ_0 - fluxon
$\omega_{dRA}^{i_0}$ - frequency of the dynamic RA minimum for a specific i_0 value
$\omega_{sRA}^{i_0}$ - frequency of the stochastic RA minimum for a specific i_0 value
ω - frequency of the oscillating bias current
ω_{NES} - frequencies setting which NES effect occurs
β_J - Johnson parameter
E_{J0} - Josephson coupling energy
L - linear dimension of the device
W - linear dimension of the device
m - mass of the phase particle
t_{MAX} - maximum time
τ - mean first passage time
γ - noise amplitude
γ^c - noise amplitude - McCumber approach
γ^p - noise amplitude - Johnson approach
$\gamma_{sRA}^{i_0}$ - noise amplitude at which stochastic RA emerges, for a specific i_0 value
C - Normal capacitance of the junction
R_N - Normal resistance of the junction
N - number of numerical realizations
T_p - period of oscillation of the washboard potential
ω_P - plasma frequency
ω_{p_0} - plasma frequency in absence of applied bias current
$\omega_P^{i_0}(i_b^{\pm})$ - plasma frequency, for highest and lowest slopes of U, for a specific i_0
$\omega_P(t)$ - plasma frequency, time variation
φ - phase - order parameter
$P\left(t^{esc}\right)$ - PDFs of the switching times

i_f	-	stochastic noise current
ξ	-	superconducting coherence length
Δ_0	-	superconductive excitation gap
i_φ	-	supercurrent
β_C	-	Stewart-McCumber parameter
T	-	temperature
$\omega_{thr}^{i_0}$	-	threshold frequency, for a specific i_0 value
U	-	washboard potential - conventional junction
$\widetilde{U}$	-	washboard potential - graphene junction

Physical constants

Boltzmann constant	k_B	=	$1.380\ 650 \times 10^{-23}$ JK^{-1}
Elementary charge	e	=	$1.602\ 176\ 49 \times 10^{-19}$ C
Euler number	e	=	2.718 281 828 ...
Magnetic flux quantum	Φ_0	=	$2.067\ 833\ 667 \times 10^{-15}$ Wb
Planck constant	h	=	$6.626\ 068\ 96 \times 10^{-34}$ Js
Reduced Planck constant	$\hbar$	=	$1.054\ 571\ 63 \times 10^{-34}$ Js
Speed of light	c	=	299 792 458 ms^{-1}
Vacuum dielectric constant	ϵ_0	=	$8.854\ 187\ 817 \times 10^{12}$ Fm^{-1}
Vacuum magnetic permeability	μ_0	=	$4\pi \times 10^{-7}$ NA^{-2}

Chapter 1

Introduction

This chapter contains a brief overview on the general features of a Josephson junction, superconductivity and applications in quantum computing. The state of the art of noisy out-of-equilibrium dynamics of short and long JJs affected is also presented. This is the main focus of this work.

1.1 The Josephson junctions: the transient dynamics

During last decades the interest in superconductor physics and its applications has had a remarkable development. In this context, an important role is played by improvements made in devising and realizing Josephson junction (JJ) based devices. In fact, great attention has been paid to JJs as superconducting quantum bits [21–24], nanoscale superconducting quantum interference devices for detecting weak flux changes [25, 26], and threshold noise detectors [27–30]. Moreover JJs are typical out-of-equilibrium systems characterized by tilted or switching periodic potentials [7, 10, 31, 32]. The behavior of these systems is strongly influenced by environmental perturbations, and specifically by the presence of noise source responsible for decoherence phenomena [22, 33]. The role played by random fluctuations in the dynamics of these devices has recently solicited a large amount of work. Specifically, the investigation both on the effects of thermal and non-thermal noise sources on the transient dynamics of Josephson junctions [34–39] has recently attracted a lot of attentions. The noise current signal is caused by the stochastic motion of the charge carriers, namely the Cooper pairs in a superconductor. While thermal noise is originated by the thermal motion of the charge carriers, non-thermal noise signal is related to their scattering and transmission. Non-Gaussian noise appears when the conductor, or the superconductor, is in a non-equilibrium state because of the presence of a bias voltage or external current. The JJ behaviour can be depicted as the motion of a fictitious Brownian "phase particle" rolling down on a tilted potential, called the *washboard potential* (see Fig. 1.1), composed by a sequence of wells. The position of this phase particle along the potential profile, or, more precisely, its dynamical regime, defines the working regime of the junction. In the *superconducting state* the particle lies in a well, while in the *resistive state* it rolls down along the potential. When this happens, a non zero mean voltage V across the junction appears, according to the *a.c. Josephson relation*. The dynamics of this particle is also affected by dissipative factors, so that a *phase diffusion* (PD) state, that is an escape event combined with a subsequent retrapping in the first next minimum, can be established. The switching dynamics from the superconducting state can be driven by a force applied on the system, i.e. a polarization current, or by the stochastic fluctuations due to environmental interactions.

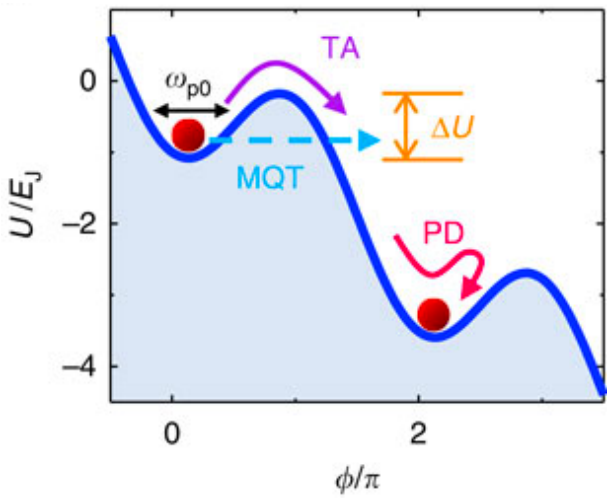

Figure 1.1: Schematic of washboard potential $U(\phi)$, normalized by the Josephson coupling constant E_J (ϕ is the phase difference across the JJ), and dynamics of a phase particle escaping from the local potential minimum (PD, phase diffusion; TA, thermal activation; MQT, macroscopic quantum tunnelling).

Two different mechanisms can cause the noise-induced crossing of a potential barrier: the macroscopic quantum tunneling (MQT) or the thermally activated (TA) escape. These processes are triggered in distinct ranges of temperature, so that a threshold value exists, the *crossover temperature* for zero bias and damping $T_{CO} = \hbar\omega_{p_0}/2\pi k$ (k is the Boltzmann constant). The frequency ω_{p_0} is a parameter characterizing a junction, called the JJ plasma frequency, representing the oscillation frequency in the bottom of a potential well. In a damped system, when a polarization current is applied, this value is slightly reduced, becoming [40]

$$T^{\star}_{CO} = \hbar\omega_R/2\pi k$$

where $\omega_R = \omega_{p_0}\left\{\sqrt{1+\alpha^2} - \alpha\right\}$, $\alpha = (2\omega_P R_N C)^{-1}$ (R_N and C are the normal resistance and the capacitance of the junction). For temperatures below this threshold the system undergoes a *quantum tunneling regime*, otherwise the system works in the *thermal activation regime*. In this latter condition and neglecting thermal fluctuations, the phase can remarkably change merely when the polarization current approaches and overcomes the critical value (the system go into a resistive regime). Conversely, considering noise effects, transitions along the potential can also occur applying a current smaller then the critical one. The phase dynamics is affected by dissipative phenomena, responsible for peculiarities of the system, ranging from overdamped (high viscosity) to underdamped (low viscosity) condition. In light of this, one can talk about metastable states, switching events and transient dynamics studying the current-voltage characteristic of a JJ.

1.2 Superconductivity and Josephson effects

A JJ is made by sandwiching a thin layer of a non-superconducting material between two layers of superconducting material. The devices are named after Brian Josephson, who predicted in 1962 [41] that pairs of electrons, called Cooper pairs, can "tunnel" right through the nonsuperconducting barrier from one superconductor to another. He also predicted the exact form of the current and voltage relations for the junction. In particular, the carriers in the left and right superconductors forming a junction can be

described by

$$\begin{aligned} \psi_{_L} &= \sqrt{\rho_{_L}}\, e^{i\theta_{_L}} \\ \psi_{_R} &= \sqrt{\rho_{_R}}\, e^{i\theta_{_R}} \end{aligned} \tag{1.1}$$

in which $\theta_{_{L,R}}$ and $\rho_{_{L,R}}$ are the wave functions phases and carriers densities of the coupled superconductors. Defining the phase difference

$$\varphi = \theta_{_R} - \theta_{_L}, \tag{1.2}$$

the well-known *Josephson Equations* can be derived:

$$I_\varphi = I_c \sin(\varphi) \tag{1.3}$$

$$\tag{1.4}$$

$$\frac{d\varphi}{dt} = \frac{2eV}{\hbar} \tag{1.5}$$

where I_φ is the Josephson current, I_c is the critical current, e is the electron charge, $\hbar$ is the reduced Planck constant and V is the potential difference across the junction. These relations tell us that also without voltage applied to the junction, i.e. $V = 0$, a costant phase difference can be established, therefore a finite supercurrent can flow through the junction. This is the core of the *d.c. Josephson effect*, first experimentally observed in 1963 [42]. Instead, as a result of a non-zero costant potential difference the phase difference will grow linearly in time, i.e. if $V \equiv V_0$ then $\varphi(t) = \varphi_0 + (2e/\hbar)V_0 t$ and a current, oscillating with a frequency $2eV/\hbar$, appears. This is known as the *a.c. Josephson effect*. Experimental works proved that Josephson was right, so that he was awarded the 1973 Nobel Prize in Physics for his work.

To understand the unique and important features of JJs, it is first necessary to understand the basic concepts and features of superconductivity. Cooling many metals and alloys to very low temperatures (with temperature $T < 20°K$), a phase transition occurs. At this "critical temperature", the metal goes from what is known as the normal state, where it has electrical resistance, to the superconducting state, where there is essentially no resistance to the flow of direct electrical current. The newer high-temperature superconductors, which are made of ceramic materials, exhibit the same behavior but at higher temperatures, ranging from $40°K$ to $190°K$ [43]. What occurs is that the electrons in the metal become paired, forming the so-called "Cooper pairs", according to the work of Bardeen, Cooper and Schrieffer in 1957 (BCS theory) [44]. Above the critical temperature, the net interaction between two electrons is repulsive. Below the critical temperature, though, the overall interaction between two electrons becomes very slightly attractive, a result of the electronic interaction with the ionic lattice of the metal.

This very slight attraction allows them to drop into a lower energy state, opening up an energy "gap". Because of the energy gap and the lower energy state, electrons can move (and therefore current can flow) without being scattered by the ions of the lattice, which leads to electrical resistance in metals. Therefore, there is no electrical resistance in a superconductor, and therefore no energy loss. There is, however, a maximum supercurrent that can flow, called the critical current. Above this critical current the material is normal. There is another very important property: when a metal goes into the superconducting state, it expels all magnetic fields, as long as the magnetic fields are not too large. In a JJ, the nonsuperconducting barrier separating the two superconductors must be very thin. If the barrier is an insulator, its thickness has to be

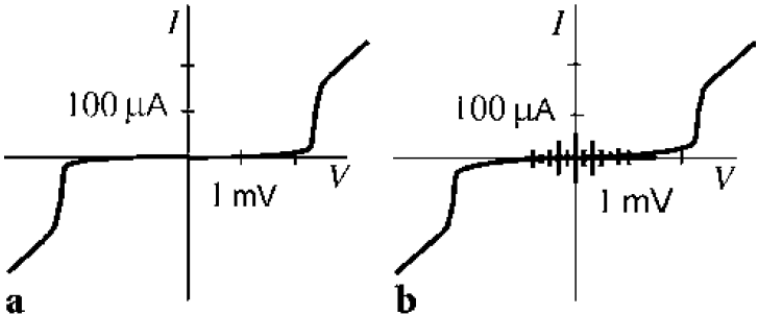

Figure 1.2: Dc currentvoltage characteristic of Nb/Al2O3/Nb trilayer Josephson tunnel junction at 4.2K. Note the supercurrent in the zero-voltage state and the steep gap structure near 2.7 mV. (a) No applied microwaves and (b) with applied microwaves. The small vertical zero-crossing steps are equally spaced with a voltage difference of $\Delta V = hf/2e$. These nonlinear quantum phenomena allow for the practical construction of the Josephson voltage primary standard. Figure adpated from [1].

of the order of 30 Å or less. If the barrier is another metal (nonsuperconducting), it can be as much as several microns thick. Until a critical current is reached, a supercurrent can flow across the barrier; electron pairs can tunnel across it without any resistance. So, as long as the current through the junction is less than the critical value, the voltage is zero. When the current exceeds the critical current, the voltage is not zero but varies in time. Detecting and measuring the change from one state to the other is at the heart of the many applications for JJs. Electronic circuits can be built from JJs, especially digital logic circuitry. Many researchers are working on building ultrafast computers using Josephson logic. JJs can also be fashioned into circuits called SQUIDs–an acronym for superconducting quantum interference device. These devices are extremely sensitive and very useful in constructing extremely sensitive magnetometers and voltmeters. A SQUID consists of a loop with two JJs interrupting the ring, and it is extremely sensitive to the total amount of magnetic field that penetrates the area of the loop. The voltage that can be measured across the device is very strongly correlated to the total magnetic field into the loop.

If the junction is supplied with a constant voltage, V_{DC}, the phase difference steadily increases with time, and the junction current oscillates with the frequency $\nu = V_{DC}/\Phi_0$, that is, the junction works as a voltage controlled oscillator (VCO) that may generate microwave power into the gigahertz range (the pre-factor $1/\Phi_0 \approx 0.5$ GHz/ μV).

The capacitance between the two electrodes shunts the Josephson tunneling and leads to hysteresis in the current-voltage characteristic (I-V curve) as shown in Fig. 1.2. Starting at zero and increasing the bias current, there is a vertical supercurrent (zero-voltage state) up to I_c where the junction switches (horizontally) to the steep so-called quasi-particle curve (near 2.7 mV), which reflects the superconducting gap of the two niobium electrodes. The quasi-particle curve is followed both when the bias current is further increased and when the current is returned to I = 0. The hysteretic I-V curve is pointsymmetric around (V,I)=(0,0).

The I-V curve near the gap is strongly nonlinear and temperature dependent. Tunnel junctions biased close to the knee are used as low-noise bolometers to detect broad band signals in the millimeter, or μm, range. Due to its strong nonlinearity, heterodyne receivers based on this "superconductor-insulator- superconductor"(SIS)-mixer can be operated near the quantum limit ($h\nu \approx k_B T$). The SIS-mixer may be pumped by the microwave signal emitted from a long JJ (see below the descriptions for both long JJ and SIS junction). Most modern radio-telescopes employ SIS-mixers for spectral measurements in the frequency range 10-1000 GHz.

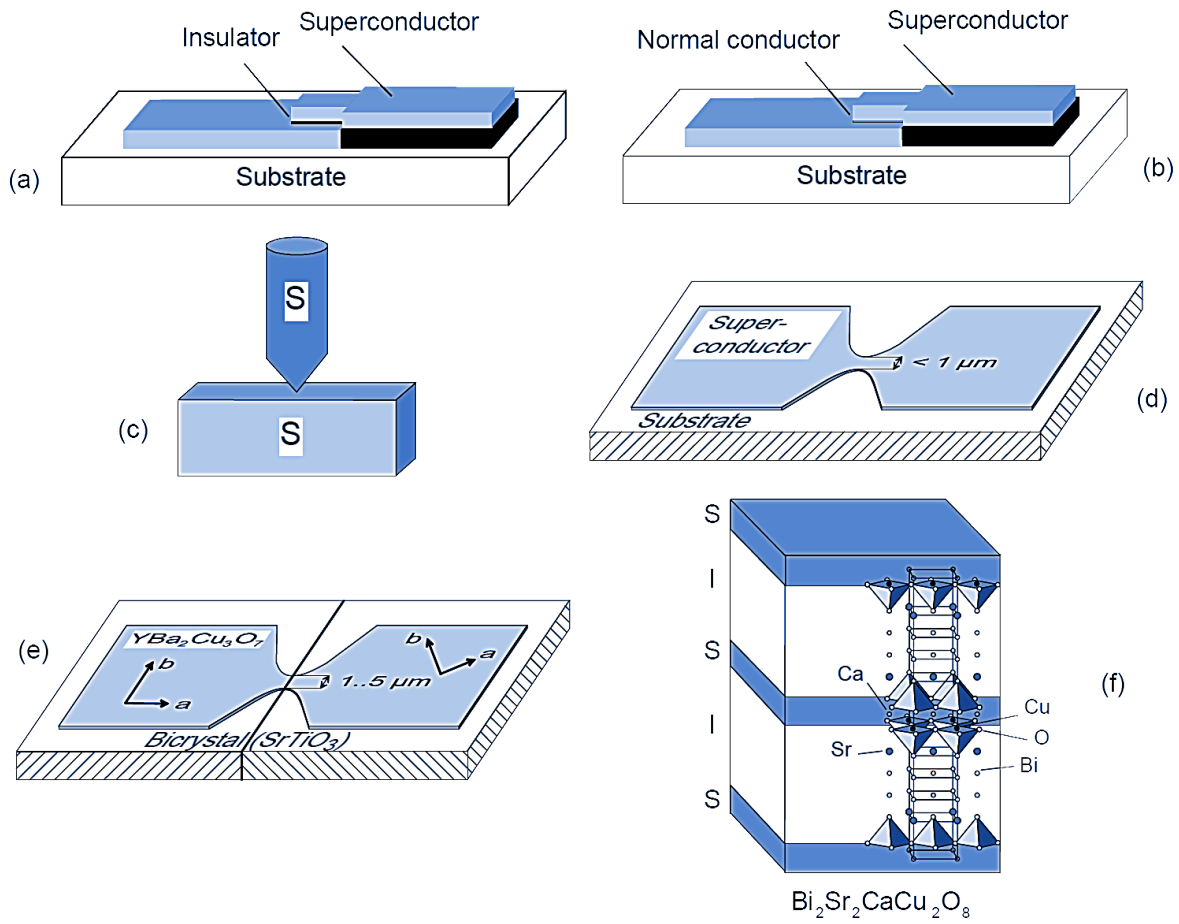

Figure 1.3: Schematics of the different possibilities for producing a weak coupling between two superconductors: (a) SIS junction with an oxide layer as a barrier; (b) SNS junction with a normal conducting barrier; (c) point contact; (d) microbridge; (e) $YBa_2Cu_3O_7$ grain boundary junction; (f) intrinsic Josephson junction in $Bi_2Sr_2CaCu_2O_8$. Figure adpated from [2].

Fig. 1.2 shows the I-V curve when a microwave signal is applied to the junction. The supercurrent is suppressed and small equally spaced replica appear as vertical (Shapiro) steps [45] with a voltage difference of $\Delta V = h\nu/2e$. These zero-crossing steps and the fact that voltage and frequency are related only through fundamental constants allow for the practical realization of the Josephson voltage primary standard. When pumped by a 70 GHz signal, $\Delta V \approx 140\mu$V; thus a small chip with more than 20.000 dc series connected JJs can generate a reference voltage of 10V with an accuracy of 0.1 nV. The stability of the Josephson voltage standard is limited by chaotic behavior [46].

JJs are highly sensitive to magnetic fields. The gradient of the phase difference φ is proportional to the magnetic field applied in the plane of the junction, and for constant current density the φ has a variation of 2π when the flux Φ through the junction is exactly one flux quantum Φ_0. These changes of the phase difference along the junction also lead to the so-called Fiske steps. These are nearly constant-voltage steps in the I-V curve at voltages $V_{\mathrm{FS}n} = n\Phi_0\bar{c}/2L$, where $n = 1, 2, ..., L$ is the junction length perpendicular to the magnetic field and $\bar{c}$ is the speed of light in the medium.

1.3 Types of junctions

A huge variety of junctions exists, depending on the specific application. A simple collection of different type o junction is shown in Fig. 1.3 [2]. The panels (a) and (b) of this figure show a superconductor-insulator-superconductor (SIS) and a superconductor-

normal conductor-superconductor (SNS) junction, respectively. While in the SIS structure the insulating barrier must be only 1-2 nm thick, the SNS can work with a larger normal conductor layer. This is due to the deeper penetration of the Cooper pairs in a metal layer than into an oxide layer. An important difference beetwen these two structures is the value of the resistance per square (normal resistance/area of the barrier). For the SIS junction reanges in $[10^{-3} - 10^{-4}]$ Ωcm^2 and for SNS junction is below 10^{-8} Ωcm^2. More complicated structures exist, e.g. the so-called SINIS junctions. In the point contact junction (panel (c) of Fig. 1.3) a metal tip is pressed on a surface, so that the cross section of the contact depends on the applied pressure. A microbridge (panel (d) of Fig. 1.3) is a narrow constriction limiting the Cooper pairs exchange. Considering high temperature superconductors, grain boundaries can be used as weak coupling regions. $YBa_2Cu_3O_7$ thin film can be deposited on a bicrystal substrate, consisting of two single-crystalline parts joined together at a specific angle. The grain boundary of the substrate is then transferred also into the deposited film, which otherwise is a single-crystalline epitaxially grown (panel (e)). Variations in the grain boundary angles corresponds to variations in the strenght of the Josephson coupling. Intrinsic JJs can be detected in the crystal structure of some high-temperature superconductors, as $Bi_2Sr_2CaCu_2O_8$ (panel (f)). Here the superconductivity is restricted only to the copper oxide layers with about 0.3 nm thickness. Between these layers there are electrically insulating bismuth oxide and strontium oxide planes. Hence, such materials form stacks of SIS JJs, where each junction has a thickness of only 1.5 nm, the distance between two neighboring copper oxide layers [47].

This work is base on the investigation of SNS or SIS junctions, including spatial dependence of the current density through it, referred as *extended* JJs [48]. Discussing the physics of extended JJs, two cases can be distinguished:

- *Short* Josephson junctions:

  in short junctions the magnetic field generated by the Josephson current itself is negligible compared to the externally applied magnetic field. Junctions can be considered as short junctions, if the spatial dimensions of the junction area are smaller than a characteristic length scale named Josephson penetration depth λ_J.

- *Long* Josephson junctions:

  in long JJs the magnetic field generated by the Josephson current itself is no longer negligible. Long JJs have spatial dimensions larger than the Josephson penetration depth λ_J.

The Josephson penetration depth is:

$$\lambda_J = \sqrt{\frac{\hbar c^2}{8\pi e d J_c}} \tag{1.6}$$

and represents the skin portion of the junction edge in which, in d.c. Josephson effect, the Josephson current is confined. In the λ_J expression, J_c is the critical current density, $d = \lambda_{L_1} + \lambda_{L_2} + t_{ox}$, where t_{ox} is the interlayer thickness and $\lambda_{L_{1,2}}$ are the London penetration depths, that is the length scale over which an applied field can penetrate the two superconductors.

1.4 Noise and JJ

During the second half of the twentieth century, the industry of microelectronics has made considerable technological progress, creating new devices and nanoscopic

heterostructues. These have instigated experiments revealing novel quantum effects, originated from the transport of electrons through nanostructures, for example:

- The *Aharonov-Bohm effect*. In quantum mechanics, the electromagnetic potentials have a physical significance and can cause effects on charged particles even in spatial regions where the fields (and thus all the applied electromagnetic forces) are zero [49].

- The *universal conductance fluctuations*. If the length of the system is comparable to the electron coherence length, reproducible conductance fluctuations as a function of an applied magnetic field are observed [50].

- The *quantum Hall effect*. In two-dimensional electron systems at low temperatures and high magnetic fields, the resistance is quantized [51, 52].

- The phenomenon of *weak localization*. In materials with a high density of defects, the resistivity increases due to the quantum interference, e.g. a 2D electron gas becomes insulating in absence of magnetic field as the temperature approaches absolute zero [53].

In quantum transport, there are various physical length scales that, compared to the dimensions of the conductor, establish the nature of transport. The basic scales are the average distances that an electron travels before it:

$\succ$ scatters changing its momentum (*mean free path*) or

$\succ$ scatters inelastically randomizing its phase (*coherence length*).

In terms of these length scales, transport can be characterized as

✓ *diffusive*, if the conductor dimensions are much larger than the mean free path and the coherence length of the electrons, so their initial momentum and phase get changed;

✓ *ballistic*, if the mean free path is larger than the dimensions of the conductor;

✓ *coherent*, if the electrons coherence length is greater than the dimensions of the conductor.

Transport experiments exhibit current and voltage fluctuations. This undesirable 'noise' is often originated from imperfections in the design of the circuit. However, part of the noise is of more fundamental nature, and when that originated from a bad design is sufficiently suppressed, the remaining fluctuations can be used as a powerful tool to learn about electronic properties and different characteristics of the conductor. Let us start by giving a brief description of the fundamental types of noise that may be encountered in a mesoscopic system:

$\triangleright$ **thermal noise** (Johnson-Nyquist noise): at thermodynamic equilibrium and a finite temperature T, the distribution of the number of particles n with a particular energy ε (which is $f = [\exp\{-\frac{\varepsilon}{k_B T}\} + 1]^{-1}$ for fermions) presents a non-vanishing noise value (second cumulant) given by $\left\langle (n - \langle n \rangle)^2 \right\rangle = f(1 - f)$.

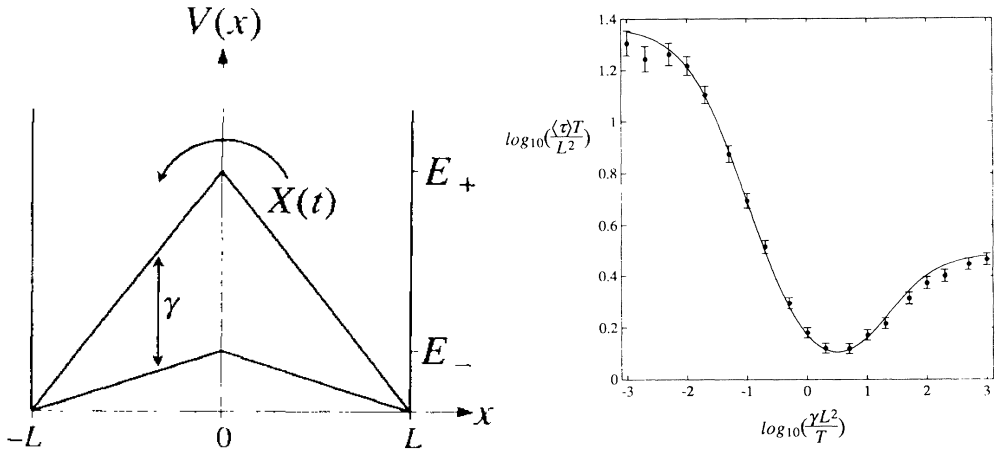

Figure 1.4: a) Barrier configuration of the system studied by Doering and Gadoua [3]. b) Resonant Activation: theoretical curve (solid line) and simulation data (points) of the MFPT vs fluctuation rate of the driving potential [3].

- ▷ **1/f noise** (flicker noise): the nature of this noise is believed to be often related to the random motion of charges trapped in the substrate of the material. This motion is slow compared to other time-scales in the system, what makes the fluctuations to be significant usually below 10kHz.

- ▷ **shot noise** (Schottky noise): this is due to the discrete character of the current, composed of electrons flowing along the conductor. Each of these particles has a wave character, and thus a probability P of being transmitted and $(1-\mathsf{P})$ of being reflected in the process of tunneling through the system. Shot noise may also originate from the random nature in which particles are released from the emitter. In any case, if $\langle n_{\mathsf{P}}\rangle = \mathsf{P}$ is the mean number of transmitted particles, we find $\langle (n_{\mathsf{P}} - \langle n_{\mathsf{P}}\rangle)^2\rangle = \mathsf{P}(1-\mathsf{P})$. Thus, in the tunneling limit ($\mathsf{P} \ll 1$) we have $\langle (n_{\mathsf{P}} - \langle n_{\mathsf{P}}\rangle)^2\rangle \approx \mathsf{P} = \langle n_{\mathsf{P}}\rangle$, that is, the current noise is proportional to the current itself. This Poissonian behaviour was measured by Schottky in 1918 in the process of emission of electrons from a cathode in a vacuum tube. Notice that if electrons are emitted according to the Fermi distribution f, we have $\langle n_{\mathsf{P}}\rangle = \mathsf{P}f$ and thus $\langle (n_{\mathsf{P}} - \langle n_{\mathsf{P}}\rangle)^2\rangle = \mathsf{P}f(1-\mathsf{P}f)$, which reduces to $\mathsf{P}(1-\mathsf{P})$ in the zero-temperature limit.

- ▷ **quantum noise**: This arises from the quantum nature of the emission and absorption processes. First, the spectrum of radiation of the electromagnetic field follows Planck's law. Second, it incorporates vacuum fluctuations. Similarly to the zero-point motion of the quantum harmonic oscillator ($\langle \hat{x}^2\rangle_{\text{vac}} \neq 0, \langle \hat{p}^2\rangle_{\text{vac}} \neq 0$, being $\hat{x}$ and $\hat{p}$ position and momentum, respectively, and the averages taken in the vacuum state), voltage V and current I in an electric circuit present a zero-point variance as well, $\left\langle \hat{V}^2 \right\rangle_{\text{vac}} \neq 0, \left\langle \hat{I}^2 \right\rangle_{\text{vac}} \neq 0$ (which can be understood as inherited from the fluctuations of flux $\hat{\Phi}$ and charge $\hat{Q}$, namely $\left\langle \hat{\Phi}^2 \right\rangle_{\text{vac}} \neq 0, \left\langle \hat{Q}^2 \right\rangle_{\text{vac}} \neq 0$).

1.5 State of the art

Recently various works explored the behavior of long and short JJs analyzing the effect of a stochastic noise source on the switching dynamics from the metastable

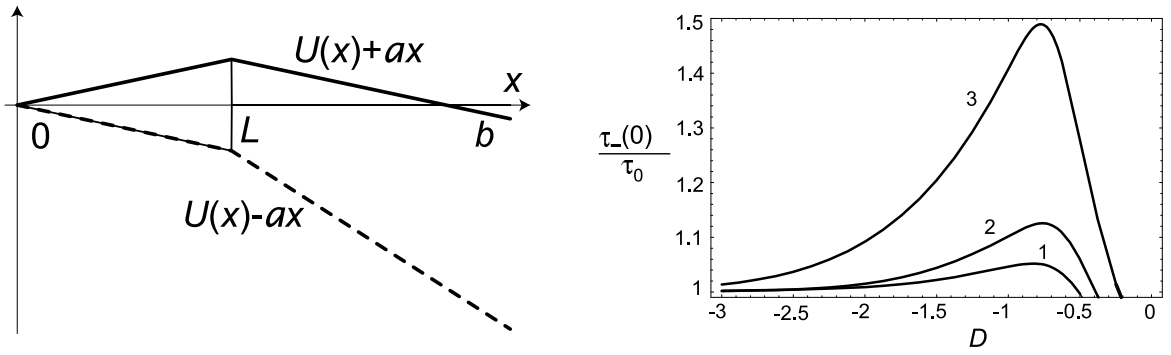

(a) (b)

Figure 1.5: a) Switching piece-wise linear potential [4]. b) Semilogarithmic plot of the MFPT vs the white noise intensity D for three values of the dimensionless driving frequency ω: 0.1 (curve 1), 0.05 (curve 2), 0.01 (curve 3) [4].

superconducting state. Different noise induced phenomena can be highlighted, specially when a random fluctuating potential or effect of an oscillating external driving are considered. The phenomenon called "resonant activation" (RA), first studied by Doering and Gadoua [3], is observed by investigating the problem of thermally activated potential barrier crossing in the presence of fluctuations of the barrier itself. For a piecewise linear barrier, displayed in Fig.1.4a, switching between two values as a Markov process, their results reveal a resonant-like phenomenon as a function of the barrier fluctuation rate. Fig.1.4b shows the average of the first passage time (MFPT) as a function of fluctuation rate of the barrier. For very slow variations the MFPT is the average of the times required to diffuse over each of the barriers separately; for very fast variations the MFPT is that required to cross the average barrier. At intermediate rates the crossing is strongly correlated with the potential variation and the MFPT exhibits a local maximum at a "resonant" fluctuation rate, Fig.1.4b.

Another noise induced effect can result studying the MFPT as a function of the intensity of the noise signal. Counterintuitively, the presence of a stochastic signal can increase the permanence time inside the metastable state respect the deterministic case, and this produce a maximum in the MFPT behavior. This effect was first experimentally observed in a tunnel diode by Mantegna and Spagnolo [54], and it was named "noise enhanced stability" (NES) [4, 54–58]. The dynamics of a Brownian particle in fluctuating piece-wise linear potential, Fig.1.5a, is studied. The MFPT, i.e. how long it take the particle, starting from the the metastable state, to arrive into the point b (abosrbing boundary), as a function of the noise intensity D shows an evident maximum, corresponding to a growing permanence time inside a potential well. This is displayed in Fig.1.5b, for three different values of the driving frequency. All curves are characterized by a non-monotonic behavior expressed by a clear NES effect.

1.5.1 Thermal noise in short JJs

The dynamics of a short overdamped JJ, subjected to a current $i(t)$, was firstly computationally explored by Gordeeva *et al* [5] studying the following Langevin equation:

$$\omega_c^{-1}\frac{d\varphi(t)}{dt} = -\frac{du(\varphi)}{d\varphi} - i_f(t), \tag{1.7}$$

$$u(\varphi) = 1 - \cos(\varphi) - i(t)\varphi, \tag{1.8}$$

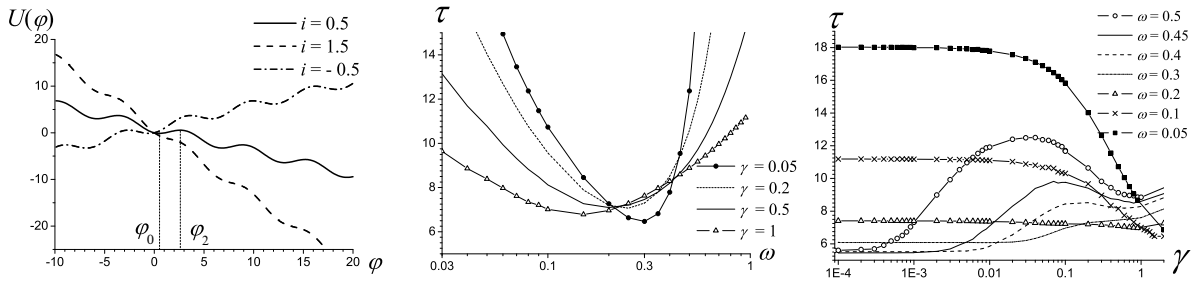

(a) **(b)** **(c)**

Figure 1.6: a) Washboard potential: the extreme positions during the periodical variations (i = -0.5 and i = 1.5), and the intermediate configuration (i = 0.5) are shown [5]. b) MST versus the signal frequency for different values of the noise intensity [5]. c) MST versus noise intensity for seven different values of driving frequencies [5].

where φ is the phase difference (see the Eq.1.2), $u(\varphi)$ is the dimensionless washboard potential (see Fig.1.6a), $\omega_c = 2eR_N I_c/\hbar$ is the characteristic frequency of the JJ. Here $i(t) = I(t)/I_c = i_0 + f(t)$ is the total current across the junction, where i_0 is the constant bias current and $f(t)$ is the driving signal. Moreover $i_f(t) = I_f(t)/I_c$ is a normalized stochastic signal that, due to the thermal fluctuations, may be represented by white Gaussian noise

$$\langle i_f(t)\rangle = 0, \qquad \langle i_f(t) i_f(t+\tau)\rangle = \frac{2\gamma}{\omega_c}\delta(\tau), \tag{1.9}$$

where $\gamma = 2ekT/\hbar I_c = I_T/I_c$ is the dimensionless intensity of fluctuations, T is the temperature and k is the Boltzmann constant. Initially, the JJ is biased with a current across the junction smaller than the critical one, that is $i_0 = (I_0/I_c) < 1$, and the location of the phase in a potential minimum, $\varphi_0 = \arcsin(i_0)$, is taken as the initial condition. A current signal $f(t)$, such that $i(t) > 1$, switches therefore the junction into the resistive state. In Fig.1.6a the periodical potential profile of the JJ and its extreme positions within which it varies in time are displayed. The switching occurs not immediately, but at a later time, i.e switching time that, due to the noise, is a random quantity. Therefore the mean switching time (MST) τ is explored. The used driving signal is $f(t) = A\sin(\omega t)$, where ω is the oscillation frequency and A is the signal amplitude. In Fig.1.6b the MST is shown versus the signal frequency ω for different values of the noise intensity, and the RA phenomenon is clearly evident. A frequency range, from 0.2 to 0.4, where the MST grows by increasing the noise intensity is evident. By increasing the noise intensity, the probability of the thermal activated switching increases and, as a result, the MST decreases. In the interval $0.2 < \omega < 0.5$ the NES effect appears (see Fig.1.6c) and the behavior of the MST vs γ curves, becomes non-monotonic in contrast with the cases with $\omega < 0.2$. Due to the periodic variation of the potential profile, the particle starting from the minimum reaches a position near the top of the barrier. An enhancement of the lifetime of the metastable state produces an enhancement of the mean switching time. By increasing the noise intensity the thermally activated escape increases too and the MST decreases. Taking a cue from these results, Augello *et al* [6, 59] studied the effects of a colored noise source on the transient dynamics of short JJs. They explored the Langevin equation 1.7, inserting however the colored noise source modelized using

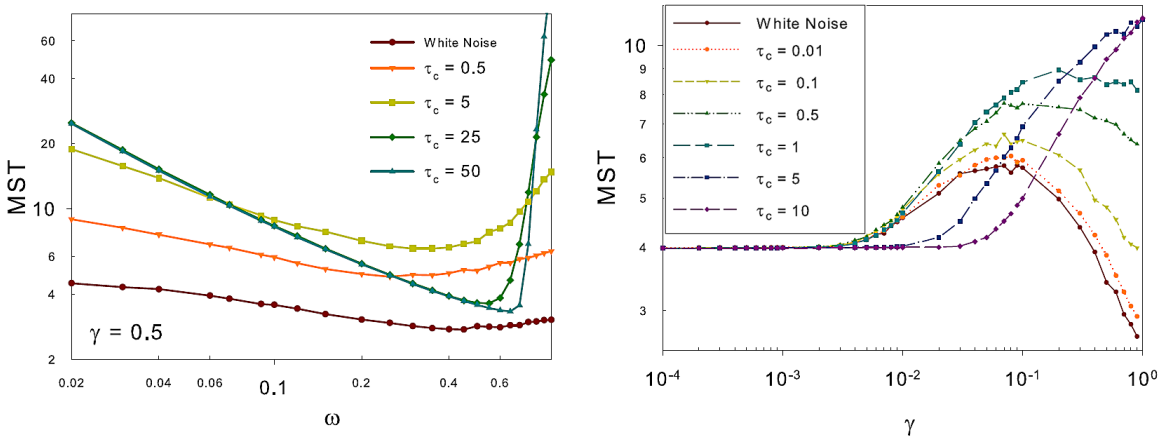

Figure 1.7: a) MST versus the driving frequency ω, with evidence of the RA minimum. b) MST versus the noise intensity γ, with evidence of the maximum. [6, 7]

an Ornstein-Uhlenbeck (OU) process

$$\frac{d\phi}{dt} = -\omega_c \frac{dU(\phi)}{d\phi} - \omega_c \zeta(t), \tag{1.10}$$

$$d\zeta(t) = -\frac{1}{\tau_c}\zeta(t)dt + \frac{\sqrt{\gamma}}{\tau_c}dW(t) \qquad \langle \zeta(t)\zeta(t')\rangle = \frac{\gamma}{2\tau_c} e^{-\frac{|t-t'|}{\tau_c}} \tag{1.11}$$

They studied the mean lifetime in the superconductive state as a function of the driving frequency ω and the noise amplitude γ, varying the correlation time of the OU noise source τ_c. In Fig.1.7a the behavior of MST vs ω is reported for different values of τ_c. The non-monotonic behavior of the curves shows that the RA phenomenon appears also with colored noise. The values of MST around the minimum are influenced by the variation of τ_c, more strongly for higher values of the noise intensity. Moreover, for higher intensity values, they find, in a wide range of frequency ($0.3 < \omega < 0.8$), a non-monotonic behavior of MST as a function of the correlation time. In Fig.1.7b, the behavior of MST as a function of the noise intensity, for different values of the correlation time, is displayed. The appearance of noise enhanced stability (NES), a phenomenon already found in short JJs in the presence of white noise, is found. They observed a range of values of correlation time, namely $0.01 < \tau_c < 1$, in which the curves present a non-monotonic behavior. For τ_c=[5, 10], the non-monotonic behavior disappears.

Both resonant activation and noise-enhanced stability were experimentally observed in underdamped JJs by Sun *et al* [8]. Their numerical simulations, which include a driving current signal and thermal fluctuations, show good agreement with the experimental results. The switching times from the metastable superconducting state were measured and collected to calculate the MST. The escape time was measured using the time-domain technique shown in Fig.1.8a. For each escape event, the measurement cycle started by ramping up the bias current to a value I_b, which was very close to I_c, and maintaining it at this level for a period of waiting time. A sinusoidal current with amplitude $2i_{ac}$ was added to I_b during the waiting time, so that $I_b + 2i_{ac} < I_c$ and the junction was still in a metastable state. The junction voltage was connected to a timer, which was triggered by the sudden voltage jump when the junction, because of thermal fluctuations, switched from zero-voltage state to finite voltage-state, to record the escape time t_{esc}. The bias current I_b was then decreased to zero, returning the junction to the zero voltage state. The process was repeated to obtain an ensemble of the escape time. The average time of

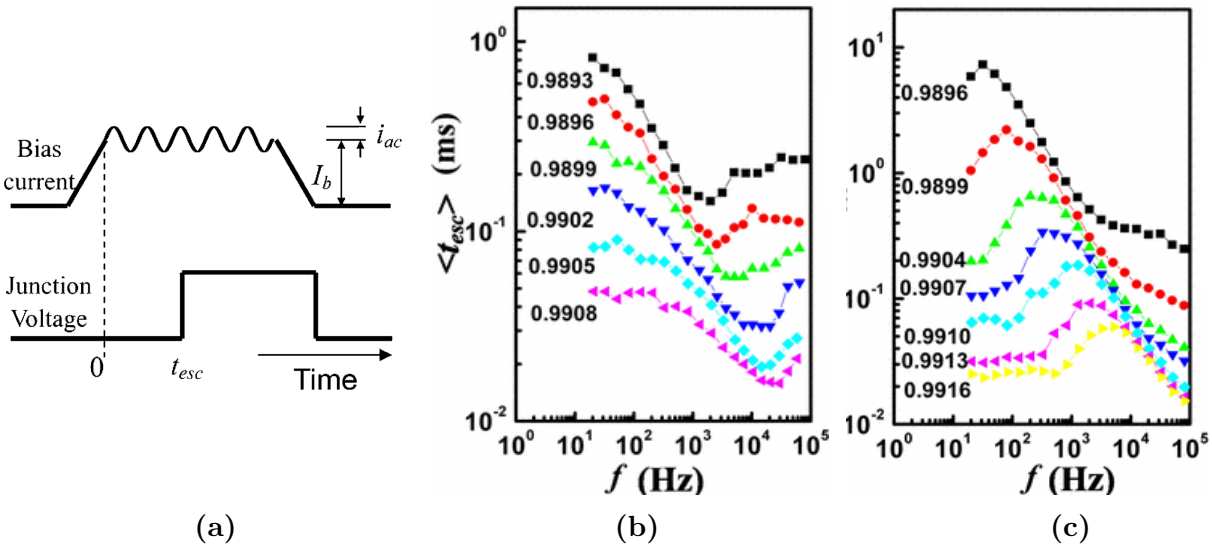

Figure 1.8: (a) Schematic time profile for measuring the escape time of a JJ subjected to a weak sinusoidal force. (b) and (c) MST as a function of the driving frequency at 4.2 K for various normalized bias currents which are marked below the curves. The initial phases were $\varphi_0 = 0$ (b) and $\varphi_0 = \pi$ (c). [8]

the ensemble represented the mean thermal activation escape time $\langle t_{esc} \rangle$. Then, another $\langle t_{esc} \rangle$ was measured changing the frequency of the driving current. In Fig.1.8b $\langle t_{esc} \rangle$ as a function of the driving frequency f is reported for different values of the bias current I_b. The RA phenomenon is evident and a minimum in correspondence of a resonant frequency is present for each value of the bias current. The curves of Fig.1.8b were obtained for zero initial phase of the particle $\varphi_0 = 0$. By gradually changing the initial phase, the minimum of the curves vanishes. When initial phase is gradually changed the minimum of the curves vanishes. Moreover, for $\varphi_0 = \pi$ resonant peaks are present at different resonance frequencies, as shown in Fig.1.8c. The junction actually has a longer average escape time than that observed without periodical driving force, corresponding, in Fig.1.8c, to $\langle t_{esc} \rangle$ at very low frequency. Therefore, the noise enhances the stability of the metastable state in the observed frequency domain, in agreement with the theoretical results previously obtained in Ref. [4].

Experimental evidence of RA effect was achieved also by Pan *et al* [9] by study, in short underdamped JJs, the behavior of a thermal noise current signal. They defined, to overcome the problem associated to the experimental control of the fluctuating current i_f, an effective temperature T_{eff} related to a white noise current. They realized a practical method to manage an oscillating effective temperature in a JJ. First, they considered an additional white noise current $I'_n(t)$, so that the correlation function of the total noise current I_{ns} defines T_{eff}

$$\langle I_{ns}(t) I_{ns}(t') \rangle = \frac{2k_B T_{eff}}{R} \delta(t - t'),$$

where R is the equivalent resistance of the JJ and $T_{eff} = T + RI_\sigma^2/2k_B$. The term I_σ is defined by the autocorrelation function of the additional white noise $\langle I'_n(t) I'_n(t') \rangle = I_\sigma^2 \delta(t - t')$. Therefore T_{eff} can be adjusted by tuning I_σ. Furthermore, the behavior of the measured switching current distribution is identical to that obtained by changing the bath temperature. To measure the MST, the time-domain technique described in Fig.1.8a was used. During the waiting time, a white noise signal with frequency f is periodically added to make the system fluctuating between two effective temperatures, as shown in Fig.1.9a. Figs. 1.9b and 1.9c show the MST as a function of the driving frequency,

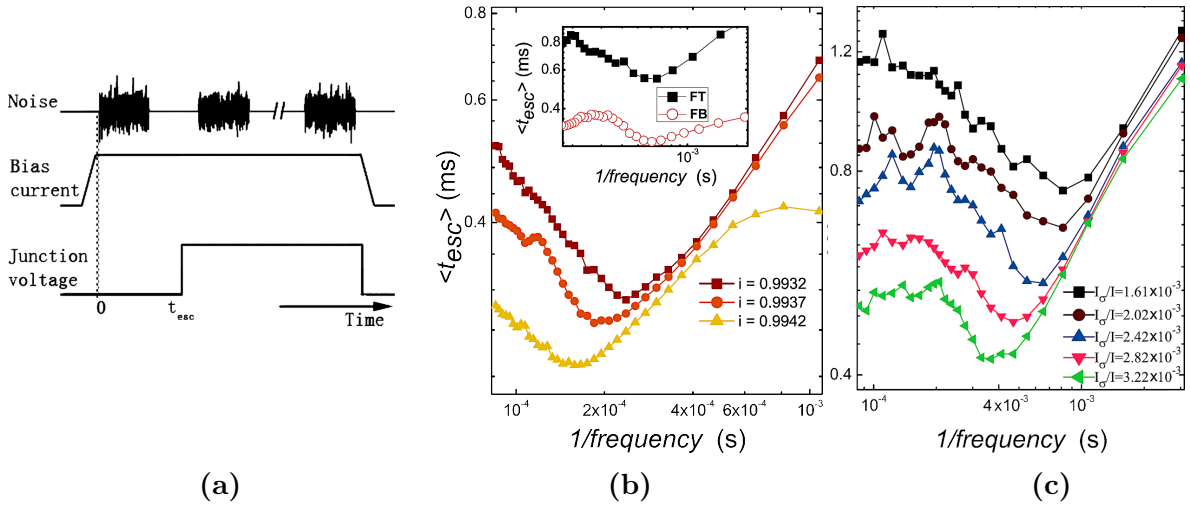

Figure 1.9: (a) Schematic time profile for measuring the escape time of a JJ with presence of an oscillating white noise. (b) $\langle t_{esc} \rangle$ as a function of characteristic time of temperature fluctuation $1/f$ for different bias current I and setting $I_\sigma = 0$. Inset: $\langle t_{esc} \rangle$ as a function of the characteristic time of barrier fluctuation for flactuating temperature (FT) and flactuating barrier (FB). (c) $\langle t_{esc} \rangle$ vs $1/f$ for various I_σ's (normalized to I). [9]

obtained, respectively, setting $I_\sigma = 0$ and changing the bias current (see Fig.1.9b) and varying the I_σ values, i.e. varying T_{eff}, and setting the bias current (see Fig.1.9c). The results highligth RA effects in presence of fluctuating barrier and temperature. As T_{eff} increases the RA valleys get deeper and narrowed, and the minima move towards lower frequencies. Moreover the additional white noise current allows control the thermal effects on the system varying the effective temperature.

1.5.2 Thermal noise in long JJs

The noisy dynamics of a LJJ was explored by Fedorov *et al* [60, 61] and Augello *et al* [6]. The electrodynamics of a LJJ, in the Stewart-McCumber framework [62], is ruled by a differential equation called the sine-Gordon (SG) equation

$$\beta \frac{\partial^2 \varphi}{\partial t^2} + \frac{\partial \varphi}{\partial t} - \frac{\partial^2 \varphi}{\partial x^2} = i_b(x) - \sin(\varphi(x,t)) + i_f(x,t) \tag{1.12}$$

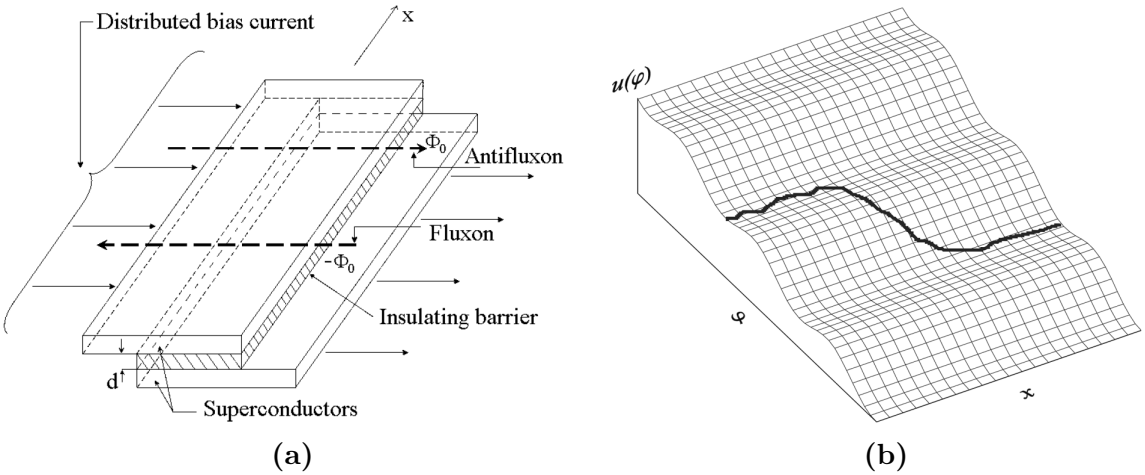

Figure 1.10: a) Schematic representation of a LJJ. b) Washboard potential $u(\varphi)$ and a phase string.

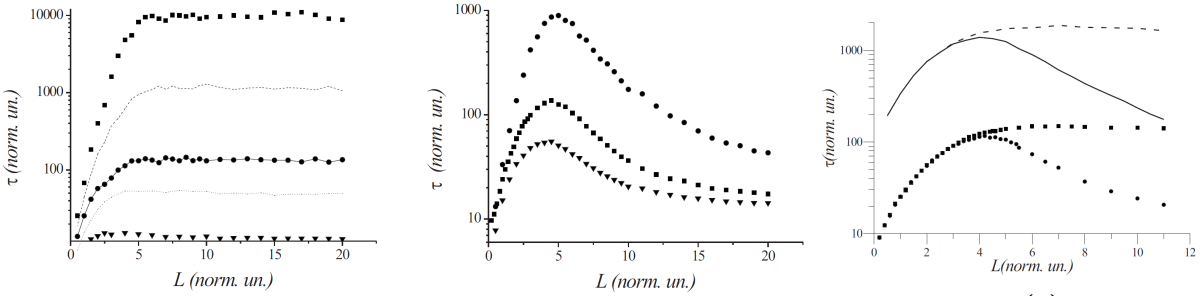

Figure 1.11: MST of LJJ for: (a) homogeneous bias current distribution with β=0.01: squares, i_0=0.5, γ=0.3; circles, i_0=0.7, γ =0.3; triangles, i_0=0.9, γ =0.3; solid line, γ =0.2, i_0=0.7; dashed line γ =0.4, i_0=0.7; (b) inhomogeneous bias current density with β=0.01, γ=0.4 and (circles) i0=0.5, (squares) i0=0.6, (triangles) i0=0.7; (c) γ=0.3, i0=0.7: circles for β=0.01 and solid line for β=100, inhomogeneous distribution, squares for β=0.01, and dashed line for β=100, homogeneous distribution.

where $\beta = \omega_c RC$ is the McCumber parameter, with R and C respectively the equivalent resistance and capacitance of the LJJ, ω_c the characteristic frequency. The bias $i(x)$ and the fluctuating $i_f(x,t)$ current densities are both normalized to the critical value I_c. The term $i_f(x,t)$ takes into account the thermal fluctuations. The absence of an external magnetic field Γ is included in the boundary conditions

$$\varphi_x(0,t) = \varphi_x(L,t) = \Gamma = 0, \tag{1.13}$$

where L is the LJJ length normalized to the Josephson penetration depth λ_J. The fluctuating term $i_f(x,t)$ used by Fedorov *et al* [60, 61] represents a Gaussian white noise signal with zero mean value and

$$\langle i_f(x,t) i_f(x',t') \rangle = 2\gamma\delta(x-x')\delta(t-t'), \tag{1.14}$$

where $\gamma = I_T/(J_c\lambda_J)$ is the dimensionless noise intensity, $I_T = 2ek_BT/\hbar$ the thermal current, T is the temperature and J_c is the critical current density of the JJ. The structure of a LJJ is shown in Fig. 1.10a. A LJJ can also be depicted as a *phase string* located beetwen the valleys of a bidimensional washboard potential (see Fig. 1.10b, the solid line represents the *phase string*). The mean life time is calculated as the time of permanence of the string elements inside the interval $[-\pi, \pi]$. Two different bias current distributions are used

$$i_b(x) = \begin{cases} i_0 & homogeneous \\ \frac{i_0\, L}{\pi\sqrt{x\,(L-x)}} & inhomogeneous. \end{cases} \tag{1.15}$$

Fig. 1.11a shows the MST τ data as a function of the junction length L. Two different regime are evident for the τ values: a raising up trend for small length ($L \lesssim 1$) and a saturation regime for $L \gtrsim 5$ with a costant value reached. For $L \lesssim 1$ the interaction beetwen each elementary part of the string and its neighbors is so strong that the string, also after stochastic fluctuations, can overcome the potential barrier only as a whole. Therefore, in these conditions, the escape time linearly grows by lengthening the junction. When $L \gtrsim 5$ the formation of kinks, i.e. a 2π step in the φ values located beetwen two neighboring washboard valleys (see solid line in Fig. 1.10b), and antikinks is allowed. The results obtained changing the bias current distribution are shown in the Fig. 1.11b. A non-monotonic effect is clearly evident. The small length regime is equivalent to the case

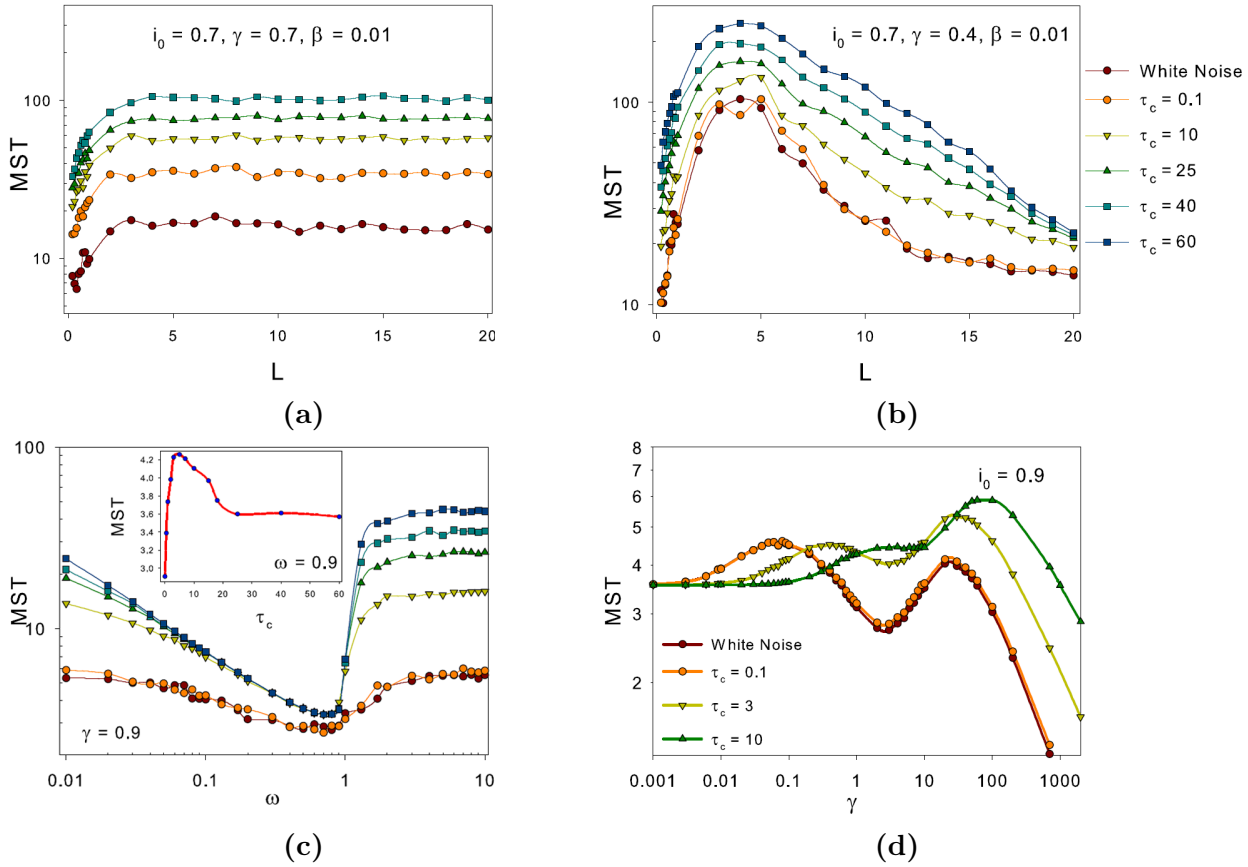

Figure 1.12: a) b) MST vs L for $i_0 = 0.7$, for white noise and colored noise with different correlation times τ_c, and $\beta = 0.01$: a) homogenous $i(x)$ and $\gamma_{cn} = 0.7$, b) inhomogenous $i(x)$ and $\gamma_{cn} = 0.4$. [6, 7]

of the homogeneous bias current distribution (see Fig. 1.11c). When the kink formation is permitted, the role of the edges of the junction, acting in this case as a generators of kinks, is crucial. The inhomogeneous bias current distribution includes large values in correspondence of the edges of the junction. The parts of the string subjected to these intense currents, slip freely on the washboard potential, supporting the generations of kinks and antikinks. This effect enhances if L increases, and this explains the observed non-monotonic behaviors.

The transient dynamics of an overdamped LJJ in presence of fluctuating bias current and oscillating potential was studied by Augello *et al* [6]. The investigation was developed in the framework of the SG model Eq. 1.12 with the boundary conditions Eq. 1.13. Both homogenous and inhomogenous bias current density Eq. 4.10 have been used. Firstly, the effect of only a correlated noise source with correlation function

$$\langle i_{cn}(x,t) i_{cn}(x',t') \rangle = \frac{2\gamma_{cn}}{2\tau_c} \delta(x-x') e^{-\frac{|t-t'|}{\tau_c}}, \tag{1.16}$$

was considered ($2\gamma_{cn}$ is the intensity of the source). The MST as a function of the JJ length L is reported in Fig. 1.12a and 1.12b, for different values of τ_c and for homogeneous and inhomogenous bias current distributions, respectively. The MST behavior are equal to those obtained by Fedorov *et al* [60, 61]. A MST decrease, as the intensity of the colored noise γ increases, was found. The results highlight the presence of different regimes: for small lengths the kinks formation is forbidden, exceeding a threshold value kinks are formed. Using an inhomogenous bias current density, the junction edges act as kinks generators, producing the MST decrease by increasing the junction length. The study was integrated including in the bias current an oscillating driving current signal:

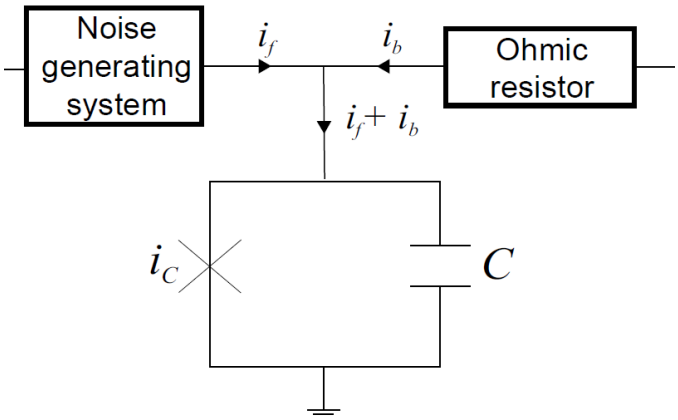

Figure 1.13: Circuit diagram of a JJ noise detector: a JJ with critical current i_c is biased in a twofold way. [10]

$$i(t) = i_b(x) + A\sin(\omega t) \tag{1.17}$$

where A and ω are its amplitude and angular frequency, respectively. The results are presented in Fig. 1.12c. All the MST as a function of ω curves show a minimum, signature of RA effects. Moreover, for $0.3 < \omega < 0.1$ the curves with different τ_c overlap. In order to investigate in detail the behavior in this frequency range, the MST as a function of τ_c, setting $\omega = 0.9$, is reported in the inset of Fig. 1.12c, finding a nonmonotonic behavior. The MST as a function of the noise intensity γ presents NES effects, which manifests itself as a double peack structure (see Fig. 1.12d).

1.5.3 Non-Gaussian noise in JJs

The JJs behavior is strongly influenced by environmental perturbations, and specifically by the presence of noise source responsible for decoherence phenomena [22, 33]. The role played by random fluctuations in the dynamics of these devices has recently solicited a large amount of work and investigations on the effects both of thermal and non-thermal noise sources on the transient dynamics of Josephson junctions [34–39]. The noise current signal is caused by the stochastic motion of the charge carriers, namely the Cooper pairs in a superconductor. While thermal noise is originated by the thermal motion of the charge carriers, non-thermal noise signals are related to their scattering and transmission. Non-Gaussian noise appears when the conductor, or the superconductor, is in a non-equilibrium state because of the presence of a bias voltage or current. In the last decade, theoretical progress allowed one to calculate the entire probability distribution of the noise signal and its cumulants, performing a *full counting statistics* of the current fluctuations [35]. Moreover, the presence of non-Gaussian noise signals has been found experimentally in many systems [34, 38, 63–66]. As an example in a wireless ad hoc network with a Poisson field of co-channel users, the noise has been well modeled by an α-stable distribution [66]. Non-equilibrated heat reservoir can be considered as a source of non-Gaussian noise sources [63–65]. Specifically, the effect of non-Gaussian noise on the average escape time from the superconducting metastable state of a current biased JJ, coupled with non equilibrium current fluctuations, has been experimentally investigated [34, 38].

Recently, the characterization of JJs as detectors, based on the statistics of the escape times, has been proposed [27–30, 67–69]. In particular, the statical analysis of the switching from the metastable superconducting state to the resistive running state of the JJ has been proposed to detect weak periodic signals embedded in a noise

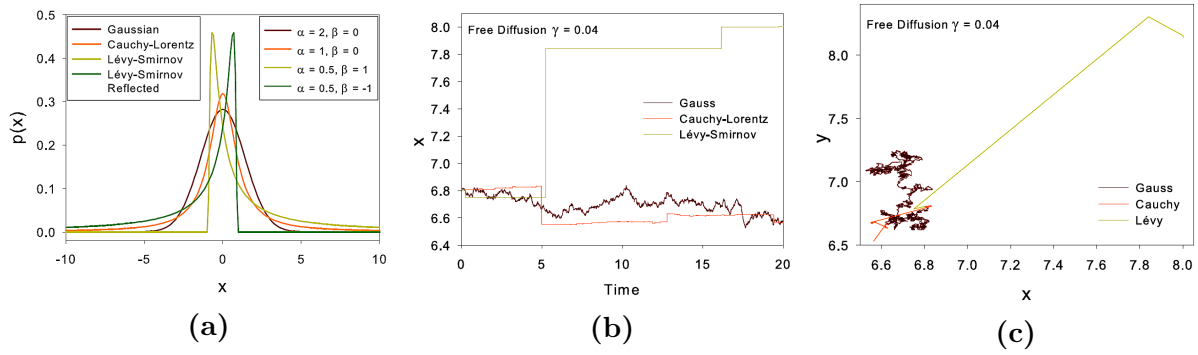

Figure 1.14: a) Probability density function for the four stable distribution: Gaussian (dark red), Cauchy-Lorentz (orange), Lévy-Smirnov (light green) and Lévy-Smirnov Reflected (dark green). b) c) One dimensional and two dimensional, respectively, trajectory of the free diffusion of a particle subjected to noise signals with Gaussian, Cauchy-Lorentz and Lévy-Smirnov distribution. [7, 11]

environment [29, 30]. Moreover, the rate of escape from one of the metastable wells of the tilted washboard potential of a JJ encodes information about the non-Gaussian noise present in the input signal [27, 28, 67–69].

After the seminal paper of Tobiska and Nazarov [39], Josephson junctions used as threshold detectors allow to study non-Gaussian features of current noise [67, 68]. Specifically, when a JJ leaves the metastable zero voltage state it switches to a running resistive state and a voltage appears across the junction. Therefore, it is possible to measure directly in experiments the escape times or switching times and to determine its probability distribution [8, 9, 70–73]. A typical simplified realization of a JJ noise detector is shown in Fig. 1.13. The fluctuating current i_f, produced by the noise generating system, is added to the bias current i_b and drives the JJ, characterized by a critical current i_c and a capacitance C. The switching times of the junction can be directly measured using the time-domain technique [8, 9, 70, 74, 75]. For each switching event the bias current is ramped up to a value i_b, which is very close to the critical current i_c and it is maintained constant for a period of waiting time. To record the switching time, the voltage across the junction is sent to a timer-counter, which is triggered by the sudden jump from zero voltage state to finite voltage state. The bias current is then decreased to zero, the junction returns to the zero voltage state, and a new cycle starts again. For JJs working in overdamped regime, the superconducting state is restored automatically, without necessity to decrease the bias current to zero. The process is repeated enough times to obtain a statistically significant ensemble of switching times (ST).

1.5.4 Non-Gaussian noise in short JJs

Recently, Augello *et al* [11] explored the role of thermal and non-Gaussian noise sources on the transient dynamics of short overdamped JJs. They addressed the problem in the resistively shunted junction (RSJ) framework [62], considering the following Langevin equation for the phase dynamics

$$\frac{d\varphi(t)}{dt} = -\omega_c \frac{dU(\varphi)}{d\varphi} - \omega_c(i_{TN}(t) + i_{nG}(t)), \tag{1.18}$$

where $i_{TN}(t)$ and $i_{nG}(t)$ are a Gaussian thermal noise and a non-Gaussian noise source, respectively. The expression of the potential is

$$U(\varphi, t) = 1 - \cos(\varphi) - i(t)\varphi, \tag{1.19}$$

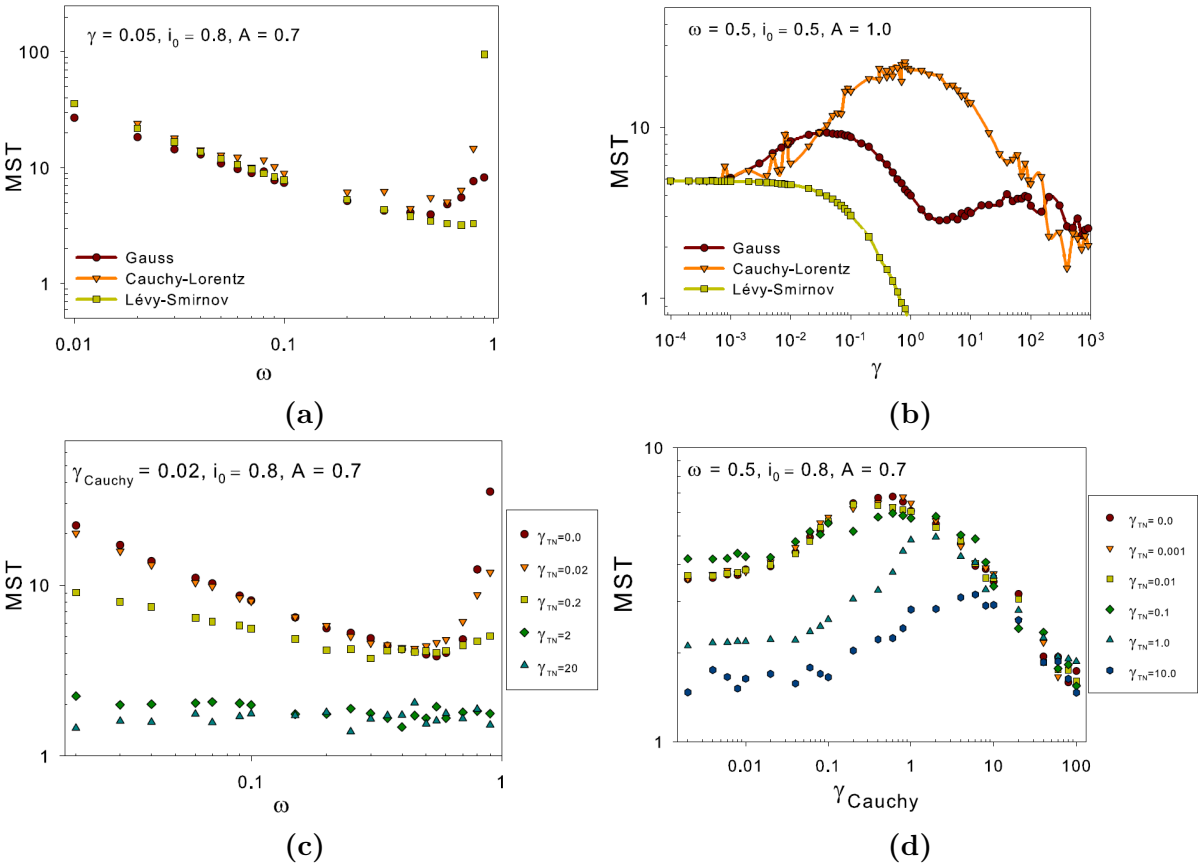

Figure 1.15: Log-Log plot of MST as a function of ω (panel a) and γ (panel b) for Gaussian, Cauchy-Lorentz and Lévy-Smirnov distributions of the noise signals. Log-Log plot of MST as a function of ω (panel c) and γ_{Cauchy} (panel d) for different thermal noise intensities γ_{TN}. [7, 11]

where

$$i(t) = i_0 + A\sin(\omega t) \tag{1.20}$$

as in the work of Gordeeva *et al* [5]. The results with $i_{TN}(t) = 0.0$ and $i_{nG}(t)$ given by Cauchy-Lorentz, reflected Lévy-Smirnov and Gaussian distributions are presented in Fig. 1.15a and 1.15b. The values of characteristic parameters and the probability density functions of these stable distributions are show in Fig 1.14a. The minus sign of $i_{nG}(t)$ in Eq. 1.18 indicates that the reflected Lévy-Smirnov distribution was considered. By this way the Lévy jumps push the particle in the positive φ direction. In Fig. 1.15a, the RA phenomenon is observed, but the Lévy Smirnov MST values are smaller then the Gaussian and Cauchy-Lorentz ones. In Fig. 1.15b, the curves corresponding to Gaussian and Cauchy-Lorentz show NES effect. For very low noise intensities, that is in the deterministic regime, all three curves tend to the same MST value. Increasing the noise intensity the Lévy-Smirnov curve decrease monotonically, because greater jumps, the so-called Lévy flights [76], push the particle very fast from the superconducting state. For higher γ values, the Gaussian curve is characterized by a double-maximum NES effect, sign of two different mechanism giving temporary trapping phenomenon. The Cauchy-Lorentz results show a single NES maximum, shifted towards higher intesity values respect to the Gaussian first peak. This is due to the typical displacement respect the mean value of the Cauchy-Lorentz distribution, that is shorter compared with the Gaussian case. This is well shown in the free-diffusion trajectories of a particle under the influence of Gaussian and Cauchy-Lorentz noises, displayed in the Fig 1.14b and Fig 1.14c. Results presented in Fig. 1.15c and 1.15d are obtained using a thermal and a Cauchy-Lorentz noise sources with intensities γ_{TN} and γ_{Cauchy}, respectively. The curves

shown in Fig. 1.15c represent MST as a function of ω changing the γ_{TN} value. The curve with $\gamma_{TN} = 0.0$ shows RA phenomenon. This effect is robust enough to be clearly detected until $\gamma_{TN} \leq 0.2$. While the position of the minimum is slightly affected by the presence of the thermal noise source, the MSTs for low and high frequencies decrease. The results in Fig. 1.15d represent MST as a function of γ_{Cauchy}, by changing the γ_{TN} value, and reveal the presence of NES effects. The simultaneous action of two noise sources produces an increase in the overall noise intensity "felt" by the system. Increasing the thermal noise intensity the maximum is lower and shifted towards higher γ_{Cauchy} values.

1.6 Noisy dynamics in long and short JJs: overview of the project

In the framework sketched out by experimental and computational works presented in this introduction, this work explores the transient dynamics of various JJ in the presence of noise sources. The focus is placed on the evolution of nonlinear solutions, i.e. soliton, antisoliton and breathers, of the SG model, their modifications due to noise influence and the connections with the transient dynamics of these devices. The investigation is computationally performed through numerical algorithms mainly implemented using fortran language based codes. The study of the lifetime in the metastable state gives informations about the switching from the superconducting regime and about all the macroscopic quantities, that is current, voltage and magnetic field, characteristic of the system. Noise represent a suitable way to model the influence of the environment on the system, and to control the dynamics of a JJ device by using it.

Taking a cue directly from the papers by Augello *et al* [6, 11], in chapter 2 the transient dinamycs of a LJJ under the simultaneous action of thermal and non-Gaussian noise sources is investigated. Soliton dynamics is deeply explored.

In chapter 3 the creation and propagation of breathers, in LJJ excited by a suitable external pulse, is analyzed. The breathers are peculiar unstable solutions of SG equation decaying in time. The effect of environmental fluctuation on the breathers stability is takes into account.

Chapter 4 contains a deep investigation of a different short junction that includes a graphene layer beetwen the superconducting elecrodes. The Josephson current for this system is quite different, departing from the conventional sinusoidal behavior. The MFPT is studied as a function of the frequency and the initial value of the applied bias current and of the parameters of the Gaussian colored noise source .

In chapter 5 the conclusions are drawn, including an outline of the main results and the future developments of these research lines.

Finally, various appendixes are included. In appendix A the algorithm used to model the α-stable distributions is described. In appendix B the numerical implementation of implicit finite-difference method used to numerically integrate the sine-Gordon equation is shown. Appendix C contains informations about the current-phase relation for a graphene based Josephson junction.

Chapter 2

Long JJ: the effects of the non-Gaussian noise

In this chapter the superconducting lifetime of long current-biased Josephson junctions, in the presence of Gaussian and non-Gaussian noise sources, is investigated. In particular, the dynamics of a Josephson junction as a function of the noise signal intensity, for different values of the parameters of the system and external driving currents, is analyzed. The chapter is organized as follows. In section 2.1 the equivalent circuit and mechanical model associated with a LJJ are described. In section 2.2 the sine-Gordon model is presented. In section 2.3 the statistical properties of the Lévy noise are briefly reviewed, showing some peculiarities of different α-stable distributions. Section 2.4 gives computational details. In section 2.5 the theoretical results for the behaviors of the MST as a function of the junction length, frequency of the external driving current and noise intensity with homogeneous and inhomogeneous bias current, are shown and analyzed. This analysis has been carried out at very low temperatures of the system, around the *crossover* temperature.

Below this temperature, the phase difference over the junction behaves quantum mechanically, the escape events occur primarily by quantum tunneling through the barrier, and the thermal fluctuations can be neglected. Therefore, only the effects of non-Gaussian noise have been analyzed. The transient dynamics of a long JJ subject to thermal fluctuations and non-Gaussian, Lévy type, noise sources is investigated in section 2.6. Finally, in section 2.7 the conclusions are drawn.

2.1 Equivalent circuit and mechanical model

The dynamics of long Josephson junctions can be described by an equivalent circuit and a mechanical model. The effects of spatially extension has to be taken into account when one or more dimension of the junction exceeds the Josephson penetration depth λ_J (see Eq. 1.6). In what follow, the effects due to the extension of only one dimension of the junction will be taken into account to investigate the dynamics of narrow LJJ. Josephson supercurrent and bias current, flowing in the junction, generate magnetic fields that influence the current distribution in the direction along which the junction extends. The geometry of a LJJ is shown in figure 2.1a. The two superconducting layers are separated by a non-superconducting layer, playing the role of an insulator. The insulator, usually a thin oxide layer, has uniform thickness t_{ox} along the Z-axis representing the Cooper pairs tunneling direction. The width W is very shorter than the Josephson penetration depth, $W << \lambda_J$, so that the electromagnetic field in the insulating barrier could be considered uniformly distributed in the Y-direction. The tunneling supercurrent is described by the

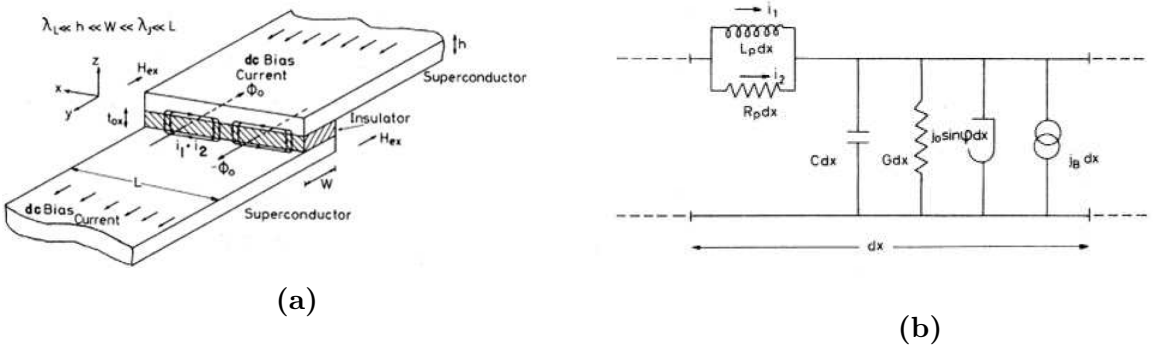

(a) (b)

Figure 2.1: a) Schematic representation of the geometry of a LJJ. b) Circuit scheme representing the dynamics of a LJJ.

Josephson equations 1.3 and 1.5. Considering a combination of these equations and the Maxwell equations, a set of partial-differential equations representing the dynamics of the junction is obtained

$$\frac{\partial V}{\partial X} = -i_2 R_P = -L_P \frac{\partial i_1}{\partial T} \tag{2.1}$$

$$\frac{\partial i_1}{\partial X} + \frac{\partial i_2}{\partial X} = -C\frac{\partial V}{\partial T} - GV - J_0 \sin\varphi + J_B \tag{2.2}$$

where i_1 and i_2 are the superconducting and the normal components of the current flowing parallel to the barrier in the X direction. Considering the Eqs.(2.1) and (2.2), the dynamics of a LJJ can be described, in terms of the circuit scheme shown in Fig. 2.1b. The resistance R_P, is related to the dissipative effects due to the motion of quasi-particles, and represents, in this case, the scattering of quasi-particle in the superconductor's surfaces. L_P is the the inductance per unit length, and represents the magnetic energy stored within one London penetration depth of the superconductor. It is equal to $L_P = \mu_0(\lambda_{L_1} + \lambda_{L_2} + t_{ox})/W$, where $\lambda_{L_{1,2}}$ are the London penetration depths for the two superconductors and μ_0 is the vacuum magnetic permeability. The capacitance per unit length C represents the electric energy stored in the barrier. It is given by $C = \epsilon_r \epsilon_0 W = t_{ox}$, where ϵ_r is the relative dielectric constant of the barrier oxide layer and ϵ_0 is the vacuum dielectric constant. The term GV takes into account the dissipative effects of quasi-particle motion through the effective normal resistance per unit length $R = 1/G$. The supercurrent per unit length is given by $J_0 \sin\varphi$, J_B represents the externally applied bias current per unit length [77]. The equivalent circuit of a LJJ can be represented by a connection of a set of SJJs. In Fig. 2.1b the parallel connection of L_P and R_P can be distinguished by the equivalent circuit representing a SJJ. The long junction equivalent circuit corresponds to a set of the circuits of Fig. 2.1b connected in parallel. The Eqs. 1.5, 2.1 and 2.2, can be combined in the third-order partial-differential equation

$$\frac{L_P}{R_P}\frac{\partial^3\varphi}{\partial^2 X \partial T} + \frac{\partial^2\varphi}{\partial^2 X} - L_P\frac{\partial^2\varphi}{\partial^2 T} - GL_P\frac{\partial\varphi}{\partial T} = \frac{2\pi L_P J_0}{\Phi_0}\left(\sin\varphi - \frac{J_B}{J_0}\right). \tag{2.3}$$

The third-order effects will be not considered, that is the term $\partial^3\varphi/\partial^2 X\partial T$ in Eq.(2.3) will be neglected. This corresponds to neglect the presence of surface loss in the electrodes due to the scattering of quasi-particle in proximity to the surfaces [78]. Considering the expressions of the Josephson penetration depth Eq. 1.6, the characteristic and plasma frequencies, with the proper normalizations for space and time, the sine-Gordon (SG) equation results from the Eq.(2.3).

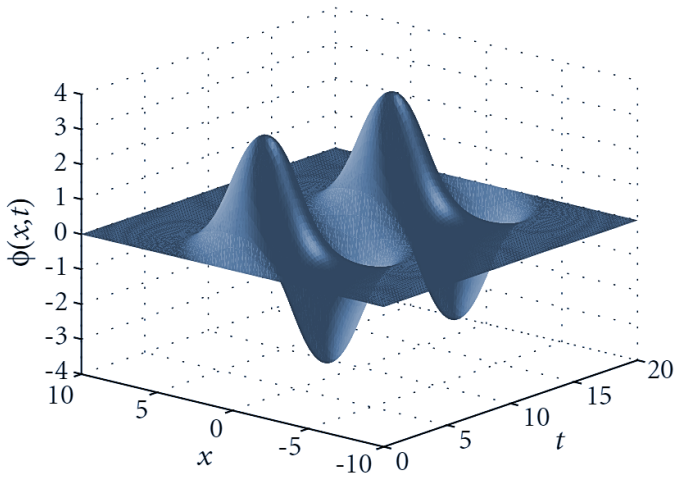

Figure 2.2: Stationary breather, with $\omega_b = \pi/5$. Picture adapted from [1].

2.2 The SG Model

The dynamics of the phase difference of the LJJ, analyzed within the SG formalism [60–62, 79], is characterized by the formation and propagation of particular wave packets, called *solitons* [80, 81]. Their presence is strongly connected with the penetration of the magnetic flux quanta, i.e. *fluxons* [82, 83] (the magnetic soliton), travelling through the junction during the switching towards the resistive state (see Fig. 2.3b). Several systems governed by SG equation show evidence of soliton motion, including not only JJs [84–90] but also the relativistic field theory, mechanical transmission lines, and atomic, particle and condensed matter physics.

The electrodynamics of a normal JJ is described by a nonlinear partial differential equation for the order parameter φ, that is the SG equation [62, 79]. Here φ is the phase difference between the wave functions describing the superconducting condensate in the two electrodes. The unperturbed SG equation, in the absence of damping, bias and noise, in normalized units is given by [1, 82]

$$\varphi_{xx}(x,t) - \varphi_{tt}(x,t) = \sin(\varphi(x,t)). \tag{2.4}$$

First introduced in 1939 by Frenkel and Kontorova [91] to study the dynamics in crystal dislocations, the SG equation found application in a huge number of fields, among others simple one-dimensional model for elementary particle, Bloch walls dynamics, self-induced trasparency in nonlinear optics and spin waves in the liquid in ^{3}He. The SG model can be depict as a linear array of coupled pendula [62]. This suggests solutions in the traveling wave form $f = \varphi(x - vt)$:

$$\varphi(x,t) = 4\arctan\left[\pm\gamma\left(x - vt\right)\right], \tag{2.5}$$

where $v < 1$ is the wave propagation velocity normalized to the speed of light in the medium, also called *Swihart velocity* and $\gamma_\ell = (1 - v^2)^{-1/2}$ is the Lorentz factor. Eq. (2.5) represents a single *kink*, or *soliton*, that is a 2π variation in the phase values. The signs $+$ and $-$ indicate a 2π-kink (soliton) and a 2π-antikink (antisoliton), respectively. Furthermore $\varphi/2\pi$ has "topological charge" $+1$ for a kink and -1 for an antikink. Imposing the boundary conditions $\varphi(x \to \pm\infty) = 0$ the generic N-solitons solution can be given [92, 93]. The kink-kink collision formula, i.e. the simplest 2-soliton solution of the SG equation, is:

$$\varphi(x,t) = 4\arctan\left[\frac{v\sinh\left(\gamma_\ell x\right)}{\cosh\left(\gamma_\ell vt\right)}\right], \tag{2.6}$$

and a kink-antikink collision is

$$\varphi(x,t) = 4\arctan\left[\frac{\sinh(\gamma_\ell v t)}{v\cosh(\gamma_\ell x)}\right]. \tag{2.7}$$

The Eq.(2.7) take an interesting expression if the velocity is allowed to be imaginary. Setting

$$v = \mathrm{i}\omega_b/\sqrt{1-\omega_b^2} \qquad\qquad \omega_b < 1 \tag{2.8}$$

the Eq.(2.7) becomes the equation of a *stationary breather*, oscillating with frequency ω_b,

$$\varphi(x,t) = 4\arctan\left\{\frac{\sqrt{1-\omega_b^2}}{\omega_b}\frac{\sin(\omega_b t)}{\cosh\left(x\sqrt{1-\omega_b^2}\right)}\right\}, \tag{2.9}$$

shown in Fig. 2.2 for $\omega_b = \pi/5$. Eq.(2.4) is invariant under Lorentz trasformation, so this stationary breather can be boosted into a moving frame, resulting in the following *moving breather*, travelling with an envelope velocity $v < 1$,

$$\varphi(x,t) = 4\arctan\left\{\frac{\sqrt{1-\omega_b^2}}{\omega_b}\frac{\sin\left[\gamma_\ell\omega_b\left(t-vx\right)\right]}{\cosh\left[\gamma_\ell\sqrt{1-\omega_b^2}\,(t)\,(x-vt)\right]}\right\}. \tag{2.10}$$

Physical models often suggest other nonlinear terms instead of "$\sin\varphi$" in Eq.(2.4), such $\varphi^3-\varphi$ (from the φ^4 equations of particle physics) or $\sin\varphi+\sin\varphi/2$ (the so called *double SG equation*). Though these models admit non-dissipative kink solutions, these kinks don't maintain their shape after collisions and thus are not considered solitons. The unperturbed SG equation che be exactly solved by analytical techniques. First solution by direct method was produced by Hirota [94], and an year later Ablamowitz *et al* [95] and Lamb [96] produced the *inverse scattering method* to solve this equation. Also Bäcklund transformations can be used to solve the SG equation. The sine-forcing term in the SG equation can be view as a nonlinear deformation $\varphi\to\sin\varphi$ of the linear forcing term of the Klein-Gordon (KG) equation [97]. This implies that SG equation can be derived as an Euler-Lagrangian equation from the Lagrangian density

$$\mathcal{L}_{\mathrm{SG}}(\varphi) = \left(\varphi_t^2-\varphi_x^2\right)/2 - 1 + \cos\varphi, \tag{2.11}$$

expected as a "deformation" of the KG Lagrangian

$$\mathcal{L}_{\mathrm{KG}}(\varphi) = \left(\varphi_t^2-\varphi_x^2\right)/2 - \varphi^2/2. \tag{2.12}$$

Therefore, beetwen the two Lagrangians exist the relations

$$\mathcal{L}_{\mathrm{SG}}(\varphi) = \mathcal{L}_{\mathrm{KG}}(\varphi) + \sum_{n=2}^{\infty}\frac{(-\varphi^2)^n}{(2n)!}. \tag{2.13}$$

The Hamiltonian density (kinetic plus potential energy), can be give in terms of canonically-conjugate coordinate and momentum fileds by

$$\mathcal{H}_{\mathrm{SG}}(\varphi,\Pi) = \Pi\varphi_t - \mathcal{L}_{\mathrm{SG}}(\varphi) = \left(\Pi^2+\varphi_x^2\right)/2 + 1 - \cos\varphi \tag{2.14}$$

so the Hamiltonian is

$$H = \int_{-\infty}^{\infty}\mathcal{H}_{\mathrm{SG}}(\varphi,\Pi)dx = \int_{-\infty}^{\infty}\left[\left(\Pi^2+\varphi_x^2\right)/2 + 1 - \cos\varphi\right]dx. \tag{2.15}$$

The SG equation is an infinite-dimensional Hamiltonian system with Poisson brachets given by

$$\{F, G\} = \int_{-\infty}^{\infty} \left[\frac{\delta F}{\delta \varphi(x)} \frac{\delta G}{\delta \Pi(x)} - \frac{\delta F}{\delta \Pi(x)} \frac{\delta G}{\delta \varphi(x)} \right] dx. \tag{2.16}$$

The Hamilton's equations yield the SG equation

$$\frac{\delta H}{\delta \varphi} = -\dot{H} \qquad \text{and} \qquad \frac{\delta H}{\delta \Pi} = \dot{\varphi} \tag{2.17}$$

$$-\ddot{\varphi} = -\dot{H} = -\varphi_{xx} + \sin\varphi \qquad \text{and} \qquad \Pi = \dot{\varphi}. \tag{2.18}$$

Computing H

$$H = \int_{-\infty}^{\infty} \left[\left(\varphi_t^2 + \varphi_x^2\right)/2 + 1 - \cos\varphi \right] dx \tag{2.19}$$

for a soliton and for a breather the resulting energies are

$$E_s = 8\gamma_\ell \tag{2.20}$$

$$E_b = 16\gamma_\ell \sqrt{1-\omega_b^2}. \tag{2.21}$$

In this framework, φ gives a normalized measure of the magnetic flux through the junction, so that Eq. (2.4) can also represent the motion of a single fluxon (or antifluxon). In fact, starting from simple electrodynamic considerations [62], it is possible to obtain a simple relation between the magnetic field $H(y)$ and the spatial derivative of the phase difference

$$\varphi_x = 2\pi \frac{dH(y)}{\Phi_0}, \tag{2.22}$$

where $d = \lambda_{L_1} + \lambda_{L_2} + t_{ox}$ is the magnetic penetration, λ_{L_1} and λ_{L_2} are the London depths in the left and right superconductors and t_{ox} is the interlayer thickness. In our LJJ model, if the junction is extended along x and short along z, the magnetic field points along y. Integrating Eq. (2.22) over the entire JJ length the following relation is obtained

$$\varphi(L) - \varphi(0) = 2\pi \frac{\Phi_H}{\Phi_0}, \tag{2.23}$$

where Φ_H is the magnetic flux through the junction and $\Phi_0 = hc/2e$ is the fluxon. If the phase string has a portion lying in the first valley and a portion inside the $n-$valley, from Eq. (2.29), the phase difference is equal to $2\pi n$. Therefore the magnetic flux will be equal to

$$2\pi n = 2\pi \frac{\Phi_H}{\Phi_0} \qquad \Phi_H = n\Phi_0. \tag{2.24}$$

If the phase evolution shows a single 2π-kink, a single fluxon will propagate along the junction, as shown in Fig. 2.3b. Here the washboard potential is represented at three different times $t = 0, \frac{\pi}{2\omega}, \frac{3\pi}{2\omega}$, corresponding to zero initial slope, maximum and minimum slope, respectively. The line on the highest potential profile represents a soliton between two adjacent valleys. The panel (b) of the same figure shows a soliton and the shape of the correspondent fluxon, that is the values of the x-derivative of φ, along the junction length in a generic time t'.

Our analysis includes a quasiparticle tunneling term and an additional stochastic contribution, $i_f(x,t)$, representing the noise effects. However, the surface resistance of the superconductors is neglected. The resulting *perturbed* SG equation reads

$$\beta_{SG}\varphi_{tt}(x,t) + \varphi_t(x,t) - \varphi_{xx}(x,t) = i_b(x,t) - \sin(\varphi(x,t)) + i_f(x,t), \tag{2.25}$$

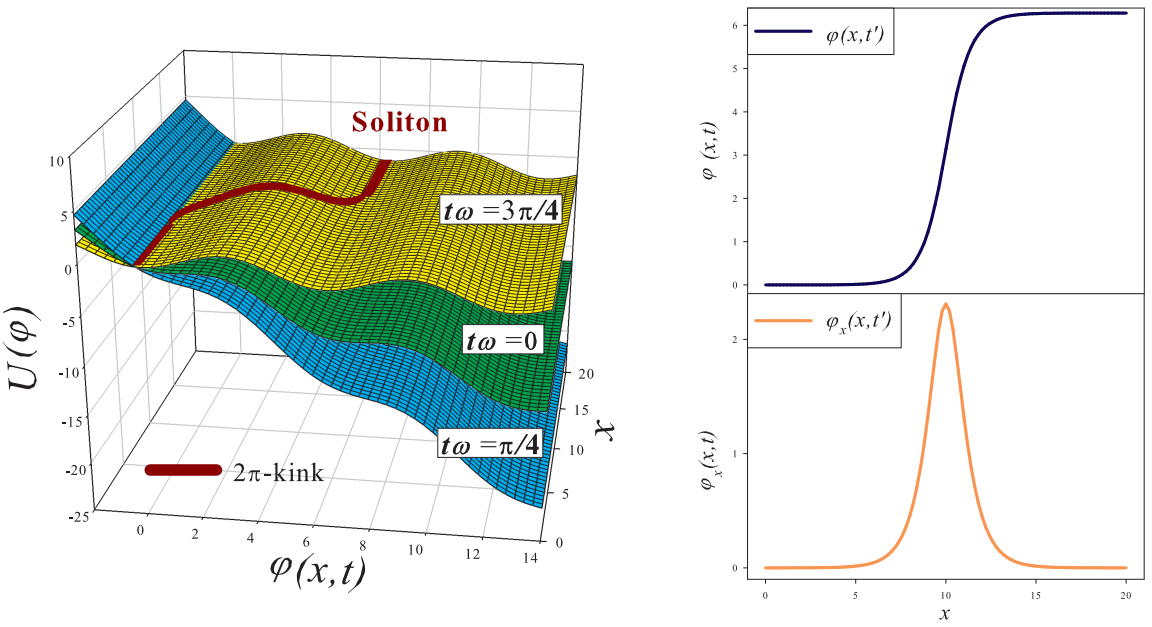

(a) **(b)**

Figure 2.3: (a) Washboard potential at 3 different times with a soliton wave (2π-kink) on the highest profile; (b) Soliton (Eq. (2.5)) and corresponding fluxon profile (Eq. (2.22)) [10].

where a simplified notation has been used, with the subscript indicating the partial derivative of φ in that variable. This notation will be used throughout all the work. In Eq. (2.25), the fluctuating current density $i_f(x,t)$ is the sum of two contributions, a Gaussian thermal noise $i_T(x,t)$ and an external non-Gaussian noise source $i_{nG}(x,t)$

$$i_f(x,t) = i_T(x,t) + i_{nG}(x,t). \tag{2.26}$$

The SG equation is written in terms of the dimensionless x and t variables, that are the space and time coordinates normalized respectively to the Josephson penetration depth λ_J and to the inverse of the characteristic frequency ω_c of the junction. Moreover, $\beta_{SG} = \omega_c RC$, where R and C are the effective normal resistance and capacitance of the junction. The terms $i_b(x,t)$ and $sin(\varphi)$ of Eq. (2.25) are respectively the bias current and supercurrent, both normalized to the JJ critical current i_C. Eq. (2.25) is solved imposing the following boundary conditions

$$\varphi_x(0,t) = \varphi_x(L,t) = \Gamma, \tag{2.27}$$

where Γ is the normalized external magnetic field. Hereinafter $\Gamma = 0$ is imposed.

The two-dimensional time-dependent tilted potential, named *washboard potential*, is given by

$$U(\varphi,x,t) = 1 - \cos(\varphi(x,t)) - i_b(x,t)\,\varphi(x,t), \tag{2.28}$$

and shown in Fig. 2.3a. In the same figure is shown a phase string in the potential profile (2.28), along which it moves during the switching dynamics. Specifically, the washboard potential is composed by a periodical sequence of peaks and valleys, with minima and maxima satisfying the following conditions

$$\begin{aligned} \varphi_{min} &= \arcsin(i(x,t)) + 2n\pi \\ \varphi_{max} &= (\pi - \arcsin(i(x,t))) + 2n\pi \end{aligned} \tag{2.29}$$

with $n = 0, \pm1, \pm2, \ldots$.

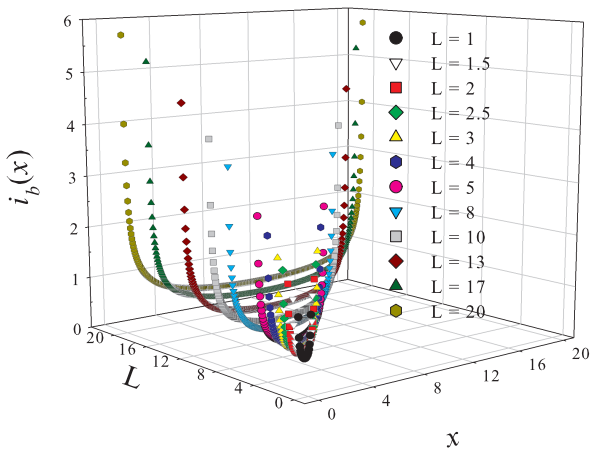

Figure 2.4: Inhomogeneous bias current density (see Eq. (4.10)) along JJs, for $i_0 = 0.9$ and different values of junction length [10].

The bias current is given by

$$i_b(x,t) = i_b(x) + A\,\sin(\omega t), \tag{2.30}$$

where A and ω are amplitude and frequency (normalized to ω_c) of the dimensionless driving current. This time dependence is normalized to the inverse of the JJ characteristic frequency ω_c.

The $i_b(x)$ term is a dimensionless current that, in the phase string picture, represents the initial slope of the potential profile. Different regimes of spatial dependence can be considered, obtaining in particular the two following current distributions [98]

$$i_b(x) = \begin{cases} i_0 & \textit{homogeneous} \\ \dfrac{i_0\,L}{\pi\sqrt{x\,(L-x)}} & \textit{inhomogeneous.} \end{cases} \tag{2.31}$$

The more realistic inhomogeneous condition provides strong current contributions at the edges of the junction. This is shown in Fig. 2.4, for $i_0 = 0.9$ and L ranging between 1 and 20. In these conditions, the phase of the cells in the edges of the junction can flow along the potential without resistance, so that the soliton formation occurs mostly in these parts of the junction.

2.3 The Lévy Statistics

The analysis is performed varying the statistic of the noise signal modeled by using different α-stable (or *Lévy*) distributions. These statistics allow to describe real situations [99] in which the evolution shows abrupt jumps and very rapid variations of parameters, called *Lévy flights*. Lévy-type statistics is observed in various scientific areas, where scale-invariance phenomena take place [100–103]. For a recent short review on Lévy flights see Dubkov *et al.* [76], and references there. Applications and other research fields in which observed evolutions are well reproduced using Lévy statistics are quite numerous, ranging from biology [104], zoology [105–107], social systems [108] and financial markets [109], to geological [110] and atmospheric data [111].

Distribution	Abbr.	P(x)	$S_\alpha(\sigma,\beta,\mu)$
Gaussian	(G)	$\frac{1}{\sqrt{2\pi}\sigma}e^{-\frac{(x-\mu)^2}{2\sigma^2}}$ $x\in\mathbb{R}$	$S_2(\sigma,0,\mu)$
Cauchy-Lorentz	(CL)	$\frac{\sigma/\pi}{\sigma^2+(x-\mu)^2}$ $x\in\mathbb{R}$	$S_1(\sigma,0,\mu)$
Lévy-Smirnov	(LS)	$\sqrt{\frac{\sigma}{2\pi}}\frac{e^{-\frac{\sigma}{2(x-\mu)}}}{(x-\mu)^{3/2}}$ $x\geq\mu$	$S_{\frac{1}{2}}(\sigma,1,\mu)$

Table 2.1: Closed form of the stable distributions and characteristic values of parameters.

In order to motivate the use of α-stable (or Lévy) distributions, some cases [112] in which non-Gaussian stable statistics is used to model experimental data with asymmetric and heavy tailed distributions, closely linked with the Generalized Central Limit Theorem [113–119], are recalled. The concept of stable distribution is briefly reviewed. A random non-degenerate variable is stable if

$$\begin{aligned}\forall n\in\mathbb{N},\exists(a_n,b_n)\in\mathbb{R}^+\times\mathbb{R}:\\ X+b_n=a_n\sum_{j=1}^{n}X_j,\end{aligned}\tag{2.32}$$

where the X_j terms are independent copies of X. Moreover X is strictly stable if and only if $b_n=0\ \forall n$. The well known Gaussian distribution stays in this class. This definition does not provide a parametric handling form of the stable distributions. The characteristic function, however, allows to deals with them. The general definition of characteristic function for a random variable X with an associated distribution function $F(x)$ is

$$\phi(u)=\left\langle e^{iuX}\right\rangle=\int_{-\infty}^{+\infty}e^{iuX}dF(x).\tag{2.33}$$

Following this statement, a random variable X is said stable if and only if

$$\begin{aligned}\exists(\alpha,\sigma,\beta,\mu)\ &\in\ ]0,2]\times\mathbb{R}^+\times[-1,1]\times\mathbb{R}:\\ X\ &\stackrel{d}{=}\ \sigma Z+\mu,\end{aligned}\tag{2.34}$$

where Z is a random number. Accordingly one obtains

$$\phi(u)=\begin{cases}\exp\left\{-|u|^\alpha\left[1-i\beta\tan\frac{\pi\alpha}{2}(\mathrm{sign}u)\right]\right\} & \alpha\neq1\\ \exp\left\{-|u|\left[1+i\beta\frac{2}{\pi}(\mathrm{sign}u)\log|u|\right]\right\} & \alpha=1\end{cases}\tag{2.35}$$

in which

$$\mathrm{sign}u=\begin{cases}\pm1 & u\ \gtrless\ 0\\ 0 & u\ =0\end{cases}\tag{2.36}$$

represents the sign function.

This definition of X requires four parameters: a *stability index* (or characteristic exponent) $\alpha\in]0,2]$, an *asymmetry parameter* β with $|\beta|\leq1$ and two real numbers $\sigma>0$ and μ that determine the outward of the distribution and are called, for this reason, *shape parameters*. The names of these two parameters indicate their physical meaning. Specifically $\beta=0$ ($\beta\neq0$) gives a symmetric (asymmetric) distribution, while

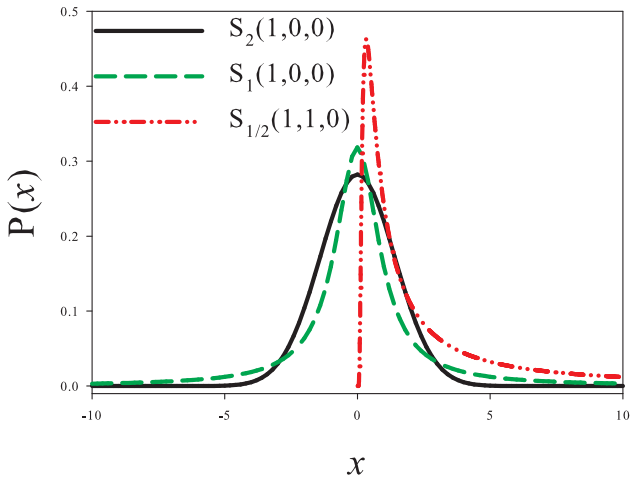

Figure 2.5: Probability density functions for Gaussian (G) (solid line), Cauchy-Lorentz (CL) (dashed line) and Lévy-Smirnov (LS) (dashed-dotted line) distributions [10].

α determines how the tails of distribution go to zero. For $\alpha < 2$ the asymptotic behaviour is characterized by a power law, while $\alpha = 2$ and $\beta = 0$ give a Gaussian distribution. The stable distribution, obtained setting $\sigma = 1$ and $\mu = 0$, is called *standard*. Every α-stable distribution are denoted with the symbol $S_\alpha(\sigma, \beta, \mu)$. Only a few number of Lévy distributions has a probability density function known in explicit form, as shown in Table (2.1). Here the abbreviations for some peculiar distributions, used in the rest of this work, are also listed.

The G (Gaussian) and CL (Cauchy-Lorentz) distributions (both with $\beta = 0$) are symmetrycal with respect to $x = 0$, while the LS (Lévy-Smirnov) distributions (normal and reflected) are skewed to the right ($\beta = +1$) or left ($\beta = -1$) side. The three distributions of Table (2.1) are plotted in Fig. 2.5. The reflected (with respect to the vertical axis) LS distribution, obtained setting $\beta = -1$, is not shown. The asymmetrical structure of the LS distribution is evident, with a heavy tail and a narrow peak located at a positive value of x. The CL distribution, in comparison with the Gaussian one, presents tails much higher and a central part of the distribution more concentrated around the mean value. For short times, the values extracted from a CL distribution determine trajectories characterized by *limited space displacement*: this can be explained noting that the CL statistics is characterized, around the mean, by a narrower form respect to the Gaussian one. For longer times, however, heavy tails cause the occurrence of events with large values of x, whose probability densities are non-neglectable. The use of CL and LS statistics allows to consider rare events, corresponding to large values of x, because of the fat tails of these distributions. These events correspond to the Lévy flights previously discussed. The algorithm used in this work to simulate Lévy noise sources is that proposed by Weron [120] for the implementation of the Chambers method [121].

2.4 Computational Details

The JJ dynamics in the SG overdamped regime, setting $\beta_{SG} = 0.01$, is studied. The time and spatial steps are fixed at $\Delta t = 0.05$ and $\Delta x = 0.05$. In order to obtain the mean values a suitable number ($N = 5000$) of numerical realizations are performed. Throughout the whole work, the words *string*, referring to the entire junction, and *cell* to indicate each of the elements with dimension Δx, which compose the junction, will be used. The washboard potential valley labeled with $n = 0$ (Eq. (2.29)) is chosen as initial

condition for solving Eq. (2.25), i.e. $\varphi_0 = \arcsin(i_b(x,0)) = \arcsin(i_b(x))$. In our model there are no barriers, neither absorbing nor reflecting, surrounding the initial metastable state, and the value of MST calculated is the nonlinear relaxation time (NLRT) [4]. After a first exit, other temporary trapping events are permitted: during the time evolution each cell can return into the initial potential well, contributing again to the final value of MST, indicate as τ. This agrees with the definition, proposed by Malakhov [122], for the mean permanence time of the phase φ inside the interval $[-\pi, \pi]$

$$\tau = \int_0^\infty tw(t)dt = \int_0^\infty P(t)dt, \tag{2.37}$$

where $P(t)$ is the probability that $\varphi \in [-\pi, \pi]$ and $w(t) = \partial P(t)/\partial t$. For each cell and for each realization the numerical calculation of $P(t)$ is performed by considering

$$P_{ij}(t) = \begin{cases} 1 \iff \varphi \in [-\pi, \pi] \\ \\ 0 \iff \varphi \notin [-\pi, \pi], \end{cases} \tag{2.38}$$

where P_{ij} is the probability that in the i-th realization for the j-th cell $\varphi \in [-\pi, \pi]$. Summing $P_{ij}(t)$ over the total number N_{cells} of string elements, and averaging first over the total number of cells, then over the total number N of realizations, the probability that the entire string is in the superconducting state at time t is

$$P(t) = \frac{1}{N\, N_{cells}} \sum_{i=1}^{N} \sum_{j=1}^{N_{cells}} P_{ij}(t) \tag{2.39}$$

The maximum time value used to perform the integral of Eq. (2.37) has to be set large enough so that temporary trapping events, in the metastable state, can occur. Therefore the upper limit of the integral, ∞, is replaced with a maximum time $t_{MAX} = 100$, obtaining the *mean switching time*

$$\tau = \int_0^{t_{MAX}} P(t)dt. \tag{2.40}$$

The whole procedure is repeated for the three noise statistics analyzed in the previous section, obtaining the behaviour of the MST τ in the presence of different sources of Lévy noise.

2.5 Effects of non-Gaussian noise

The analysis is carried out looking at the MST variations as a function of the junction length L, noise intensity γ and frequency ω of the driving signal. The i_0 values choosen are 0.5 and 0.9, to work with potentials less or more inclinated, and the $i_b(x)$ distributions used are homogeneous or inhomogeneous (Eq. (4.10)). The washboard slope is connected to the heights of the potential barriers seen by the phase elements. Reducing the i_0 value, the barriers intensity is enhanced and the MST values tend to increase. Evidences of nonmonotonic behaviour varying first the values of L, γ and ω, then the statistics of the noise sources are searched. Moreover, I try to find connections between the MST behaviors and JJ soliton dynamics. The amplitude of the oscillating driving signal is set to $A = 0.7$, to obtain at certain times (see Eq. (2.30)) $i_b(x,t) > 1$ (absence of metastable states) and, at least with one of the i_0 values used, $i_b(x,t) < 0$ (positive slope). In this section the thermal fluctuations of the current density $i_T(x,t)$ are neglected with respect to the non-Gaussian (Lévy) noise source $i_{nG}(x,t)$ in Eqs. (2.25), (2.26), because very low temperatures, around the *crossover* temperature, are considered.

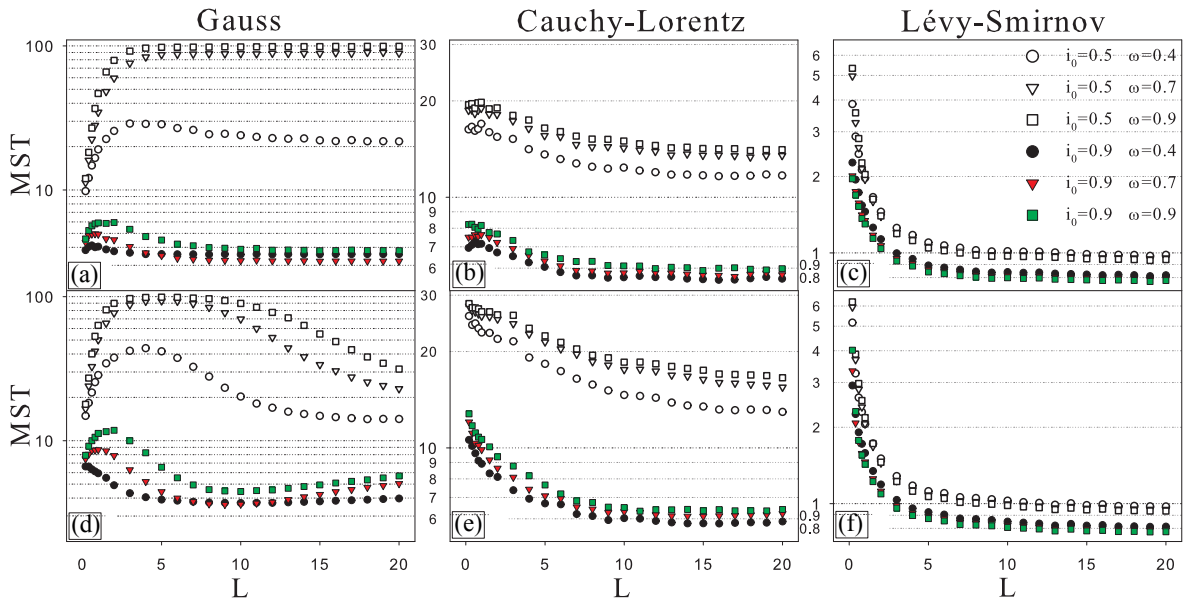

Figure 2.6: MST τ *versus* L for different current distributions along the junction: *homogeneous* $i_b(x)$ and noise sources with Gaussian (panel a), Cauchy-Lorentz (panel b) and Lévy-Smirnov (panel c) statistics; *inhomogeneous* $i_b(x)$ and noise sources with Gaussian (panel d), Cauchy-Lorentz (panel e) and Lévy-Smirnov (panel f) statistics. In all graphs the other parameters are: $i_0 = \{0.5(\text{empty symbols}), 0.9(\text{full symbols})\}$, $\omega = \{0.4$ (circles), 0.7 (triangles), 0.9 (squares)$\}$ and $\gamma = 0.2$. The legend in panel c refers to all pictures. [10]

.

2.5.1 MST vs JJ length L

I begin to study the MST values varying the JJ length L in the range $[0, 20]$. The results are shown in Fig. 2.6, emphasizing the three different noise sources used, G (panels ($h1$) and d), CL (panels b and e) and LS (panels c and f).

The panels ($h1$), b and c contain the results for homogeneous bias current density, while the panels d, e and f contain the results for inhomogeneous bias current density. In each panel, the MST values for $i_0 = 0.5$ are greater than those for $i_0 = 0.9$. This is due to the reduced height of the right potential barrier due to the increased slope, i.e. i_0 value, of the washboard. Specifically the expression for the left (or right) potential barrier height ΔU^+(or ΔU^-) is

$$\begin{aligned} \Delta U^{\pm}(x,t) = \quad & 2 \quad \sqrt{1 - i_b^2(x,t)} + \\ & + \quad i_b(x,t)[2\arcsin(i_b(x,t)) \pm \pi]. \end{aligned} \tag{2.41}$$

I start analizing the results obtained in the presence of a Gaussian noise source with $i_0 = 0.5$ and $i_b(x)$ homogeneous (empty symbols in the panel ($h1$)). In this panel of Fig. 2.6 it is evident the presence of two different dynamical regimes in each of these curves. An initial monotonic increasing behavior is followed by a constant MST plateau. This underlines the presence of two different mechanisms, governing the time evolution of the phase, which clearly appear in the soliton dynamics shown in Fig. 2.7. This picture displays four different phase dynamics during the passage towards the resistive state, i.e. when the phase φ approximately changes of 2π. The cells can escape from a potential well all together (panel (a) of Fig. 2.7) or by the formation of a single kink, or a single antikink, or a kink-antikink (K-A) pair (panel (c) of Fig. 2.7). If the string is too short, the connection among cells is so strong that the soliton formation is forbidden, the string can move from, or remain inside, a potential minimum as a whole. This is evident in panel (a) of Fig. 2.7. In this length regime, an increase in the number of cells makes

more difficult the motion of the whole string during the transition process, causing the MST to raise for short lengths. This happens as long as no soliton formation occurs. There is, in fact, a specific junction length above which the dynamics is governed by the formation of phase kinks. This length is connected with the soliton nucleation, that is the formation of a K-A pair. Following the work of Büttiker [81], in the soliton nucleation a critical nucleus, that is the minimum separation between kink and anti-kink, exists. For junction lenghts greater than this critical value it is evident a saturation effect. The MST reaches an almost constant value and the switching events are guided by the solitons, which indicates that the dynamics of these events is indipendent of the JJ length. To explain this behaviour, I consider that inside the string a subdomain structure exists. Each subdomain is composed by an amount of cells of total size approximately equal to the critical nucleus. The entire string can be thought as the sum of these subdomains and the overall escape event results to be the superimposition of the escape events of each single subdomain, so that the total MST is equal to the individual subdomain time evolution. The size of this subdomain approximately corresponds to the length value for which the initial monotonic behavior is interrupted. The dimension of the critical nucleus is proportional to $L_c \propto -\log(i_0)$. Increasing the i_0 value, the critical nucleus decreases and the soliton dynamics can start in correspondence of shorter junction lengths, as one can see in panel $(h1)$ of Fig. 2.6, where results obtained for $i_0 = 0.5$ (empty symbols) and $i_0 = 0.9$ (full symbols) are shown. In particular, $L_c \sim 5$ for $i_0 = 0.5$, and $L_c \sim 2$ for $i_0 = 0.9$. The curves obtained for $i_0 = 0.9$ are characterized by a small maximum, which reveals the presence of a weak nonmonotonic behavior. Between the initial increasing behavior and the saturation, a portion with negative slope and corresponding reduction of the MST is evident. Increasing the slope of the potential, the critical nucleus becomes shorter so that the nucleation is allowed also in regime of strong connections among the cells. These two conditions, i.e. anticipated nucleation and intense "bind" among cells, determine cooperating effects, which lead to MST reduction before the saturation regime is reached.

Panels b and c of Fig. 2.6 show MST curves obtained in the presence of CL and LS noise sources. These behaviors appear quite different with respect to those obtained using Gaussian noise sources. MST curves are strongly affected by Lévy flights that favour jumps between different potential valleys, and soliton formation (see panel (c) of Fig. 2.7, containing rapid and sudden phase variations). Specifically, for CL noise the saturation effect gives rise to a value of MST lower than that observed with the Gaussian thermal fluctuations. This is due to the peculiarity of the fat tails of PDF for CL noise. Therefore, for *homogeneous* density current (panel b), after the initial transient with an increasing behavior due to the increasing length of the junction and therefore of the string, nucleation and intense "bind" among cells speed up the escape process and τ decreases towards the saturation value. For *inhomogeneous* density current (panel e), the weak nonmonotonic behavior, found for homogeneous case (see panel b), disappears. This is because the edge portions of the phase string are subject to high values of bias current ($i_b(x) > 1$, see Fig. 2.4 and Eq. (4.10)). As a consequence, all the string is dragged out of the potential well, speeding up the escape process. The MST values obtained in the presence of LS noise sources are in general smaller than those obtained using noise sources with CL distribution. These differences are related to the intensity of the jumps in these two statistics. The saturation effect is also present, but the corresponding value of τ is very low. This is due to the LS Lévy flights, which push the string very fast out of the superconductive state, giving rise to a monotonic decreasing behavior of τ versus L. In other words, LS noise drives the phase string out of the potential well very quickly, due to the greater diffusive power of this noise source. It is worth noting that, for $i_0 = 0.9$, the values obtained using the Cauchy-Lorentz statistics

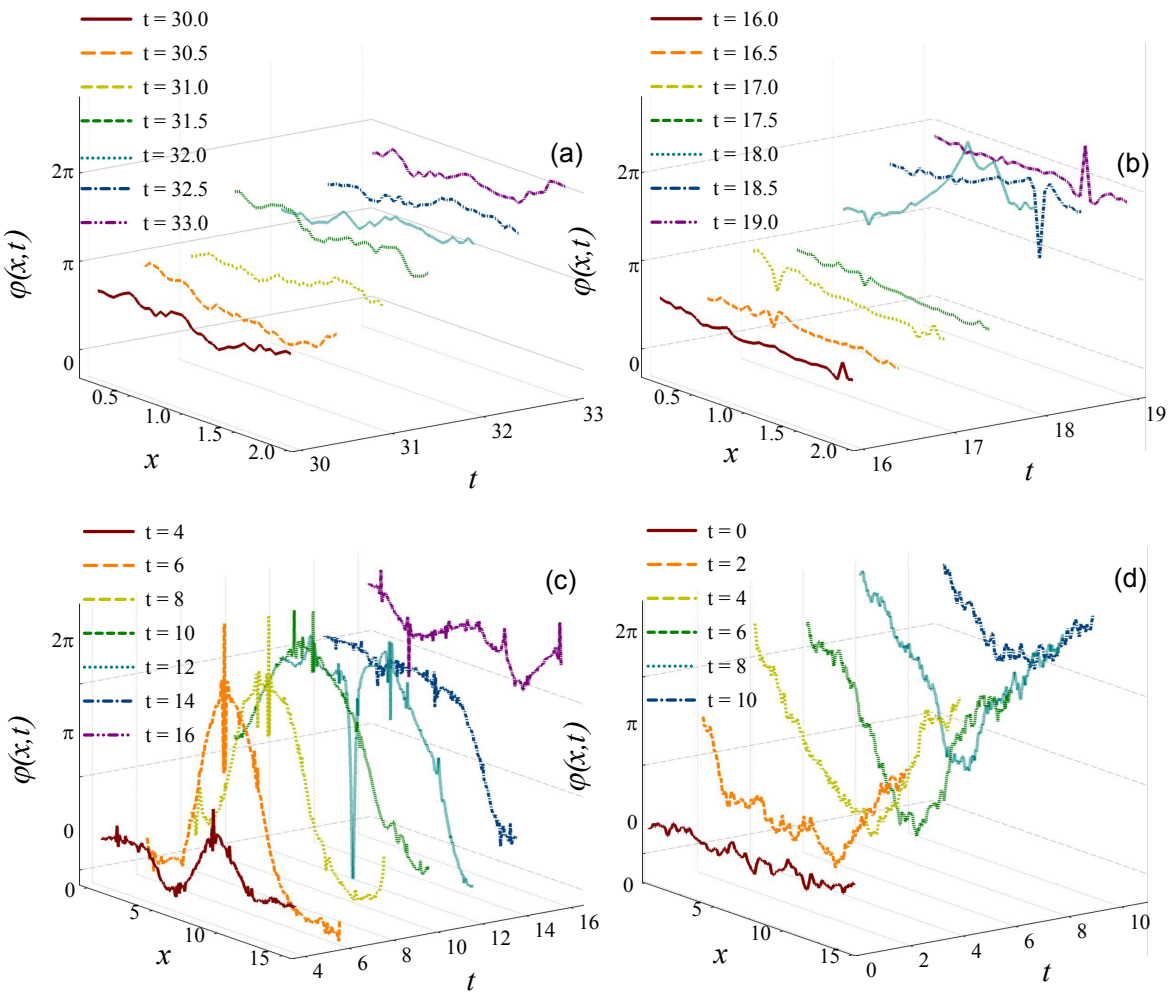

Figure 2.7: String dynamics during the switching towards the resistive state: for a JJ of length $L = 2$, with homogeneous bias current distribution and G noise source (panel (a)), inhomogeneous bias current distribution and CL noise source (panel (b)); for a JJ of length $L = 15$, with homogeneous bias current distribution and CL noise source (panel (c)), inhomogeneous bias current distribution and G noise source (panel (d)). All graphs were obtained for $\omega = 0.9$ and $\gamma = 0.2$. The curves in panels (b) and (c) show the characteristic Lévy flights of the CL statistic. [10]

are slightly greater than those obtained in the presence of Gaussian thermal fluctuations. This is connected with the *limited space displacement*, that rules the CL statistics for short time scale [11].

Panels d, e and f of Fig. 2.6 show results obtained in the presence of an inhomogeneous bias current. According to Eq. (4.10), $i_b(x)$ diverges at the string ends, $x = 0$ and $x = L$, having a minimum equal to $i_b(L/2) = 2/\pi \cdot i_0$ in the string center, $x = L/2$. In a considerable edge portion of the string (around 5% and 18% of the total length for $i_0 = 0.5$ and 0.9, respectively) $i_b(x) > 1$, allowing the phase elements to roll down along the tilted potential without encountering any resistance. These edge elements can be considered as *generators of solitons*. This corresponds to the physical situation in which the supercurrent flows between the junction ends and the fluxon formation occurs in these regions of the JJ. This kind of dynamics is shown in panel (d) of Fig. 2.7, in which the kink starts from the cells located in the junction edges. The role of these cells becomes particularly important as the length L increases, but is irrelevant for short junctions, in which the connection between cells is still too strong, and the dynamics is not guided by solitons. This situation is clear in panel (b) of Fig. 2.7, although the presence of CL

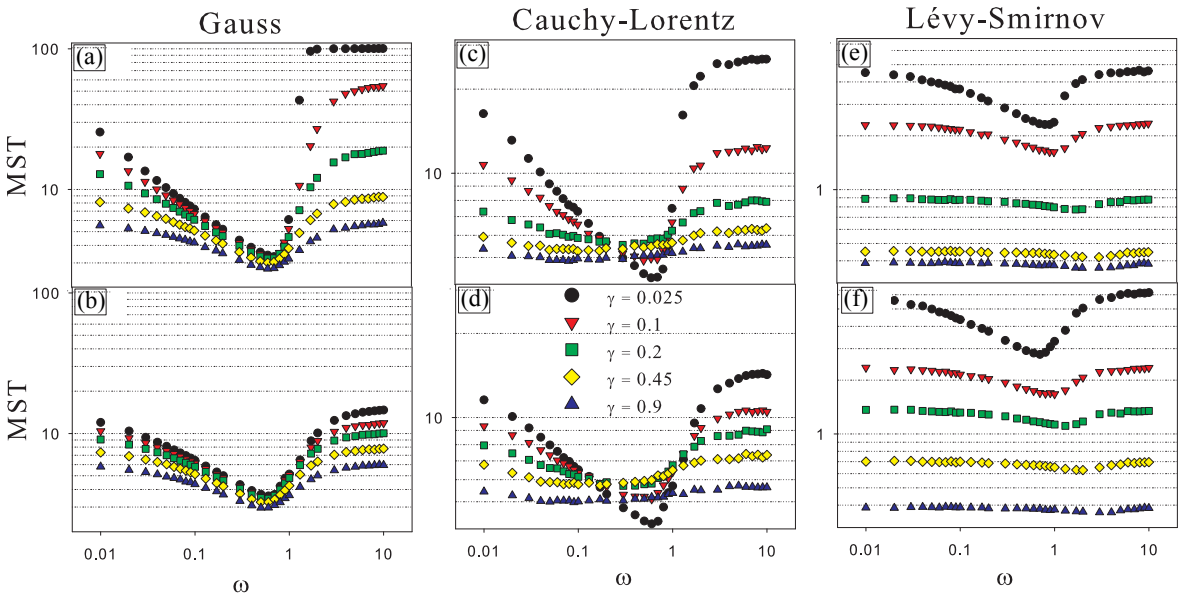

Figure 2.8: Log-log plots of MST τ *versus* ω obtained using: *homogeneous* $i_b(x)$ and noise sources G, CL and LS (panels a, c and e respectively); *inhomogeneous* $i_b(x)$ and noise sources G, CL and LS (panels b, d and f respectively). In all graphs the values of the other parameters are: $i_0 = 0.9$, $L = 10$ and $\gamma = \{0.025, 0.1, 0.2, 0.45, 0.9\}$. The legend in panel d refers to all panels. [10]

statistics causes the appearance of flights. The G curves in panel d of Fig. 2.6 show an increasing behavior similar to those obtained with homogeneous bias current distribution, even if the values reached are a little bit higher. Independently of the value of L, about 77% of the cells composing the junction has $i_b(x) < i_0$. Therefore, this percentage of cells should overcome potential barriers higher than those corresponding to the case of homogeneous bias current $i_b(x)$. This determines, in the absence of soliton formation, an increase of the escape time. Moreover, a nonmonotonic behavior is observed. After reaching the maximum, the MST curves decrease due to the action of the junction edges, which behave as generators of solitons. This effect accelerates the escape process, becoming more important as the value of L increases (see Fig. 2.4). For $i_0 = 0.9$, the time average of the barrier height is lower than in the case with $i_0 = 0.5$ and the switching process is faster.

The CL and LS results presented in panels e and f of Fig. 2.6 do not show remarkable differences with respect to those obtained with homogeneous current distribution, except for an enhancement in the MST for very short junction. The physical reason of this behaviour is the same as that discussed for the Gaussian case.

The curves in panels (b) and (c) of Fig. (2.7), obtained using a CL noise source, show peaks associated with the generations of the Lévy flights. As previously discussed, these noise induced fluctuations influence the switching events and the soliton formation. These graphs also clearly display the creation of another "structure", known as *breather* (see panel (b) for $t = \{18.5, 19\}$ and $x/\lambda_j \approx 1.5$, and panel (c)). This is a well-known localized solution of the SG equation consisting of a soliton-antisoliton pair and oscillating with an internal "breathing" frequency. The curves obtained by using non-Gaussian noise sources exhibit this kind of nonlinear "structures" (panel (b) and (c) of Fig. (2.7)).

2.5.2 MST vs driving frequency ω

In this section the MST behaviour, setting the bias current at $i_0 = 0.9$, and varying both the frequency ω of the driving signal (within the interval $[0.01, 10]$) and the noise

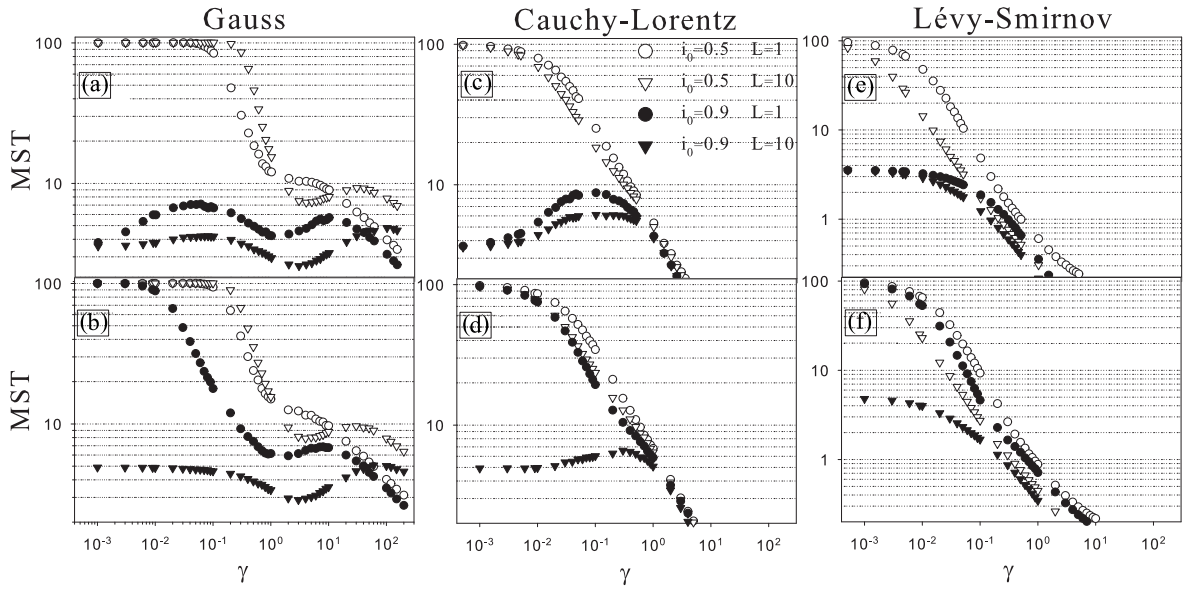

Figure 2.9: Log-log plots of MST τ *versus* γ obtained using: *homogeneous* $i_b(x)$ and noise sources G, CL and LS (panels a, c and e respectively); *inhomogeneous* $i_b(x)$ and noise sources G, CL and LS (panels b, d and f respectively). In all graphs the values of other parameters are: $i_0 = \{0.5, 0.9\}$, $\omega = 0.9$ and $L = \{1, 10\}$. The legend in panel c refers to all panels. [10]

intensity γ, is analyzed. The values of MST obtained are shown in Fig. 2.8. Specifically, results obtained in the presence of G, CL and LS noise sources are shown in the upper panels, a, c and e respectively, for homogeneous bias current distribution, and in the lower panels b, dand f respectively, for inhomogeneous bias current distribution. Each panel contains five curves, obtained for the values of γ displayed in the legend. This analysis was performed working with a junction of length $L = 10$, that is a string with a suitable length, which allows to onset the phenomenon of soliton formation. All graphs show clearly the presence of *resonant activation* (RA) [3, 4, 123–130], or *stochastic resonance activation*, a noise induced phenomenon, whose signature is the appearance of a minimum in the curve of MST *vs* ω. This minimum tends to vanish for CL and LS distributions when the noise intensities are greater than the time average of the potential barrier height ($\overline{\Delta U}_{i_0=0.9} \simeq 0.4$, see Eq. (2.41)). It is worthwhile to note that the nonmonotonic behavior of τ versus the CL noise intensity around the minimum, observed in panels c and dof Fig. 2.8, is related to that shown in panels c and d of Fig. 2.9. The RA is a phenomenon robust enough to be observed also in the presence of Lévy noise sources [11]. Particle escape from a potential well is driven when the potential barrier oscillates on a time-scale characteristic of the particle escape itself. Since the resonant frequency is close to the inverse of the average escape time at the minimum, which is the mean escape time over the potential barrier in the lower configuration, *stochastic resonant activation* occurs [9, 30], which is a phenomenon different from the *dynamic resonant activation*. This effect, in fact, appears when the driving frequency matches the natural frequency of the system, that is the plasma frequency [71, 72, 131]. Finally, the contemporaneous presence of RA and NES phenomena in the behavior of τ as a function of the driving frequency, in underdamped JJ, has been observed, finding that the MST can be enhanced or lowered by using different initial conditions [8].

The G data in panels a and b of Fig. 2.8 present this minimum for a frequency value ($\omega_{RA} \sim 0.6$) which varies little with the noise intensity γ. The only evident effect, switching to an inhomogeneous bias current, is a general reduction of the MST. The curves with CL noise present a clear minimum, shifted towards higher values of ω, with respect to that of the Gaussian case. This minimum tends to disappear increasing

the noise intensity. This is due to the influence of Lévy flights which, for strong noise intensities, drive the escape processes. As found in the presence of Gaussian noise, also in the case of CL statistics, using inhomogeneous $i_b(x)$ causes a general lowering in the MST values. For a weak noise signal, the Cauchy-Lorentz distributions are higher than the Gaussian ones: for low values of γ the jumps are not relevant, and the limited space displacement gives short phase fluctuations, making more difficult to escape from the potential wells. The MST calculated using LS sources are also governed only by the noise and present quite small values. Therefore, the RA effect is found only in the curve obtained for a very weak noise intensity.

By increasing the driving frequency, at low noise intensities, a trapping phenomenon occurs. A threshold frequency ω_{thr} exists such that for $\omega > \omega_{thr}$ the phase string is trapped within a region between two successive minima of the potential profile. In other words, the string can not move from the potential well to the next valley during one period T_0 of the driving current $A\sin(\omega t)$. As a consequence, the MST diverges in the limit $\gamma \to 0$. The value of the threshold frequency increases with increasing bias current and/or maximal current across the junction [4, 55, 132]. The threshold values for the following parameter values $i_0 = 0.9$ and $A = 0.7$ are estimated. Specifically, for Guassian thermal fluctuations $\omega_{thr} \gtrsim 1.8$, for CL noise source $\omega_{thr} \gtrsim 2.1$ and for LS noise source $\omega_{thr} \gtrsim 3$.

2.5.3 MST vs noise intensity γ

Here the MST curves calculated varying the noise amplitude in the range $[0.0005, 200]$ are analyzed. The results are shown in Fig. 2.9. Specifically the results in panels a, c and e were obtained, using an homogeneous $i_b(x)$ and G, CL and LS noise sources respectively, while those shown in panels b, d and f, using an inhomogeneous $i_b(x)$ and G, CL and LS noise sources respectively. This analysis is performed using $\omega = 0.9$ and two different values of L and i_0, i.e. $L = \{1, 10\}$ and $i_0 = \{0.5, 0.9\}$. Fixing the values of the system parameters, for $\gamma \to 0$ the curves for the three noise sources (G, CL and LS) converge to the same values, i.e. the deterministic lifetime in the superconducting state, which depend strongly on the bias current. When $\gamma \to 0$ and the potential is not too tilted, trapping phenomena occur and the MST tends to t_{MAX}. Increasing the noise intensity, the MST curves exhibit an effect of *noise enhanced stability* (NES) [4, 54–58, 133–141], a noise induced phenomenon consisting in a nonmonotonic behaviour with the appearance of a maximum. The stability of metastable states can be enhanced and the average life time of the metastable state increases nonmonotonically with the noise intensity. The observed nonmonotonic resonance-like behavior proves to be different from the monotonic one of the Kramers theory and its extensions [142–144]. This enhancement of stability, first noted by Hirsch et al. [145], has been observed in different physical and biological systems, and belongs to a highly topical interdisciplinary research field, ranging from condensed matter physics to molecular biology and to cancer growth dynamics [58, 146].

From Fig. 2.9, can be noted that in the curve obtained using a Gaussian noise source, homogeneous current distribution and high washboard inclination, $i_0 = 0.9$, two maxima are present in correspondence of $\gamma_{MAX}^{L=1} \cong \{0.06, 10\}$ for $L = 1$ and $\gamma_{MAX}^{L=10} \cong \{0.07, 100\}$ for $L = 10$. In view of understanding the physical motivations of these NES effect, the time evolution of the probability $P(t)$, as defined in Eq. (2.39), is calculated during the switching dynamics of the junction. I remember that $0 \leq P(t) \leq 1$, where the two extreme values indicate the resistive state ($P(t) = 0$) and the superconducting state ($P(t) = 1$).

The time evolution of $P(t)$ was calculated for $i_0 = 0.9$ and $\omega = 0.9$. The results,

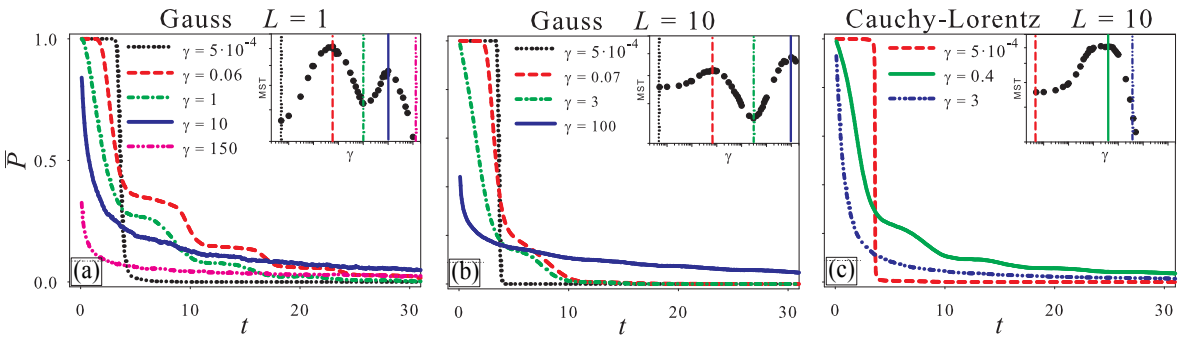

Figure 2.10: Time evolution of the probability $P(t)$ in the following conditions: G noise with $L = 1$ (panel a) and $L = 10$ (panel b); CL noise with $L = 10$ (panel c). The system parameters are $i_0 = 0.9$ and $\omega = 0.9$. Each graph contains curves of $P(t)$ obtained using values of γ for which a minimum or maximum appears in the τ *vs* γ behaviour. The insets reproduce the corresponding curves of panels a and c of Fig. 2.9. [10]

shown in Fig. 2.10, were obtained in the following conditions: i) G noise with $L = 1$ (panel a) and $L = 10$ (panel b); ii) CL noise with $L = 10$ (panel c). All panels of Fig. 2.10 contain curves of $P(t)$ calculated setting the noise intensity at values for which a maximum or minimum appears in the MST vs γ behaviour (see insets). Looking at the curves displayed in panel a, the dotted curve ($\gamma = 0.0005$) represents a deterministic switching event. The string after a quick escape does not return inside the first washboard valley. Conversely, the dashed line, obtained for $\gamma = 0.06$, describes a temporary trapping phenomenon. The contemporaneous presence of the fluctuating potential and noise source, inhibits the phase switching and therefore the passage of the junction to the resistive regime. Moreover the exit from the first well is not sharp, as in the deterministic case, and $P(t)$ assumes an oscillatory behavior, almost in resonance with the periodical motion of the washboard potential. This oscillating behavior of $P(t)$, which is related to the temporary trapping of the phase string, tends to disappear as the noise intensity increases. For $\gamma = 10$ (solid line in a of Fig. 2.10) another peak (NES effect) in the MST behaviour is observed, but no oscillations in $P(t)$ are present. At this value of γ, the JJ dynamics is totally driven by the noise and the NES effect is due to the possibility that the phase string returns into the first valley after a first escape event, as indicated by the fat tail of $P(t)$. This behaviour is strictly connected with that found for the MST, whose calculation is based on the definition of NLRT. Further increases of γ reduce for the phase string the possibility not only of returning into the intial well but also of staying for a long time inside it. The results for G noise source and $L = 10$, displayed in panel b of Fig. 2.10, are similar to those obtained for $L = 1$. The first hump, corresponding to $\gamma = 0.07$ (see inset of panel b) is a little bit smaller than that for $L = 1$ and $\gamma = 0.06$ (see inset of panel a), and this is consistent with the previous MST *versus* L analysis. Moreover a NES effect for $\gamma = 100$ is present (see inset of panel b). The difference of one order of magnitude in the noise intensity ($\gamma = 100$ for $L = 10$), respect to the NES phenomenon observed for $L = 1$ at $\gamma = 10$, can be noted. This difference is due to the greater difficulty for random fluctuations of carrying a string, ten times longer, again in the initial potential well. Panel c of Fig. 2.9 shows the curves of MST vs γ in the presence of CL noise source. Here the absence of the second peak, observed in the previous analysis at higher values of γ, can be noted. This discrepancy can be explained noting that, for low noise intensity, the effect of the CL flights on the overall JJ dynamics is neglegible, and the time evolution should appear quite similar to those observed with Gaussian noise. Conversely, due to the limited space displacement, to obtain the same effect (i.e. escape from the first potential well), junctions subject to CL

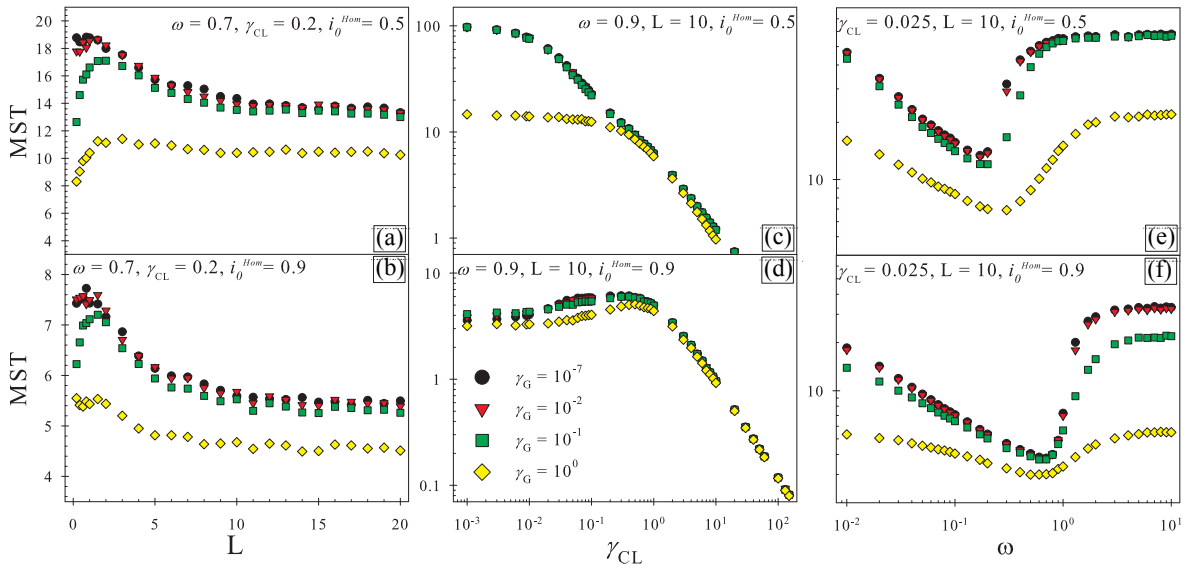

Figure 2.11: MST τ as a function of L, γ_{CL}, and ω. All curves were obtained considering the simultaneous presence of CL and thermal noise sources, using two different values, i.e. $i_0 = 0.5$ (top panels) and $i_0 = 0.9$ (bottom panels), of the homogenous bias current, and varying the Gaussian noise intensity, γ_{G}. The legend in panel d refers to all panels. [10]

noise should be exposed to noise intensity larger respect to identical junctions subject to G noise. The peak (maximum of MST) should be therefore shifted towards higher values of γ. Increasing the noise intensity, the influence of Lévy-flights on the total JJ dynamics becomes higher, and the probability that a second peak appears, similar to that observed in the presence of G noise, tends to vanish. This analisys is confirmed by the graph shown in panel c of Fig. 2.10. Conversely, LS flights are too intense to allow the formation of NES peaks (see panel e of Fig. 2.9). Finally, the curves obtained with inhomogeneous $i_b(x)$ do not present any differences, except those for $i_0 = 0.9$ and $L = 1$ (full circles), that show very high values of MST with respect to the case of homogenous current distribution. This indicates again a trapping phenomenon that occurs when a short junction undergoes very weak noise intensities ($\gamma \to 0$). In this case, the parts of the junction generating solitons do not affect the string dynamics. In fact, since $i_b(x) < i_0$ for 77% of the total length, a large percentage of the string remains confined in a potential well deeper than that of the analogous homogeneous case, thus determining the trapping effect.

Moreover, all the curves of MST vs γ for CL and LS noise sources coalesce together at high noise intensities. The MST has a power-law dependence on the noise intensity according to the expression

$$\tau \simeq \frac{C(\alpha)}{\gamma^{\mu(\alpha)}} \tag{2.42}$$

where the prefactor C and the exponent μ depend on the Lévy index α [76]. From Fig. 2.9, $\mu(\alpha) \sim 0.9$ for CL noise and $\mu(\alpha) \sim 1.2$ for LS noise, which are in agreement with the exponent $\mu(\alpha) \approx 1$ for $0 < \alpha < 2$, calculated for barrier crossing in bistable and metastable potential profiles [147, 148].

2.6 Simultaneous presence of Lévy noise and thermal fluctuations

In this section the presence of both thermal and Lévy noise sources is analyzed. Therefore, in Eqs. (2.25) and (2.26) both contributions of Gaussian thermal fluctuating current density $i_T(x,t)$ and non-Gaussian Lévy noise current density $i_{nG}(x,t)$ are considered. The Lévy contribution is restricted to a Cauchy-Lorentz term. The noise intensities are indicated by $\gamma_{\rm G}$ (Gaussian), ranging within the interval $[10^{-7},1]$, and $\gamma_{\rm CL}$ (Cauchy-Lorentz). Noise induced phenomena previously observed, when the CL noise source only is present, show now some differences. The values of the system parameters are chosen in such a way to highlight these changes. Fig. 2.11 contains a collection of MST curves obtained varying the junction lenght L (panels a and b), CL noise intensity $\gamma_{\rm CL}$ (panels c and d), and frequency of the oscillating bias current ω (panels e and f). Top and bottom panels show data calculated using $i_0 = 0.5$ and $i_0 = 0.9$, respectively. An overall reduction of the MST values is observed by increasing the intensity of thermal fluctuations, by speeding up the switching process between the superconductive and the resistive state. The simultaneous presence of thermal fluctuations and a Lévy noise source produces an increase of the overall intensity "felt" by the string phase. In all panels clear modifications of the nonmonotonic behavior are present, becoming more pronounced as the Gaussian thermal noise intensity increases, especially for $\gamma_{\rm G} > 10^{-1}$.

The analysis of MST vs L suggests that the soliton dynamics is modified only when the intensity of thermal fluctuations are greater than those of the CL noise, that is $\gamma_{\rm G} > \gamma_{\rm CL}$, conversely the curves for $\gamma_{\rm G} < \gamma_{\rm CL}$ overlap all together ($\gamma_{\rm G} \leq 10^{-1}$). The curves of the panels a and b maintain the structure already shown in panel b of Fig. 2.6 (see Sec. 2.5.1), that is a nonmonotonic behavior with a maximum and a saturation plateau. The saturation value of τ decreases, of course, with the increase of the intensity of thermal fluctuations.

Looking at the graphs of MST vs $\gamma_{\rm CL}$ (panel c), trapping phenomena are observed when $\gamma_{\rm CL} \to 0$ and $\gamma_{\rm G} \to 0$. For $\gamma_{\rm G} \geq 1$, that is when the Gaussian thermal noise intensity is comparable with the time average of the potential barrier height ($\overline{\Delta U}_{i_0=0.5} \simeq 1$, see Eq. (2.41)), trapping events disappear and thermally activated processes drive the switching events. For $i_0 = 0.9$ (panel d) all the curves show a nonmonotonic behavior, which is the signature of the NES effect. Low thermal noise intensities do not affect the behavior of the NES curve, with respect to the case of absence of thermal noise, till their value is lower than $\gamma_G \simeq 0.2$. This is the value of the CL noise intensity corresponding to the maximum of τ versus $\gamma_{\rm CL}$, $\gamma_{\rm CL}^{Max} \simeq 0.2$ (see panel c of Fig. 2.9). In other words, thermal fluctuations affect the behavior of NES curve for $\gamma_G \gtrsim \gamma_{\rm CL}^{Max}$. The maximum of the curve decreases and it is shifted towards higher CL noise intensities, because of the larger spatial region of the potential profile spanned by the phase string before reaching the boundaries $[-\pi,\pi]$.

For CL noise intensities $\gamma_{CL} \gtrsim 1$, all the curves of MST vs γ_{CL} (see panels c and d) coalesce together with a power-law behavior given by Eq. (2.42), with $\mu(\alpha) \sim 0.9$. When the structure of the potential profile becomes irrelevant for the dynamics of the phase string, that is when the noise intensity γ_{CL} is greater than the time average of the potential barrier heights ($\overline{\Delta U}_{i_0=0.5} \simeq 1$ and $\overline{\Delta U}_{i_0=0.9} \simeq 0.4$), the MST has a power-law dependence on the noise intensity.

The curves of MST as a function of ω in panels e and f of Fig. 2.11 reproduce the typical RA behavior (see panels c and dof Fig. 2.8). Again, all the curves of MST are lowered for increasing thermal fluctuation intensities. Specifically, for $i_0 = 0.5$ (panel e), the minimum of the curve decreases and it is shifted towards higher values of the driving

frequency. The resonant rate escape, that is the resonant frequency at the minimum, increases by increasing the overall noise intensity, being fixed the height of the average potential barrier ($\overline{\Delta U}_{i_0=0.5} \simeq 1$). For $i_0 = 0.9$ (panel f), there is not any potential barrier for about half period of the external driving force, and therefore the switching process is accelerated, and the position of the minimum is slightly affected by thermal fluctuations.

2.7 Conclusions

I have investigated the influence of both thermal fluctuations and external non-Gaussian noise sources on the temporal characteristics of long-overlap JJs. I studied how random fluctuations with different α-stable (or Lévy) distributions affect the superconducting lifetime of long current-biased Josephson junctions. The study was performed within the framework of the sine-Gordon equation. Specifically I analyzed the mean switching time (MST) of the phase difference across the junction, from a minimum of the tilted washboard potential, as a function of different parameters of the system and external random and periodical driving signals. I found nonmonotonic behaviors of the superconducting lifetime τ as a function of noise intensity γ, driving frequency ω and junction length L.

In particular, in the behaviour of the MST, I observed noise induced phenomena such as *stochastic resonant activation* and *noise enhanced stability*, with different characteristics depending on both the bias current distribution along the junction and the length of the superconducting device. Moreover, temporary trapping of the phase string in the metastable state with Gaussian thermal and CL noises gives rise to an oscillating behavior of the time evolution of the probability $P(t)$. The analysis of the MST as a function of the junction length revealed that the *soliton dynamics* plays a crucial role in the switching dynamics from the superconducting to resistive state. In more detail, I studied the relationship between creation and propagation of solitons and different features of the mean switching time. This analysis has demonstrated the existence of two different dynamical regimes. One, occurring for short junction, is characterized by the movement of the phase string as a whole. The other one, occurring for junction whose size exceeds a critical length, in which the kink (or antikink) creation is allowed.

Moreover, for high values of the bias current, there is a length in which the two regimes take place simultaneously. Finally I found that, choosing an inhomogeneous distribution of the bias current along the junction, the cells located at the junction edges behave as generators of solitons. In these conditions the escape from the metastable superconducting state is strongly affected by the soliton dynamics. The analysis of the contemporaneous presence of Cauchy-Lorentz and thermal noise sources gives rise to modifications in the soliton dynamics and noise induced effects observed in the transient dynamics of JJs in the presence of non-Gaussian, Lévy type noise sources. Moreover oscillating pairs of soliton-antisoliton (*breathers*) induced by the noise have been observed.

Our findings, which are important to understand the physics of fluctuations in long-overlap Josephson junctions to improve the performance of these devices, could help to shed new light on the general context of the nonequilibrium statistical mechanics. In fact, JJs are good candidates for probing relevant physics issues in metastable systems [8]. Moreover, the mean switching time from one of the metastable states of the potential profile encodes information on the non-Gaussian background noise. Therefore, the statistical analysis of the switching times of JJs can be used to analyze weak signals in the presence of an unknown non-Gaussian background noise.

The results presented in this chapter are published in Ref. [10].

Chapter 3

Long JJ: breathers detection

I consider a long Josephson junction excited by a suitable external ac-signal, in order to generate, control and detect breathers. Studying the nonlinear supratransmission phenomenon in a nonlinear sine-Gordon sinusoidally driven chain, Geniet and Leon [12, 13] explored the bifurcation of the energy transmitted into the chain and calculated a threshold $A(\omega)$ for the external driving signal amplitude, at which the energy flows into the system by breathers modes. I numerically study the continuous sine-Gordon model, describing the dynamics of the phase difference in a long Josephson junction, in order to deeply investigate the "continuous limit" modifications to this threshold. Wherever the energy flows into the system due to the nonlinear supratransmission, a peculiar breathers localization areas appear in a (A, ω) parameters space. The emergence of these areas depends on the damping parameter value, the bias current, and the waveform of driving external signal. The robustness of generated breathers is checked by introducing into the model a thermal noise source to mimic the environmental fluctuations. Presented results allows one to consider a cryogenic experiment for creation and detection of Josephson breathers.

The chapter is structerd as follows. Section 3.1 presents an introduction about the phenomenon of nonlinear supratransmission, recalling the JJ frameworks in which this effect cames into view. Section 3.2 contains details about the SG model and the description of the driving signal used to excite breathers into the system. The collection of results is presented in section 3.3, including a deep discussion about the emerging features. In section 3.4 the conclusions are drawn.

3.1 Nonlinear supratransmission and breathers

The behavior of a nonlinear system excited by an external sinusoidal driving and the bifurcation of the energy transmission into the system were deeply studied by Geniet and Leon [12, 13]. The Floquet theorem [149] states that, for linear waves in a periodic structure, a forbidden gap of frequency exists. The frequency gap between acoustic and optical branches in the vibration modes of a diatomic chain well embodies this picture. Waves with frequencies within this forbidden range esponentially vanish in the medium (evanescent waves). In nonlinear systems excited by plane waves, the appearance of gap solitons [150] and the localization of energy due to nonlinear instability are matter of many systems [151–156]. If the nonlinear medium, characterized by a forbidden band gap (FBG), is irradiated to one end by a sinusoidal drive, with frequency within the gap, the energy transmission can be supported. This phenomenon is called *nonlinear supratransmission* (NST) and is nowadays reported in several other contexts, from Bragg media [157, 158], coupled-wave-guide arrays (nonlinear Schrödinger model) [159, 160],

optical waves guide arrays [161], Fermi-Pasta-Ulam model [162], Klein-Gordon (KG) electronic network [163], chains of coupled oscillators [164], discrete inductance-capacitance electrical line [165] to generic multicomponent nonintegrable nonlinear systems [166]. The manifestation of NST in both SG and KG equations, points out that this process is not dependent on the integrability, but is a feature of systems possessing a natural forbidden band gap. Geniet and Leon found a very simple rule proving an explicit formula for the bifurcation diagram in the (ω, A) parametric space: the energy flows into the medium as soon as the amplitue A of the driving, at frequency ω, exceeds the maximum amplitude of the static breather of the same frequency. This energy then travels through the system by means of plasma waves and nonlinear localized excitations, that is solitons, antisolitons and breathers. Geniet and Leon extended the results, obtained for a SG chain, to its continuous version, used to describe a long Josephson junction (LJJ) whose extremity is subjected to a sinusoidal excitation (*Neumann boundary condition*). The soliton solutions are strongly stable, maintaining their shape after collisons or reflections, and producing clean evidences in the I-V characteristics of the junction. A breather is another travelling SG solution formed by a soliton-antisoliton bounded couple, oscillating in an internal frame with a proper internal frequency. The magnetic flux associated with a breather is zero, as the voltage difference across the junction. Indeed, considering that the time variations of φ produce a voltage difference across the junction according to the a.c. Josephson relation, the rapid oscillations of the breather phase results in a mean voltage close to zero (or beyond the sensitivity of nowadays high frequencies oscilloscopes). Other pratical difficulties exist: i) a breather has to be efficently generated and trapped, for a sufficent long time, in a confined area to allow measurements, ii) it decays esponentially in time, even more so considering the damping affecting the system, and iii) an applied bias current tends to split the breather in a soliton/antisoliton couple. These are the reasons that underlie the lack of experimental evidences and confirmations of breathers in LJJ. Observations of breathers, called *rotobreathers*, in Josephson junctions (JJ) are reported only using "Josephson ladders", i.e. a ladder composed by small JJs [167–171]. Our investigation points towards an experimental setup devoted to the exclusive generation and detection of breathers in LJJ. The influence of the environment should be take into account to well describe a real experimental framework. Bodo *et al* [14, 163, 172] enhanced the deterministic analisys developed by Geniet and Leon in a discrete SG chain, using a sinusoidal excitation corrupted by an additive white Gaussian noise. Considering driving amplitude below the critical value, they highlighted the generation of noise induced breathers, with a probability depending on the noise intensity. To check the robustness of the generated breathers, a Gaussian white source is added to the perturbed SG model, to mimic the environment effect on the breather's dynamics. The percentage of surviving breather, including a white noise source of given amplitude, is calculated.

3.1.1 The nonlinear SG chain

The pioneers in the context of NST were Geniet and Leon [12, 13]. They explored the bifurcation of energy transmitted in a discrete SG chain composed by N damped coupled oscillators, initially at rest

$$\ddot{u}_n - c^2(u_{n+1} - 2u_n + u_{n-1}) + \sin u_n = -\gamma(n)\dot{u}_n \qquad n = 1, ..., N \tag{3.1}$$

with *Dirichlet boundary condition* at the origin of the chain,

$$u_0(t) = A\sin(\omega t) \qquad u_n(0) = 0 \qquad \dot{u}_n(0) = 0. \tag{3.2}$$

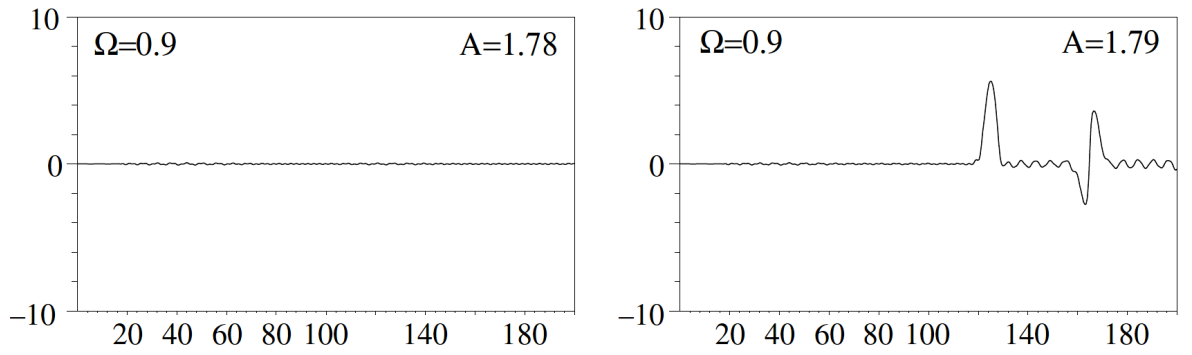

Figure 3.1: Representation of $u_n(t)$ as a function of time for $n = 60$ in the case $\omega = 0.90$ for two amplitudes. [12]

The damping coefficent γ is used to model a semi-infinite chain with an absorbing boundary. The parameter C is the coupling factor. Geniet and Leon [12, 13] deduced, exciting the JJ in the forbidden frequencies gap ($\omega < 1$), a threshold $A_s(\omega)$

$$A_s(\omega) = 4 \arctan \left[\frac{\mathrm{C}}{\omega} \operatorname{arccosh} \left(1 + \frac{1 - \omega^2}{\omega} \right) \right], \tag{3.3}$$

above which NST accours and the system permits the energy transmission by means of nonlinear modes generation (breathers, kinks, antikinks).

Geniet and Leon checked the qualitative definition of the bifurcation threshold by means of numerical simulations of Eq. (3.1) with the boundary condition Eq. (3.2) by varying, at given frequency ω, th amplitude A around the above value $A_s = 1.803$ (for $\mathrm{C} = 4$). Observing the motion of only one element of the chain, the appearence of NST can be easily proved. In Fig. 3.1 the motion of the 60th site of a chain, composed by 200 elements driven at frequency 0.9 at amplitudes $A = 1.78$ (no NST) and $A = 1.79$ (NST) for a coupling factor $\mathrm{C}^2 = 16$, is shown. Each large oscillation in the right panel of Fig. 3.1 corresponds to a breather passing by the site. Two of them are generated and cross the site 60 at times 120 and 160.

The Fig. 3.2a shows, by systematic exploration of the chain, the lowest A values for which NST is seen in numerical simulations, and it is obtained for 200 particles with a coupling $\mathrm{C}^2 = 100$ for a typical time of 200. The points in this figure are compared to the theoretical threshold expression 3.2 (continuous curve). Good agreement, between calculation and theoretical predictions, exists, apart for the discrepancies for A values within the range $[0.18 - 0.33]$.

Moreover, Geniet and Leon numerically evaluated the energy flowing into the system [13], for a generic nonlinearity deriving from a potential energy $V(u_n)$ (for the SG case $V(u_n) = 1 - \cos u_n$). Starting from the energy density

$$H_n = \frac{\dot{u}_n^2}{2} + \frac{\mathrm{C}^2}{2}(u_{n+1} - u_n)^2 + V(u_n) \qquad n = 1, ..., \infty \tag{3.4}$$

and considering the evolution equation, that follows the conservation law

$$\frac{\partial H_n}{\partial t} + (J_{n+1} - J_n) = 0 \tag{3.5}$$

with the current

$$J_n = -\mathrm{C}^2 \dot{u}_n (u_n - u_{n-1}), \tag{3.6}$$

the total energy of the system reads

$$E = \sum_{n=1}^{\infty} H_n + \frac{\mathrm{C}^2}{2}(u_1 - u_0)^2, \tag{3.7}$$

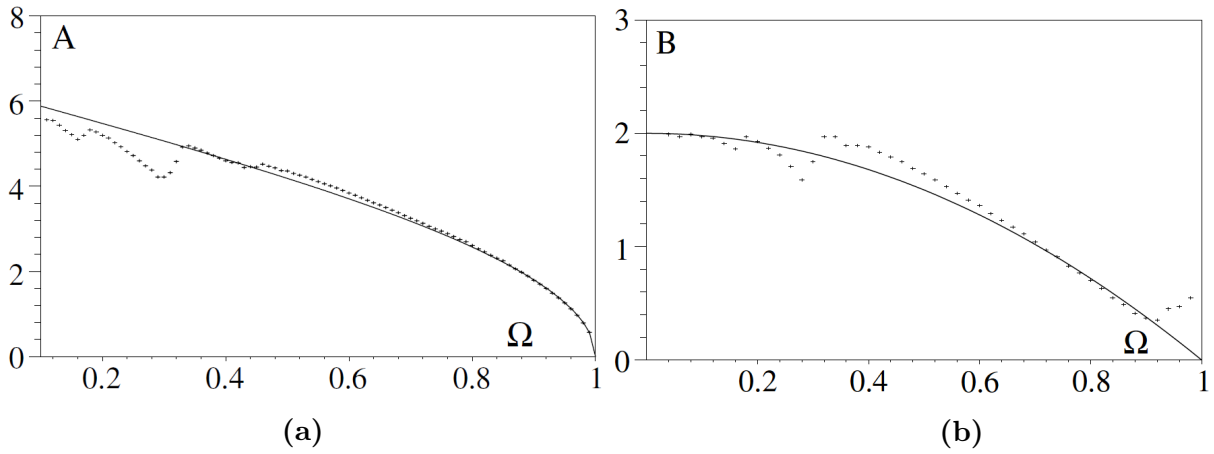

Figure 3.2: The bifurcation diagrams in the (A, ω) plane. The crosses indicate the lowest values of amplitude for which nonlinear supratransmission is seen in numerical simulations. a) Discrete SG chain, the solid curve is the threshold Eq. (3.3). b) Continuous SG, the solid curve is the threshold Eq. (3.13). [12]

including also the potential energy associated with the coupling between the first particle u_1 and the boundary u_0. The chain is supposed infinite with $u_n(t) \to 0$, that is $J_n \to 0$, as $n \to \infty$.

Taking the time derivative

$$\frac{\partial E}{\partial t} = \sum_{n=1}^{\infty} \frac{\partial H_n}{\partial t} + \mathrm{c}^2 \dot{u}_1(u_1 - u_0) + \mathrm{c}^2 \dot{u}_0(u_0 - u_1) = \sum_{n=1}^{\infty} \frac{\partial H_n}{\partial t} - J_1 + \mathrm{c}^2 \dot{u}_0(u_0 - u_1) \quad (3.8)$$

and using the Eq. (3.5) to explicit the sum over n of H_n

$$\frac{\partial H_1}{\partial t} + \frac{\partial H_2}{\partial t} + \ldots + \frac{\partial H_n}{\partial t} = (J_1 - \cancel{J_2}) + (\cancel{J_2} - \cancel{J_3}) + \ldots + (\cancel{J_n} - J_{n+1}) = J_1 - J_{n+1},$$

the Eq. (3.8) becomes

$$\begin{aligned} \frac{\partial E}{\partial t} &= [J_1 - J_{n\to\infty}] - J_1 + \mathrm{c}^2 \dot{u}_0(u_0 - u_1) = -J_{n\to\infty} + \mathrm{c}^2 \dot{u}_0(u_0 - u_1) = \\ &= \mathrm{c}^2 \dot{u}_0(u_0 - u_1). \end{aligned} \quad (3.9)$$

The energy injected E_i into the system during a time T is

$$E_i = \mathrm{c}^2 \int_0^T \dot{u}_0(u_0 - u_1) dt. \quad (3.10)$$

The continuous version of the Eq. (3.1) subjected to a costant torque, for the variable $x = n/\mathrm{c}$ and $1/\mathrm{c} \to 0$, is

$$u_{tt} + \gamma u_t + \sin u = i_b + u_{xx}. \quad (3.11)$$

Including the boundary condition, called *Neumann bundary condition*

$$\partial_x u|_{x=0} = B \sin(\omega t) \quad (3.12)$$

the resulting threshold is [12, 13]

$$B_s = 2(1 - \omega^2). \quad (3.13)$$

The B_s expression is calculated imposing that the system adapts its phase profile to the breather derivative, i.e. the derivative of the Eq. (2.9), at the boundary $\partial_x u|_{x=0} =$

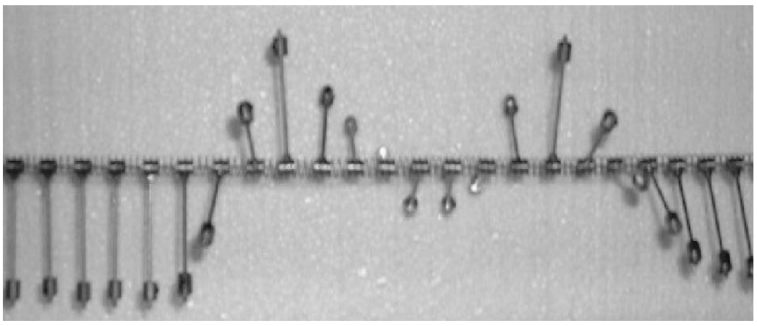

Figure 3.3: Picture of a breather generated in a mechanical pendula chain driven at one end at a frequency in the forbidden band gap. [13]

$\partial_x u_b|_{x=0}$. Varying the position of the breather's center to maximize $\partial_x u_b|_{x=0}$, the simple expression for the maximum amplitude (see Eq. (3.13)) is obtained. Geniet and Leon solved the discrete system, with no applied bias ($i_b = 0$), for a chain of 60 particles with an absorbing boundary on the last 30, and with a coupling factor $c^2 = 25$. The results in Fig. 3.2b show good agreement with the theoretical threshold B_s, except perhaps the low frequencies and close to the plasma (phonon) band ($\omega \sim 1$).

They also experimentally realized the phenomenon of NST, using a mechanical pendula chain driven on a boundary by a periodic torque [13]. A picture of the breather generated by the boundary driving at the frequency in the FBG is shown in the Fig. 3.3. This breather is obtained using a chain formed by 48 pendula of angular eigenfrequency $\omega_0 = 15$ Hz (upper value of the FBG) by driving the system at frequency 12.7 Hz, corresponding to $\omega = 0.85$ in normalized units. The measured coupling costant was $c = 32$.

Bodo *et al* [14, 172] enhanced the deterministic analysis described hitherto, studying noise induced breathers, in an externally driven SG chain, excited using a driving sugnal with amplitude below the deterministic threshold. They considered a driving sinusoidal excitation "corrupted" by a white Gaussian noise $\eta(t)$ of root mean square (RMS) value, replacing the first boundary condition in Eq. (3.2) with:

$$u_0(t) = e^{-\frac{t-t_0}{20\pi/\omega}} \left[A sin(\omega t) + \eta(t)\right] H(t - t_0) \tag{3.14}$$

where $H(t)$ is the Heaviside function and t_0 corresponds to the time at which the breather reaches the 50th cell. With this modified boundary condition, only one breather can be generated. In order to investigate the noise influence on the NST, they calculated over 200 numerical realizations the probability to generate a breather mode as a function of the RMS. The results vaying the amplitude of the sinusoidal driving are shown in Fig. 3.4a. The curves contained in this picture have a staircase profile. The probability to find a breather is first zero, but, reached a RMS critical value, rapidly increases until a breather is definitely generated. In order to determine the appropriate amount of noise for generating a breather, two RMS critical values $\sigma_{10\%}$ and $\sigma_{90\%}$ are defined, corresponding to the noise intensity giving probabilities of 10% and 90%, respectively. The corresponding curves are shown in Fig. 3.4b. Below the first curve, the noise is not sufficient to generate a breather, conversely beyond the second curve a breather is surely induced into the medium. Between these two curves, a breather is created with a probability in the range $[\sigma_{10\%}; \sigma_{90\%}]$.

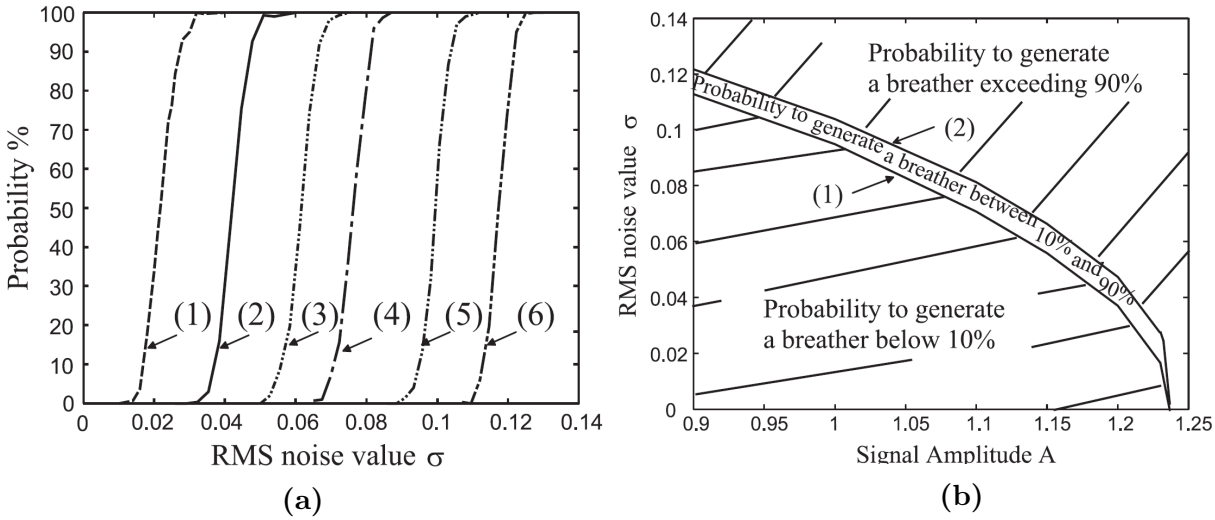

Figure 3.4: a) Probability of generating a breather versus the RMS noise amplitude for different amplitudes of the sinusoidal driving. The probability is estimated over 200 simulations. (1) $A = 1.23$, (2) $A = 1.2$, (3) $A = 1.15$, (4) $A = 1.1$, (5) $A = 1$, (6) $A = 0.9$. b) Bifurcation diagram of the SG chain subjected to a noisy sinusoidal excitation. (1) Critical noise value $\sigma_{10\%}$ for which a breather is generated with 10% probability versus the amplitude. (2) Critical noise value $\sigma_{90\%}$ for which a breather is generated with 90% probability versus the amplitude. These two critical curves define three regions of parameters that allow us to generate a breather with a given probability. Parameters: $N = 4000$, $m = 500$, $b = 140$, $\omega_0 = 1$, $c = 10$, $\Omega = 0.95$. . [14]

3.2 The continuous SG model

To describe the dynamics of the LJJ used to generate breathers, the SG equation [62, 79] is used, including the quasiparticle tunneling term and an additional stochastic contribution $i_{TN}(x,t)$, but neglecting the surface resistance of the superconductors,

$$\varphi_{tt}(x,t) + \gamma\varphi_t(x,t) - \varphi_{xx}(x,t) = i_b - \sin(\varphi(x,t)) + i_{TN}(x,t), \tag{3.15}$$

where a simplified notation has been used, with the subscripts of φ indicating the partial derivative in that variable. The SG equation is expressed in terms of the dimensionless x and t variables, that are the space and time coordinates normalized respectively to the Josephson penetration depth λ_J and to the inverse of the plasma frequency ω_p of the junction. The damping parameter is $\gamma = (\omega_p R_N C)^{-1}$, and it will be set hereafter to a small value to work in underdamped regime, in particular $\gamma \leq 0.5$. Higher damping parameters drastically and rapidly reduce the amplitude and the velocity of the breathers, making it hard to detect them.

Eq. (3.15) is solved imposing the following boundary conditions

$$\varphi_x(0,t) = f(t) \qquad \varphi_x(L,t) = 0 \tag{3.16}$$

where $f(t)$ is the external driving pulse used to excite the LJJ and generate the breathers.

3.2.1 The driving signal

Previous authors [12, 14] studied a junction excited by a sinusoidal external signal. Gaussian or rectangular pulses irradiating the system cannot generate breather modes, but can excite only solitons and antisolitons. Indeed, recalling the relation between the external magnetic field and the $x-$derivative of the phase (see Eq. (2.22)), a Gaussian pulse resembles the profile of the $x-$derivative of a soliton, i.e. a fluxon (see Fig. 2.3b).

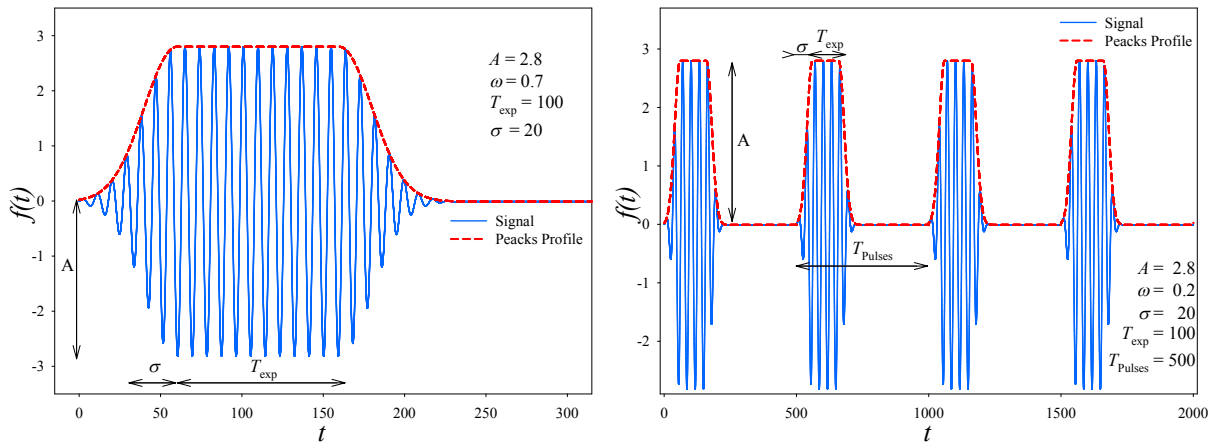

Figure 3.5: a) External sinusoidal pulse, with amplitude smoothly increasing/reducing according to Gaussian profiles during the switching on/off regimes of the pulse. b) Train of identical modulated sinusoidal pulses spaced by T_{Pulses}.

Instead, the $x-$derivative of a breather is more similar to an oscillation period of a sinusoidal envelope. For this reason a sinusoidal signal have to be used to excite breather modes. In our model, one end of the junction is driven by a sinusoidal pulse $f(t)$

$$f(t) = A(t)\sin(\omega t). \tag{3.17}$$

with amplitude $A(t)$ and frequency ω lower than 1, that is, due to the time normalization, lower than the JJ plasma frequency ω_p:

To well reproduce a meaningful experimental signal, see Fig. 3.5a, that is without abrupt variations during the switching on/off regimes, the driving amplitude $A(t)$ is smoothly increased/reduced according to Gaussian profiles:

$$A(t) = \begin{cases} A \quad e^{-\frac{(t-T_-)^2}{\sigma^2}} & with \quad t < T_- \\ A & T_- \leq t \leq T_+ \\ A \quad e^{-\frac{(t-T_+)^2}{\sigma^2}} & with \quad t > T_+ \end{cases}$$

where A is the maximum amplitude, $T_\pm$ and σ are the centers and the tails of the Gaussian envelopes, respectively, so that the pulse duration is $T_{exp} = T_+ - T_-$. Hereafter, the value of the Gaussian tails will be imposed to $\sigma = 20$. A real experimental realization needs a train of identical pulses, to exite the multiple generation of breathers. The signal to use is shown in Fig. 3.5b, where T_{Pulses} is the distance between consecutive pulses.

3.3 Numerical results

The deterministic analysis is carried out setting $i_{TN}(x,t) = 0$ in the Eq. (3.15). The lenght of the junction is hereafter imposed to $L = 50\lambda_J$, a typical value for the commonly used LJJ. The integration of the stochastic differential Eq. (3.15) is performed, within the Ito scheme, by a finite difference method. Time and space steps are $\Delta x = \Delta t = 0.005$ and the maximum observation time is set to $T_{max} = 300$. As initial condition, the string is at rest in the first washboard potential valley.

The analysis is performed varying the driving amplitude A and frequency ω in the ranges $A \in [0 - 2.5]$, with $\Delta A = 0.01$, and $\omega \in [0 - 1]$ (i.e. $\omega \leq \omega_p$ in not normalized units), with $\Delta\omega = 0.01$, respectively.

To follow the evolutions of breathers, it is easier to focus the attention only on one element, i.e. a cell, of the string. To avoid misreading due to boundary reflections, a reference cell far from the edges is chosen, in our analysis $x_{ref} = 20$. To detect a breather is useful calculate the time average of the phase of this reference cell, $\overline{\varphi}_{x_{ref}}$, and the dispersion of the $\varphi_{x_{ref}}(t)$ values from this average value, that is the standard deviation (SD), $\sigma_{\overline{\varphi}}$. Three different cases can arise:

1. $\overline{\varphi}_{x_{ref}} \simeq 0$ and $\sigma_{\overline{\varphi}} \simeq 0$
   absence of NST, there are not nonlinear excitations travelling through the medium;

2. $\overline{\varphi}_{x_{ref}} \simeq 0$ and $\sigma_{\overline{\varphi}} \lesssim 1$
   only breathers are excited;

3. $\overline{\varphi}_{x_{ref}} \gg 1$ and $\sigma_{\overline{\varphi}} \gg 1$
   every combinations of solitons, antisolitons and breathers travell through the medium.

A refined bifurcation diagram can be create by plotting the $\sigma_{\overline{\varphi}}$ as a function of (A, ω), neglecting the $\sigma_{\overline{\varphi}} \gg 1$ values obtained in presence of at least one moving soliton (case 3). A collection of these diagrams is presented in the left panels of the Figs. 3.6, 3.8 and 3.9. A different bifurcation diagram can be obtained by plotting the energy injected E_i into the system, according to Eq. (3.10), as a function of (A, ω). A collection of these diagrams is presented in the right panels of the Fig. 3.6, 3.8 and 3.9.

The panels of the Fig. 3.6 are obtained setting the damping parameter $\gamma = 0.02$ and the bias current $i_b = 0.0$, and varying the duration of the external pulse, so that $T_{exp} = \{1$ (panels a and b), 5 (c and d), 10 (e and f), 20 (g and h), 35 (i and l)$\}$. In each left panel, the light grey background indicates the absence of breathers modes exclusively generated into the junction. In detail, for low (A, ω) values (below the threshold B_s, see Eq. (3.13)) there is not NST effect (case 1), while above the threshold every kind of nonlinear excitations can propagate through the medium. The colored spots highlight the exclusive presence of breathers (case 2), resulting in a new and unexpected localization of the breathers in *branches*. Plasma waves, generated by the external signal and resulting from the breathers decay, are also observed with the breathers. Between these breathers-branches, every combination of kinks, antikinks, breathers and plasma waves are detected, but due to the stable nature of solitons and the damping of the medium, after a short time only soliton solutions survive inside the system. The branches for high amplitude values, that is $A \gtrsim 1$, corresponde to multiple generation of stationary and moving breathers. The situation for low frequencies (~ 0.2) and high amplitude is consistent with Geniet and Leon's results [12].

The analisys of the energies injected into the system is displayed in the right panels of Fig. 3.6. Each of them shows a large black area, sign of the lack of NST (no energy flows into the system). Over the bifurcation threshold, the energy flux is evidenced by a colorful region, in which branches structures, similar to that found in the $\sigma_{\overline{\varphi}}$ diagrams, can be noted. The breathers tend to localize in "border regions" where E_i significantly changes (i.e. between areas with a color change). Moreover, this suggests that the breathers prefer to localize into isoenergetic regions of (A, ω) parameter space, where the energy is slightly lower than the sorrounding areas. In these more intense (from the energetic point of view) sorrounding regions, solitons and antisoliton can be generated. Indeed, according to the Eq. (2.20), the energy of a breather is lower than the energy of

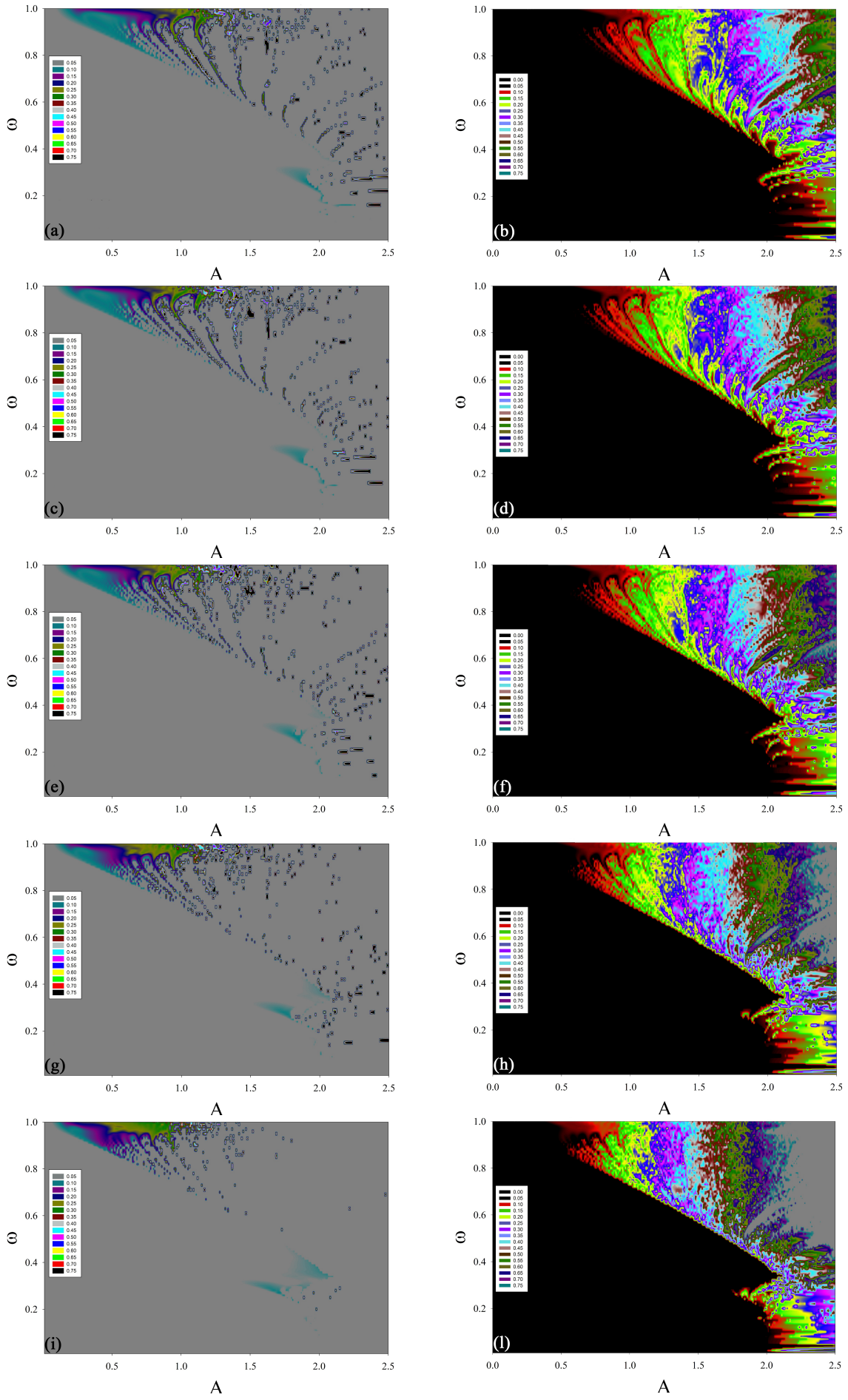

Figure 3.6: Bifurcation diagrams for $\sigma_{\overline{\varphi}}$ (left panels) and injected energies E_i (right panels) as a function of amplitude A and frequency ω of the driving signal, setting $\gamma = 0.02$ and varying the duration of the pulse T_{exp}. From the top, $T_{exp} = \{1$ (panels a and b), 5 (c and d), 10 (e and f), 20 (g and h), 35 (i and l)$\}$.

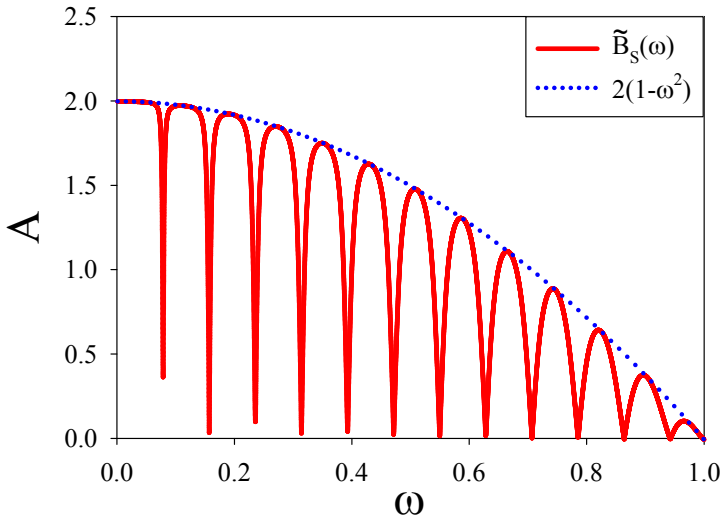

Figure 3.7: Bifurcation thresholds Eq. (3.13) [13] and 3.22, setting $t = T_{exp}$.

a kink-antikink couple. I can suppose that breathers are generated if E_i is within the range $[E_b; 2E_s[$ (see Eq. (2.20), that is:

$$E_b = 16\gamma\sqrt{1-\omega^2} \leq E_i < 16\gamma = 2E_s. \tag{3.18}$$

Increasing the pulse duration T_{exp}, more energy comes into the system, and the breathers branches tend to disappear, because the condition expressed by the Eq. (3.18) is hardly realized.

The breathers branches seems start from well-defined points of the bifurcation threshold. Following [12], Eq. (3.13) is obtained supposing that, at the boundary, the system adapts to the stationary breather derivative centered in $(-x_0)$, $\partial_x\varphi(x,t)|_{x=0} = \partial_x\varphi_b(x,t)|_{x=0}$, that is

$$\varphi_b(x,t) = 4\arctan\left\{\frac{k}{\omega}\frac{\sin(\omega t)}{\cosh\left[k(x-x_0)\right]}\right\} \tag{3.19}$$

$$\partial_x\varphi_b(x,t)|_{x=0} = 4\frac{k^2}{\omega}\frac{\sin(\omega t)\sinh(kx_0)}{\cosh^2(kx_0)+k^2/\omega^2\sin^2(\omega t)}. \tag{3.20}$$

Here, $\omega^2 + k^2 = 1$ is the dispersion relation for evanescent waves. Varying the position x_0, Eq. (3.20) has a maximum for $x_0 = x_m$ given by

$$\sinh^2(kx_m) = 1 + k^2/\omega^2.$$

so that:

$$\partial_x\varphi_b(x,t)|_{x_0=x_m} = 2\frac{k^2}{\omega}\frac{\sin(\omega t)}{\sqrt{1+\frac{k^2}{\omega^2}\sin^2(\omega t)}}. \tag{3.21}$$

The expression of the threshold B_s is obtained by calculating the maximum amplitude of Eq. (3.21), i.e. imposing $sin(\omega t) = 1$,

$$B_s = 2\frac{k^2}{\omega}\frac{1}{\sqrt{1+k^2/\omega^2}} = 2\frac{k^2}{\omega}\sqrt{\frac{\omega^2}{\omega^2+k^2}} = 2\frac{k^2}{\cancel{\omega}}\cancel{\omega} = 2(1-\omega^2).$$

Instead, maintaining the sinusoidal dependences and using the dispersion relation, from the Eq. (3.21) the maximum amplitude becomes

$$\widetilde{B}_s = \frac{2(1-\omega^2)}{\sqrt{1+\omega^2\cot(\omega t)}}. \tag{3.22}$$

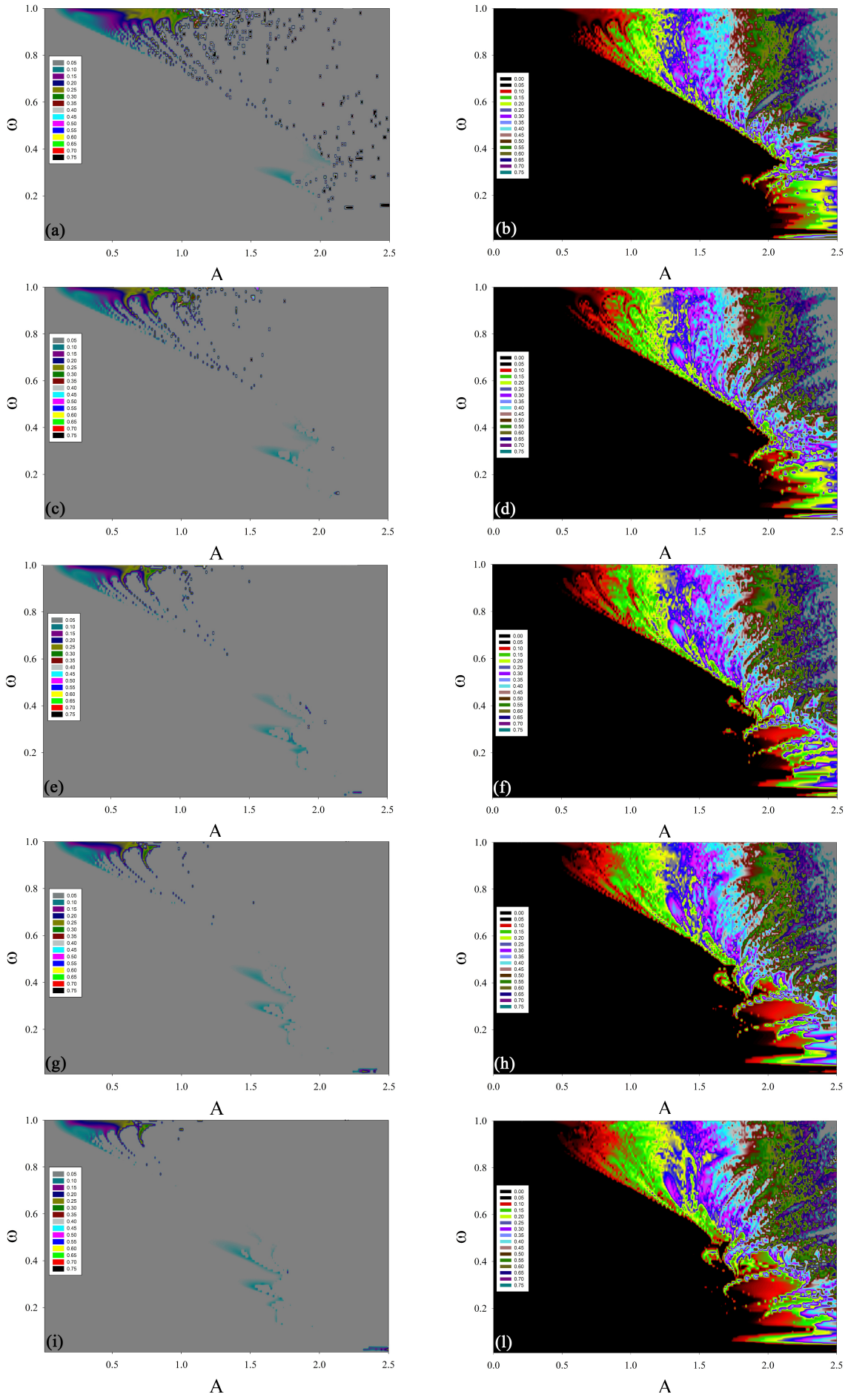

Figure 3.8: Bifurcation diagrams for $\sigma_{\overline{\varphi}}$ (left panels) and injected energies E_i (right panels) as a function of amplitude A and frequency ω of the driving signal, setting $\gamma = 0.02$ and $T_{exp} = 20$ and varying the bias current value i_b. From the top, $i_b = \{0$ (panels a and b), 0.05 (c and d), 0.1 (e and f), 0.15 (g and h), 0.2 (i and l)$\}$.

The Eqs. (3.13) and (3.22), for $t = T_{exp}$, are plotted in Fig. 3.7. Exciting the junction with a signal of limited duration, the energy flows into the medium by breather modes, only for the (A, ω) values for which the curves in Fig. 3.7 touch each other.

The bifurcation diagrams of dispersion and energy-injected presented in Fig. 3.8 are calculated setting $\gamma = 0.02$ and $T_{exp} = 20$ and varying the bias current value i_b. In detail, $i_b = \{0$ (panels a and b), 0.05 (c and d), 0.1 (e and f), 0.15 (g and h), 0.2 (i and l)$\}$. Investigations of breathers excited in a biased SG equation was developed by Lomdahl *et al* [173]. A positive (negative) driving force accelerates a kink (antikink) to the right and an antikink (kink) to the left, so that a large driving force, i.e. greater then a threshold value [173], causes the breather to split in a kink-antikink pair. The breathers-branches in the left panels of Fig. 3.8 disappear increasing the bias current, as a sign of the breathers splitting into kink-antikink couples due to the bias current increase.

Bifurcation diagrams for $\sigma_{\overline{\varphi}}$ and injected energies E_i, setting $T_{exp} = 20$, $i_0 = 0$ and varying the damping parameter γ, are shown in the left and right panels of Fig. 3.9, respectively. The damping parameter values are $\gamma = \{0$ (panels a and b), 0.001 (c and d), 0.01 (e and f), 0.02 (g and h), 0.2 (i and l)$\}$.

By increasing the damping up to $\gamma \leq 0.02$, the breathers density on the graph increases. Probably, a high damping parameter value makes easier to realize the energy condition expressed by Eq. (3.18). This is true under the assumption that the breather should be able to propagate for a sufficent time along the medium (the experimental requirement for our purposes is that it reachs the junction edge opposite to the excited one). Indeed, due to its unstable nature, a breather tends to rapidly decay in amplitude and to move more and more slowly. Recently, Johnson and Biswas [174], deeply explored the dynamics of a breather solution of a perturbed SG equation, including in the perturbation many terms, taking into account different physical phenomena in JJs (dissipation, inhomogeneity of local inductance and capacitance, diffusion, losses due to a current along the barrier, high order spatial dispersion). They found the integral of motion and used it in soliton perturbation theory to derive the differential equation $\mathrm{d}v/\mathrm{d}t$ governing the breather velocity. For JJs in which only dissipation is considered, $\mathrm{d}v/\mathrm{d}t$ can be solved exactly in terms of an initial velocity $v(0) = v_0$, obtaining the velocity of a breather $v(t)$ normalized to the initial value

$$\frac{v(t)}{v_0} = \frac{e^{-\gamma t}}{\sqrt{1 + v_0^2(e^{-2\gamma t} - 1)}}, \tag{3.23}$$

where $v(t)$ and v_0 are both normalized to the Swihart velocity. The breather velocity as a function of time t, for $\gamma \in [0.01 - 0.05]$, is plotted in Fig. 3.10a, setting $v_0 = 0.9$. The rapid decay of the breather is evident.

Integrating the Eq. (3.23) the distance covered by a breather in a time t is

$$x(t) = \frac{1}{\gamma}\left[\operatorname{arcsinh}\left(\frac{v_0}{\sqrt{1 - v_0^2}}\right) - \operatorname{arcsinh}\left(\frac{v_0}{\sqrt{1 - v_0^2}} e^{-\gamma t}\right)\right]. \tag{3.24}$$

The time required to reach the position $x(t) = L$ is

$$t_{(x=L)} = -\frac{1}{\gamma} \ln\left[\cosh(\gamma L) - \frac{\sinh(\gamma L)}{v_0}\right] \tag{3.25}$$

and this espression diverge for

$$\cosh(\gamma L) = \frac{\sinh(\gamma L)}{v_0} \qquad \text{that is} \qquad \tanh(\gamma L) = v_0. \tag{3.26}$$

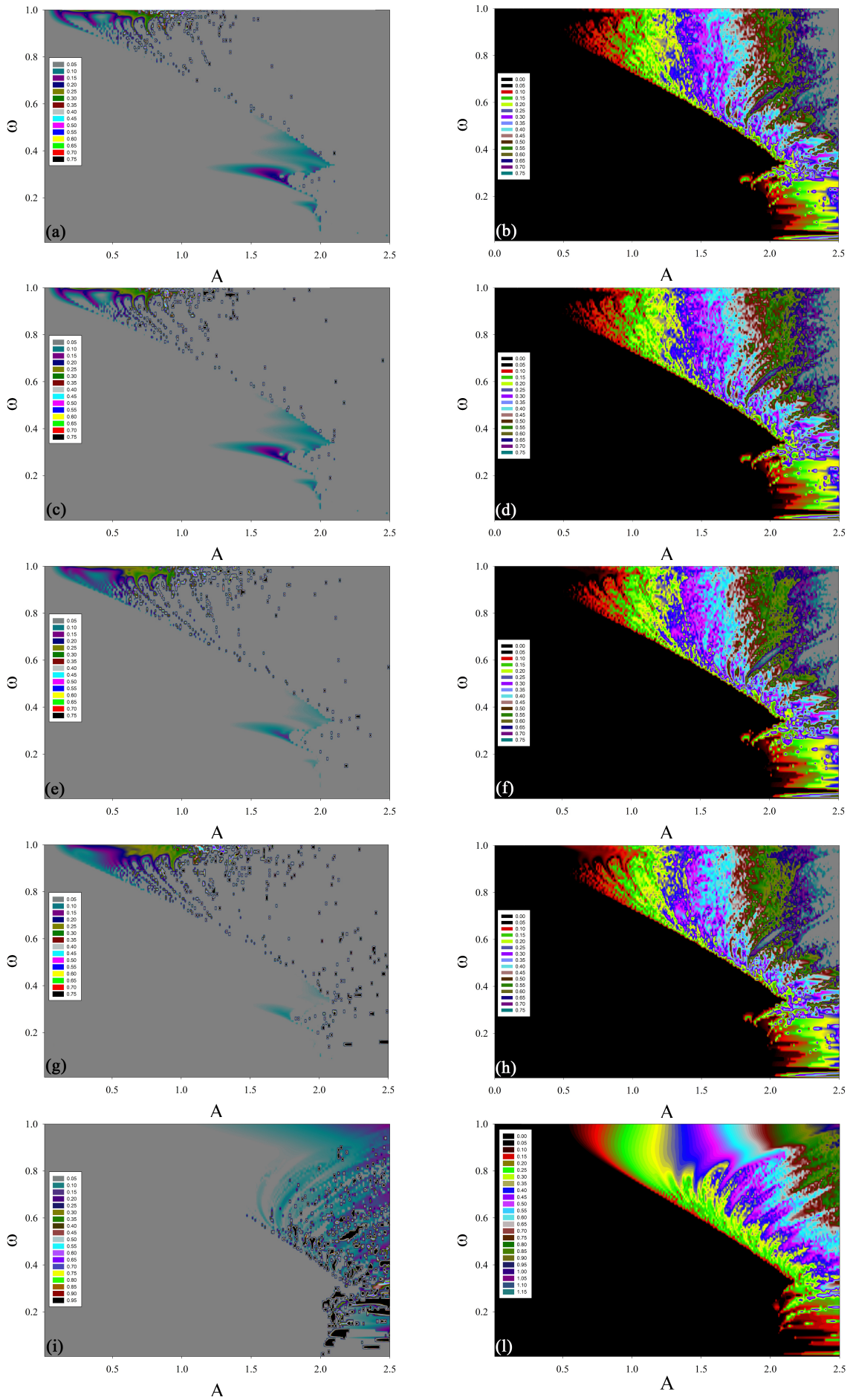

Figure 3.9: Bifurcation diagrams for $\sigma_{\overline{\varphi}}$ (left panels) and injected energies E_i (right panels) as a function of amplitude A and frequency ω of the driving signal, setting $T_{exp} = 20$ and varying the damping parameter γ. From the top, $\gamma = \{0$ (panels a and b), 0.001 (c and d), 0.01 (e and f), 0.02 (g and h), 0.2 (i and l)$\}$.

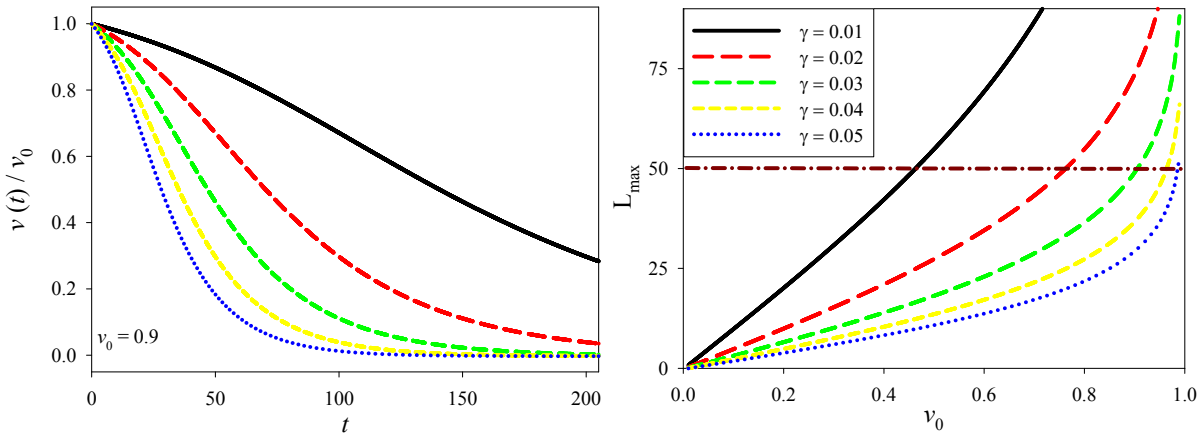

Figure 3.10: a) Breathers speeds, normalized to the intial value v_0, see Eq. (3.23), as a function of the time t, for $\gamma \in [0.01 - 0.05]$ and setting $v_0 = 0.9$. b) Maximum distances covered by a breather, see Eq. (3.27), as a function of the initial speed v_0 for $\gamma \in [0.01 - 0.05]$. The legend in panel b refers to both graphs.

The maximum distance covered by a breather in a time $t \to \infty$ is

$$\mathrm{L}_{max} = \frac{\mathrm{arctgh}\,(v_0)}{\gamma}. \tag{3.27}$$

The maximum distance L_{max} as a function of the initial speed v_0 for $\gamma \in [0.01 - 0.05]$ is plotted in Fig. 3.10b. This picture shows that, depending to the initial speed and to the damping value, breathers can never reach the right junction edge (a dash-dotted line is placed in correspondence of $\mathrm{L}_{max} = 50$ to mark the value setted in the analysis).

The panel (i) of Fig. 3.9 shows only plasma waves and very slow solitons. Indeed, in absence of applied bias current, this value of damping is sufficient to slow the soliton up to stop it.

To check the robustness of the generated breathers, a nonzero noise amplitude is considered. The stochastic investigation is developed performing $N = 10^3$ numerical realizations, setting the (A, ω) parameters corrisponding to the deterministic creation of breathers. In the SG model, see Eq. (3.15), a white noise contribute i_{TN}, with the well-known statistical properties

$$\left\langle i_{TN}\left(\tilde{t}\right)\right\rangle = 0 \qquad \left\langle i_{TN}\left(\tilde{t}\right) i_{TN}\left(\tilde{t}+\tilde{\tau}\right)\right\rangle = 2\frac{kT}{R_N}\delta\left(\tilde{\tau}\right). \tag{3.28}$$

is included.

Thermal fluctuations can provide the system with an amount of energy large enough to create a kink-antikink couple instead of a breather, or to break a breather into a kink-antikink couple. The percentages of surviving breathers, after N numerical realizations, as a function of the amplitude A (varying in the range $A \in [0.4 - 1.5]$) and of the frequency ω (varying in the range $\omega \in [0.55 - 0.85]$), are shown in Fig. 3.11. The noise amplitudes are $\gamma_{TN} = 10^{-4}$ (panel a) and $\gamma_{TN} = 10^{-3}$ (panel b). For large A values, little amount of thermal energy can be enough to destroy a breather, i.e. for $A \gtrsim 1$, breathers can be detected with a probabilty less then $\sim 20\%$. Anyway, suitable (A, ω) values ranges exist in which breathers are still generated by external excitation with

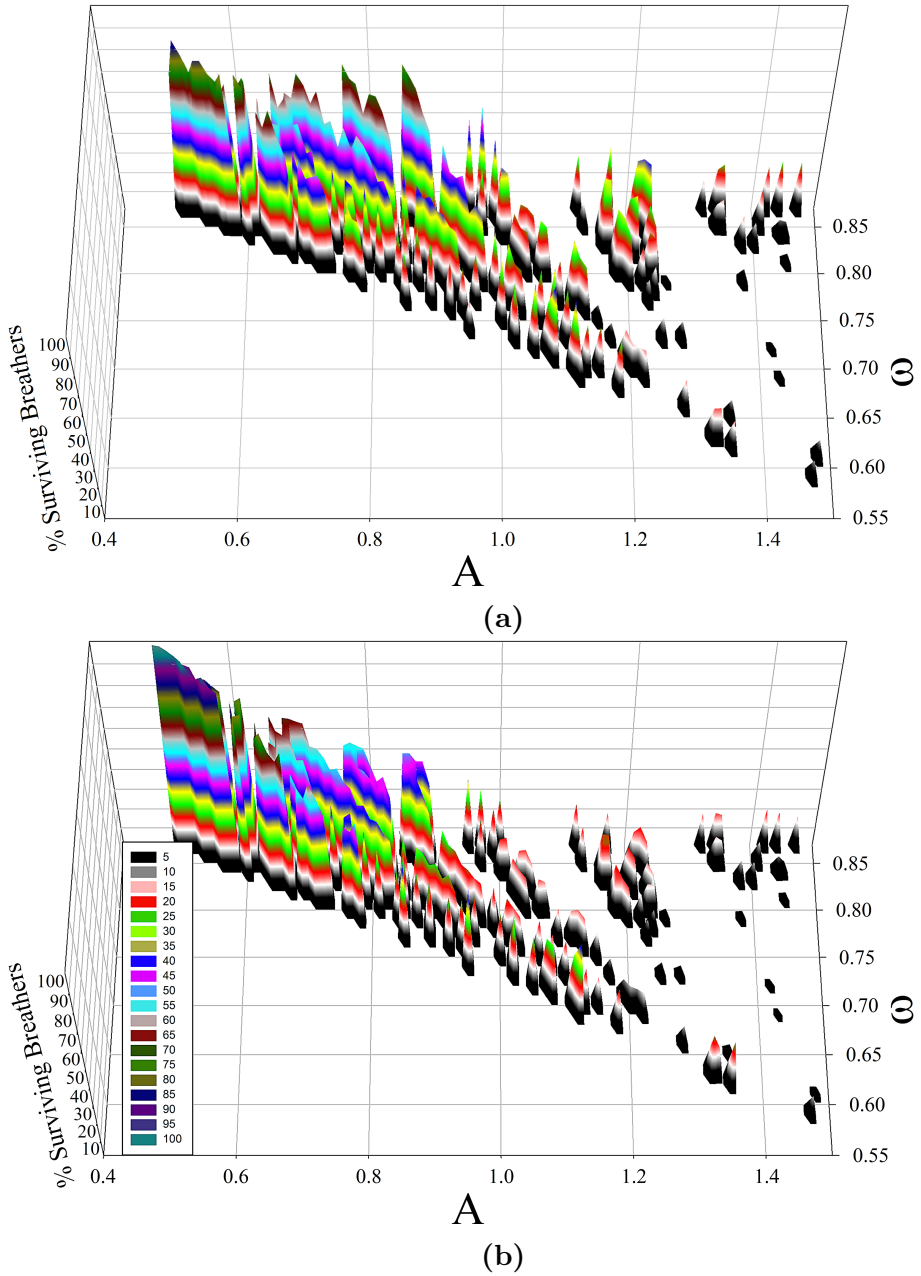

Figure 3.11: Percentage of surviving breathers as a function of amplitude A and frequency ω of the external drive, setting $\gamma_{TN} = 10^{-4}$ (panel a) and $\gamma_{TN} = 10^{-3}$ (panel b), and performing $N = 10^3$ numerical realizations. The legend in panel b refers to both pictures.

high probabilities, despite of the thermal influence.

3.4 Conclusions

I explore the breathers generation and propagation in a long Josephson junction externally irradiated by a suitable excitation, changing the amplitude A and the frequency ω of the exciting external signal. The analysis is computationally developed in the framework of the damped and biased continuous sine-Gordon equation, using a sinusoidal pulse with amplitude $A(t)$ smoothly increasing/reducing, according to Gaussian profiles, during the switching on/off regimes of the pulse. To include the environmental influence, a Gaussian white noise source is inserted into the model. Taking a cue from the results

of Ref. [12] on the nonlinear supratransmission (NST) in a discrete sine-Gordon chain, I obtained two kinds of *bifurcation diagrams*, plotting the dispersion of the phase values of a reference cell, and the energy injected into the system as a function of A and ω. These pictures clearly shows a parameters region in which no energy flows into the medium (that is without NST) and a region in which energy travels through the junction by means of SG nonlinear excitations, i.e. kinks, antikinks, breathers and plasma waves. When NST occurs, I highlighted a new peculiar localization of the breathers in *branches*, in which soliton modes are not excited. The density of these breathers-branches on a (A, ω) parametric space is strongly dependent on the duration of the pulse, the applied bias current and the damping of the system. Increasing the pulse duration more energy is pumped into the system and the energetic conditions, giving an excited breather, are hardly satisfied. Therefore, breather-branches tend to disappear increasing the pulse duration. Similarly, increasing the applied bias current the breather-branches tend to vanish because the current stretches a breather up to split it into a kink-antikink couple. The damping parameter has also to be carefully set, because an appropriate value favors the breathers formation but a too high damping value rapidly annihilates a generated breather. The deterministic analysis is improved including a white noise contribute, to evaluate the percentage of breathers resisting to the thermal effects. Combination of (A, ω) exists in corresponce of which breathers are induced with high probability, despite the noise influence.

Chapter 4

Short graphene-based JJ

I study by numerical methods the phase dynamics in ballistic graphene-based short Josephson junctions. A superconductor-graphene-superconductor system exhibits superconductive quantum metastable states similar to those present in normal current-biased JJs. I explore the effects of thermal and correlated fluctuations on the escape time from these metastable states, when the system is stimulated by an oscillating bias current in the presence of Gaussian white and coloured noise sources. Varying the intensity and the correlation time of the noise source, it is possible to analyze the behavior of the escape time from a superconductive metastable state in different temperature regimes. Moreover, dynamical regimes characterized by the *dynamic resonant activation* effect, in the absence of noise source, and the *stochastic resonant activation* phenomenon, induced by the noise, can be distinguished. *Noise enhanced stability* is also observed in the system investigated. For low initial values of the bias current, the dynamics resonant activation shows new double-minimum structures.

4.1 Graphene and Josephson junctions

The possibility of obtaining *graphene* [175], by extraction of single layers from graphite, paved the way for a new generation of superconductive graphene-based devices. In particular, the evidence of proximity-induced superconductivity [17, 18], due to the one-atom thick nature of graphene, promoted the realization of superconductor-graphene-superconductor (SGS) structures. The refractoriness of graphene to the surface oxidation in natural environment favours the realization of highly transparent contacts with the superconductive electrodes. Furthermore, superconductivity in graphene, pure or doped, was predicted and explored [176, 177] and new devices, as dc-SQUIDs [178, 179], proximity Josephson sensors [180], or bolometers based on superconductive tunnel junction contacts [181], were fabricated using graphene. The charge carriers in graphene are massless quasiparticle, the Dirac fermions, with pseudo-spin half and linear energy dispersion [182]. The band structure shows contact points, called Dirac points, beetwen the conduction and valence bands [182]. These peculiar electronic properties [182] give rise to interesting phenomena, such as specular Andreev reflection [183], unusual propagating modes along graphene channels [184], oscillatory dependence of the Josephson current on the barrier thickness and applied bias voltage [185]. Titov and Beenakker [186] predicted, in the limit of zero temperature, the behavior of critical current and current-phase relationship (CΦR) for a short *ballistic* SGS system. Taking a cue from these results, Lambert *et al.* [187] derived the expression of the washboard potential for a suspended graphene junction.

Different aspects of graphene-based junctions in noisy environment were already examined by several authors. Miao *et al.* [20] took into account the noise induced prema-

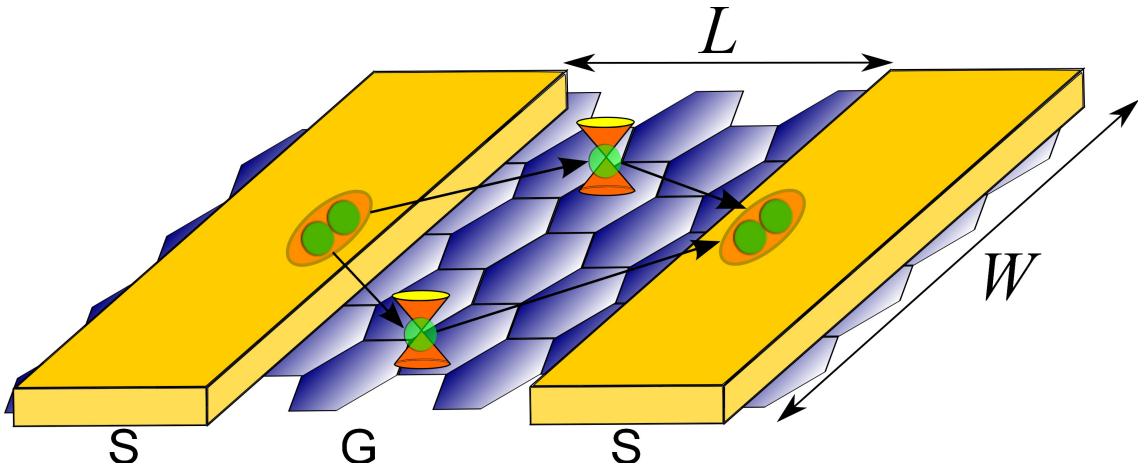

Figure 4.1: Schematic view of a suspended SGS device. The electrons forming a Cooper pair, when they enter graphene, move into different K-valleys, represented as orange cones. In the short-junction regime, $L \ll W$.

ture switching in underdamped SGS JJ at finite temperature. Specifically, in Ref. [20] the reduction of the critical current and variations in the product $I_C R_N$ were experimentally observed and theoretically explained considering non-negligible the thermal fluctuations. Other authors [17, 188] suggested a supercurrent reduction by premature switching induced by thermal and electromagnetic noise. Coskun *et al.* [16] systematically studied the thermally activated dynamics of phase slip in SGS JJs throught the measurement of the switching current distribution. They found an anomalous temperature dependence of the switching current dispersion due to nontrivial structure [186, 189] of the Josephson current. A simple stochastic model to explore the electrodynamics of an underdamped graphene JJ was proposed by Mizuno *et al.* [15]. They stressed the importance of realizing high quality suspended SGS structures, to prevent disorders due to the conventionally used substrates, whereby a flow of supercurrent at high critical temperature can be obtained. The SGS junction is a good candidate for the fabrication of gate-tunable phase qubits [190, 191]. In Ref. [190] the study of the stochastic switching current distribution in a SGS junction for low temperatures allowed to highlight the macroscopic quantum tunneling and energy level quantization, similarly to conventional JJs. Moreover, Lee *et al.* [190] studied the switching current distribution in both quantum and thermal regime, building up a computational analysis based on the pure resistively and capacitively shunted junction (RCSJ) model for a conventional JJ [62], that is a SNS or a SIS junction. Considering a range of temperatures in which the dynamics is exclusively ruled by thermal fluctuations, Lee *et al.* [190] observed disagreement between the experimental and fitted temperatures. To understand this discrepancy, they invoked the misuse, in their model, of the pure sinusoidal Josephson current distribution, neglecting however any noise induced effects on the escape rate from the superconductive state.

My work fits well into this scenario, since it aims to study how thermal fluctuations affect the dynamical behavior of a SGS junction. In particular, I study the influence of Gaussian (white or colored) noise sources on the switching dynamics from the superconductive metastable state to the resistive one in a suspended graphene-based short JJ, considering the proper CΦR [186]. In this chapter I explore therefore the transient dynamics of an underdamped SGS junction, considering the simultaneous action of an external driving force oscillating with frequency ω, and a stochastic signal which represents a random force of intensity γ. I focus our analysis on the mean permanence time in the superconductive state. The study is performed fixing the initial values of the applied bias current i_0 and the correlation time τ_c of the colored noise source, and varying

the frequency ω and the noise intensity γ. Whenever possible, results are compared with those obtained for normal JJs. The similarities in the behavior of the graphene-based and normal junctions allow to interprete our results referring to conventional JJ quantities, such as plasma frequency (Eq. (4.4)).

The chapter is organized as follows. The next section includes an overview about the physical model used. In Sec. III the theoretical results are shown and analyzed. The Sec. IV contains a *probability density function* (PDF) analysis of the escape times, by focusing on the appearance of noise induced non-monotonic effects in the mean switching times. In Sec. V conclusions are drawn.

4.2 The Model

The dynamics of a JJ can be explored looking at the time evolution of the order parameter φ. According to the RCSJ model and including the environmental influence, the equation of motion for φ is

$$\varphi_{tt}(t) + \beta_{_J}\varphi_t(t) = i_b(t) - i_\varphi(t) + i_f(t) \tag{4.1}$$

where $i_b(t)$ and $i_\varphi(t)$ are the bias and supercurrent respectively, both normalized to the critical current of the junction I_c. The term $i_f(t)$ represents the stochastic noise contribution. The subscripts of φ denote partial derivatives in time. The use of normalized variables allows to extend, in a direct and simple way, the theoretical results to different experimental settings. Eq. (4.1) is in accordance with the Johnson approach [62], since it includes a damping parameter $\beta_{_J} = (\omega_{p_0} R_N C)^{-1}$, multiplied by $\varphi_t(t)$, and assumes the time variable normalized to the inverse of the zero-bias plasma frequency $\omega_{p_0} = \sqrt{2\pi I_c/(\Phi_0 C)}$ (R_N and C are the normal resistance and capacitance of the junction, and $\Phi_0 = h/2e$ is the magnetic flux quantum). Introducing the parameter $\beta_{_C} = {\beta_{_J}}^{-2}$, Eq. (4.1) can be alternatively arranged in the Stewart-McCumber framework [62], according which a term $\beta_{_C}\varphi_{tt}(t)$ is included in the equation, and the time variable is normalized to the inverse of the JJ characteristic frequency $\omega_c = \omega_{p_0}^2 R_N C$. The JJ behavior can be depicted as the motion of a "phase particle" with mass $m = C(\Phi_0/2\pi)^2$ rolling down along *washboard potential*. For a conventional current biased junction, the normalized supercurrent and washboard potential have the well-known expressions

$$i_\varphi(t) \;=\; \sin(\varphi(t)) \tag{4.2}$$

$$U(\varphi, t) \;=\; -E_{J0}\left[\cos(\varphi(t)) + i_b(t)\,\varphi(t)\right], \tag{4.3}$$

where $E_{J0} = \Phi_0 I_c/2\pi$ is the Josephson coupling energy, that is the energy initially stored in the junction. The bias current represents the slope of this potential. Eq. (4.2) is the *d.c. Josephson relation*. In the limit of small amplitude oscillations, the JJ plasma frequency corresponds to the oscillation frequency in the bottom of a potential well, modified by the presence of a bias current according to

$$\omega_{_P}(t) = \omega_{p_0}\sqrt[4]{1 - i_b^2(t)}. \tag{4.4}$$

Titov and Beenakker [186] calculated the CΦR and critical current for a ballistic graphene-based junction at the Dirac point. They addressed the problem in the framework of the Dirac-Bogoliubov-de Gennes (DBdG) equation [183, 192]. Considering the

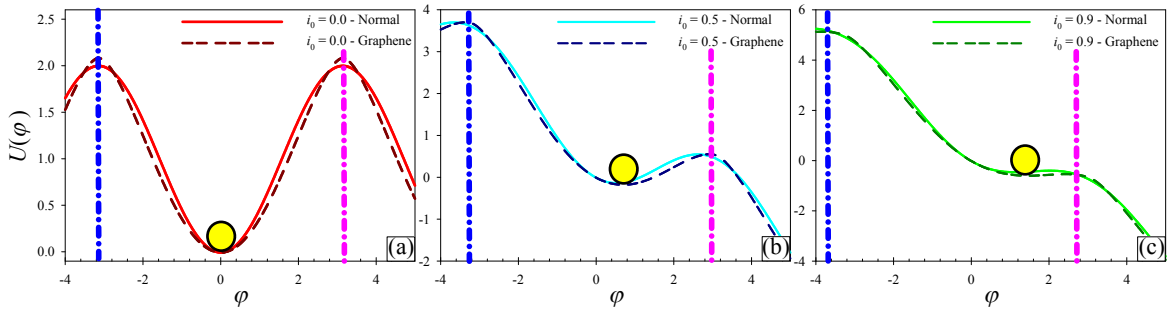

Figure 4.2: Washboard potential for conventional (see Eq. (4.3)) and graphene (see Eq. (4.9)) JJs (solid and dashed lines, respectively), for different initial values of the bias current: a $i_0 = 0.0$; b $i_0 = 0.5$; c $i_0 = 0.9$. It is also shown the initial position (bottom of the potential well) of the "phase particle". Blue and pink dotted-dashed lines indicate the left and right absorbing barriers, respectively.

Josephson current at zero temperature [193]

$$I(\varphi) = -\frac{4e}{\hbar}\frac{\mathrm{d}}{\mathrm{d}\varphi}\int_0^\infty d\varepsilon \sum_{n=0}^{\infty} \rho_n(\varepsilon,\varphi)\varepsilon, \tag{4.5}$$

supposing an "ideal" normal-metal-superconductor interface and taking infinite mass boundary conditions [194] they obtained the following expressions

$$i_\varphi(t) = \frac{I(\varphi)}{I_c} = \frac{2}{1.33}\cos\left(\frac{\varphi}{2}\right)\tanh^{-1}\left[\sin\left(\frac{\varphi}{2}\right)\right] \tag{4.6}$$

$$I_c = 1.33\frac{e\Delta_0}{\hbar}\frac{W}{\pi L}, \tag{4.7}$$

where W and L are the linear dimensions of the device (see Fig. 4.1), that is the length of the superconductive plates and their separation, respectively. Furthermore Δ_0 is the superconductive excitation gap, e the electron charge and $\hbar$ the reduced Plank's constant. Eqs. (4.6) and (4.7) refer to the *short-junction* regime, in which L is smaller than the superconducting coherence length ξ (the distance at which a Cooper pair spreads), and to junctions with short and wide normal region, i.e. $L \ll W$. I recall that the simple CΦR given in Eq. (4.6) is obtained in the limit of zero temperature. Hagimásy *et al.* [189] calculated a more general formula for finite temperature T and arbitrary junction length (for more details about $I(\varphi, T)$ see Appendix C). However, an analytic expression for the Josephson current, such as that given in terms of washboard potential, can not be obtained except for $T = 0$. Indeed, for vanishing temperature the expression by Hagimásy *et al.* correctly converges to that obtained by Titov and Beenakker. Instead, for $T \to T_c$, the non-sinusoidal supercurrent derived by Hagimásy *et al.* in both long and short junction regime, converges to a sinusoidal behavior. In the short junction limit, cf. Fig. 1a and Fig. 3a in Ref. [189], as long as $T \lesssim T_c/4$, the critical current and $i(\varphi)$ hardly change, so that Titov and Beenakker's formula remains valid [195]. This temperature threshold can be also deduced from the gap equation of the BCS theory, cf. Eq. C.13 in Appendix C. Thi analysis is therefore strictly valid in a wide range of temperature values, and represents a good approximation for temperatures far from the critical value. For completeness, in the long junction limit ($L \gg W$), the Josephson current reduces to

$$I(\varphi) = \frac{e\Delta}{\hbar}\tanh\left(\frac{\Delta}{2T}\right)e^{-\pi L/W}\sin\varphi = I_c(T)\sin\varphi, \tag{4.8}$$

showing the same φ-dependence of conventional JJs (see Appendix C).

Lambert *et al.* [187] obtained from the expression of the current Eq. (4.6), for a SGS, the following washboard-like potential

$$\widetilde{U}(\varphi,t) = - E_{J0}\left\{ - \frac{2}{1.33}\left\{ 2\sin\left(\frac{\varphi(t)}{2}\right)\tanh^{-1}\left[\sin\left(\frac{\varphi(t)}{2}\right)\right] + \right.\right. \\ \left.\left. + \ln\left[1-\sin^2\left(\frac{\varphi(t)}{2}\right)\right]\right\} + i_b(t)\varphi(t)\right\}. \tag{4.9}$$

The analytic knowledge of the potential allows to well impose the initial condition and the thresholds for the escape time calculations. As well as the conventional $U(\varphi,t)$ (see Eq. (4.3)), the potential $\widetilde{U}(\varphi,t)$ consists of a tilted sequence of wells. In the *superconductive state* the particle lies in a well, while in the *resistive state* it rolls down along the potential. When this happens, a non-zero mean voltage V across the junction appears, according to the *a.c. Josephson relation*, see Eq. 1.5. Furthermore, depending on the damping parameter value, the *phase diffusion state*, that is an escape event with a retrapping in the first subsequent minimum, could be established. When $i_b(t) \geq 1$, that is when the applied bias current exceeds the critical value, both potentials (Eqs. (4.3) and (4.9)) lose their "maxima and minima" structures and the particle tends to freely slip.

I explore the response of the system to the simultaneous action of both d.c. and a.c. current sources. The bias current, composed by a constant term, i_0, representing its initial value, and an oscillating part whose frequency ω is normalized to ω_{p_0}, is therefore given by

$$i_b(t) = i_0 + A\sin(\omega t). \tag{4.10}$$

with maximum and minimum values given by

$$i_b^{\pm} = i_0 \pm A, \tag{4.11}$$

respectively.

By choosing properly the values of i_0 and A, within a period it is possible to achieve values of $i_b(t)$ greater than 1. A direct comparison between the potentials for normal and graphene-based JJ is given in Fig. 4.2 for $i_0 = 0.0$ (panel a), 0.5 (panel b), 0.9 (panel c). Here it is worth noting that differences, though small, between the graphene and normal JJ curves are detectable. Fig. 4.2 shows also the initial condition for the fictitious particle, which is located in the potential minimum. The system leaves the superconductive regime when the particle reaches one of the nearest maxima. Two absorbing barriers are therefore placed in correspondence to these maxima, as highlighted in Fig. 4.2 (see dotted-dashed lines). Recording for each realization the escape times t^{esc}, i.e. the time required to pass a barrier, for an enough large number N of realizations, the *mean first passage time* (MFPT) is defined as

$$\tau = \frac{1}{N}\sum_{i=1}^{N} t_i^{esc}. \tag{4.12}$$

The oscillating force acting on the system, $i_b(t)$, and stochastic fluctuations, $i_f(t)$, due to the environmental influence, drive the switching dynamics. Two different mechanisms can therefore cause overcome of the potential barrier: the macroscopic quantum tunneling or the thermally activated passage. These processes are triggered in distinct ranges of temperature so that, for vanishing values of the bias and damping, a threshold value

		Mizuno [15]	Coskun [16]	Du [17]	Heerschee [18]	English [19] Samples A/B/C/D	Miao [20]
i_C	mA	100	10	800	10	71/107/39/160	110
β_C		76	16				
C	pF	1	12-50				
R_N	Ω	500	10				
T	K	3	0.4	0.2	0.3	0.01	0.3
T_{CO}	K	0.02	$[8\text{-}17]\cdot10^{-3}$				0.12-1.2
γ_C		1.3	1.7	0.01	1.3	$6/4/11/3\cdot10^{-3}$	0.11
ω_{P0}	GHz	17	0.8-1.6				10^2-10^3

Table 4.1: Experimental values of different JJ parameters, calculated or directly acquired by various published works [15–20].

exists, $T_{CO} = \hbar\omega_{p_0}/2\pi k$ (k is the Boltzmann constant), called *crossover temperature*. In a damped system, when a polarization current is applied, this value is slightly reduced, becoming [40]

$$T^{\star}_{CO} = \hbar\omega_R/2\pi k, \tag{4.13}$$

where $\omega_R = \omega_P\left\{\sqrt{1+\alpha^2}-\alpha\right\}$, $\alpha = (2\omega_P R_N C)^{-1} \propto \beta_J$. For $T < T^{\star}_{CO}$ the system undergoes a *quantum tunneling regime*. On the other hand, for $T > T^{\star}_{CO}$, the system works in the *thermal activation regime*.

Here quantum effects are not taken into account. In this condition, when thermal fluctuations are neglected, the phase can remarkably change merely as the applied current approaches the critical value I_c (the system moves into a resistive regime). Conversely, considering noise effects, transitions along the potential can occur also applying a current much smaller than I_c. As already pointed out, the phase dynamics is affected by dissipative phenomena, responsible for peculiarities of the system, ranging from overdamped (high viscosity $\beta_J \gg 1$) to underdamped (low viscosity $\beta_J \ll 1$) condition. Table 4.1 shows a collection of few experimental values, for different graphene-based JJs, calculated or, whenever possible, directly acquired by different published works [15–20]. Blank cells indicate not available values. The values of the parameters $\beta_C = {\beta_J}^{-2}$ suggest that these systems often [15, 16] work in underdamped conditions. Moreover, the comparison between the working temperature T and the crossover value $T^{\star}_{CO}$ underlines the thermally activated switching behavior of these junctions [15, 16, 20].

The noise source. – An exhaustive analysis of a real device has to take into account environmental fluctuations continuously affecting the system, such as unpredictable variations of current and temperature. Thus the deterministic RCSJ model can be improved by considering the presence of the stochastic current $i_f(t)$ (see Eq. (4.1)), in a first approximation modeled using a Gaussian "white" noise source. The stochastic non-normalized current $I_f\left(\tilde{t}\right)$ is therefore characterized by the well-known statistical properties of a Gaussian random process

$$\left\langle I_f\left(\tilde{t}\right)\right\rangle = 0 \qquad \left\langle I_f\left(\tilde{t}\right) I_f\left(\tilde{t}+\tilde{\tau}\right)\right\rangle = 2\frac{kT}{R_N}\delta\left(\tilde{\tau}\right), \tag{4.14}$$

where T is the temperature. Using normalized current and time, the correlation function becomes

$$\langle i_f(t) i_f(t+\tau)\rangle = 2\gamma(T)\delta\left(\tau\right), \tag{4.15}$$

where the dimensionless amplitude $\gamma(T)$ is proportional to the temperature T. The expression of $\gamma(T)$ depends on the approach used to manage Eq. (4.1)

$$\text{McCumber)} \quad \gamma^c(T) = \frac{kT}{R_N}\frac{\omega_c}{I_c^2} = \frac{2e}{\hbar}\frac{kT}{I_c} = \frac{kT}{E_J} \tag{4.16a}$$

$$\text{Johnson)} \quad \gamma^p(T) = \frac{\omega_{p0}}{\omega_c}\gamma^c(T) \tag{4.16b}$$

It is worth noting that the noise intensity can be also expressed as the ratio between the thermal and Josephson coupling energies (see Eq. (4.16a)). Few γ^c values, calculated for several experimental settings, are shown in Table 4.1. More in general, $i_f(t)$ can represent a Gaussian colored noise, modeled as an exponentially correlated noise source. Specifically, in this work the noise source is described by the well-known Ornstein-Uhlenbeck (OU) process [196]

$$di_f(t) = -\frac{1}{\tau_c}i_f(t)dt + \frac{\sqrt{\gamma}}{\tau_c}dW(t), \tag{4.17}$$

where γ and τ_c are the intensity and correlation time of the noise source, respectively, and $W(t)$ is the Wiener process, characterized by the well-known statistical properties: $\langle dW(t)\rangle = 0$ and $\langle dW(t)dW(t')\rangle = \delta\,(t-t')\,dt$.

The correlation function of the OU process is

$$\langle i_f(t)i_f(t')\rangle = \frac{\gamma}{2\tau_c}e^{-\frac{|t-t'|}{\tau_c}}, \tag{4.18}$$

and gives $\gamma\,\delta(t-t')$ in the limit $\tau_c \to 0$.

Computational details. – The stochastic dynamics of the system is explored integrating Eqs. (4.1) and (4.17) by a finite difference method. Specifically, the stochastic differential equation (4.17) is integrated within the Ito scheme. The time step is fixed at $\Delta t = 10^{-3}$ and the maximum time, for which equations are integrated, is $t_{max} = 100$, i.e. a time large enough to catch every nonmonotonic behavior. A collection of first passage times is obtained iterating the procedure for a sufficiently large number of realizations $N = 10^4$. The initial condition to solve Eq. (4.1) is set at the bottom of a valley of the potential given in Eq. (4.9), closer to $\varphi = 0$. During the oscillation of the potential the two absorbing barriers change their position, following the displacements of the maxima closer to the initial valley. The analysis is performed in the underdamped regime, setting $\beta_J = 0.1$ (corresponding to $\beta_C = 100$). Four different values of i_0, in the range $0 \leq i_0 < 1$, are used. The time periodical component of $i_b(t)$, oscillates with values of the frequency ω ranging within the interval $[0.01 - 10]$. In our analysis the intensity γ of the colored noise source $i_f(t)$ varies in the range $[10^{-4} - 10^2]$, with the correlation time, τ_c, set at different values.

4.3 The Analysis

The analysis is performed studying the behavior of the MFPT, τ, as a function of the noise intensity γ and frequency ω of the oscillating term in the bias current. In Eq. (4.10) $i_0 = 0.0, 0.1, 0.5, 0.9$, corresponding to vanishing, small, intermediate and high values, respectively, of the initial slope of the washboard potential. The slope of the potential, that is the value of $i_b(t)$, is directly related to the height of the potential barriers, so that, increasing the value of $i_b(t)$, the right barrier's height decreases, getting zero when $i_b(t) \geq 1$. The normalized amplitude of the oscillating term of the bias current is set at

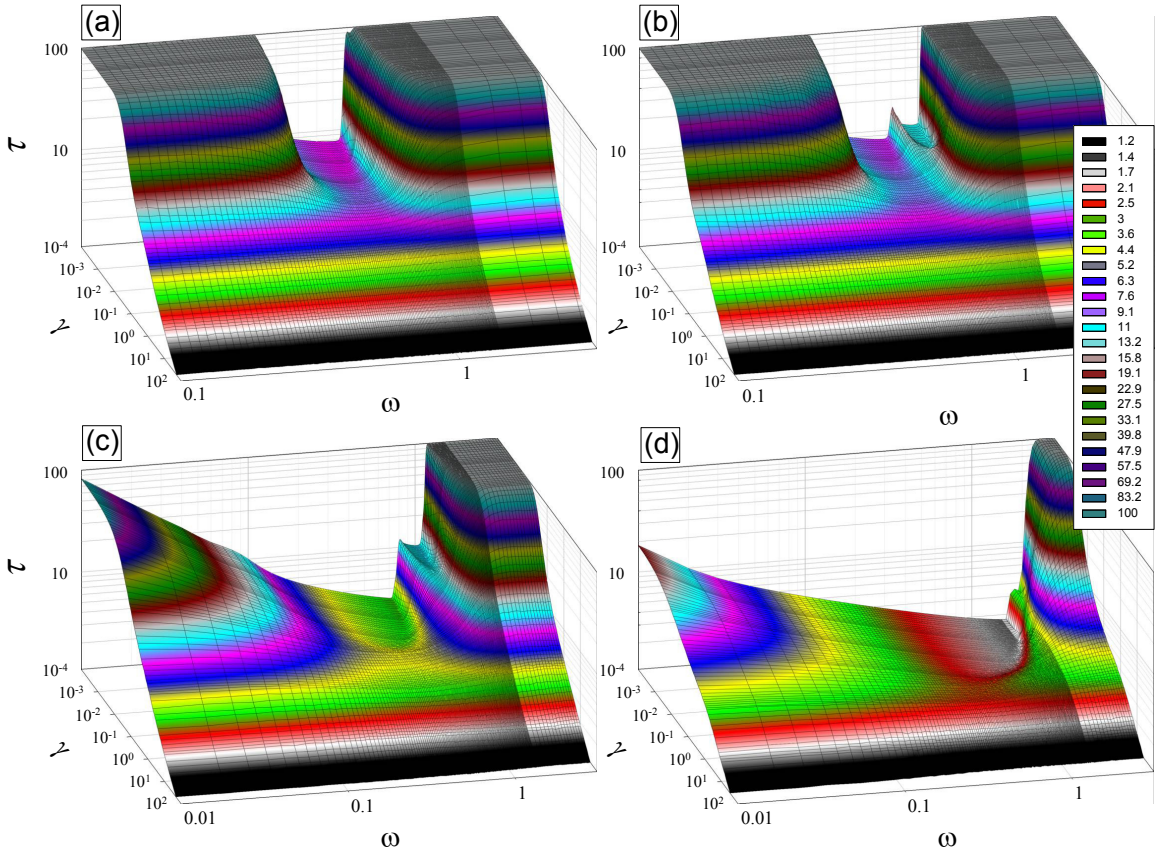

Figure 4.3: MFPT as a function of both ω and γ, for $\tau_c = 0.0$ and different initial values of the bias current: a $i_0 = 0.0$ (no slope); b $i_0 = 0.1$ (small slope); c $i_0 = 0.5$ (intermediate slope); d $i_0 = 0.9$ (high slope). The legend in panel d refers to all pictures.

$A = 0.7$ in all numerical realizations.

The values of τ are shown in three-dimensional plots to highlight the simultaneous presence of different nonmonotonic effects. The values of γ are proportional, through Eqs. (4.16), to the temperature of the system, so that varying the noise intensity in the interval $\gamma = [10^{-4} - 10^{2}]$ corresponds to explore a wide range of temperatures. The noise amplitude values, calculated in different contexts and presented in the Table 4.1, fall within this range. The values of the frequency ω are chosen in such a way to investigate different regimes of alternate current: i) quasi-direct current ($\omega \ll 1$); ii) high-frequency alternate current ($\omega \gg 1$); iii) alternate current oscillating at the characteristic plasma frequency of a conventional junction ($\omega = 1$). Recalling that the driving frequency is normalized to the plasma frequency, the values of ω_{P0} included in Table 4.1 make it possible to give a quantitative estimation of the values taken on by ω. The correlation time of the colored noise source takes the values $\tau_c = 0$ (i.e. white noise), $1, 5, 10$. The results, shown in Fig. 4.3, were obtained using a white noise source, that is setting $\tau_c = 0.0$, and for different values of the initial bias current (slope of the potential), i.e. i_0 = 0.0 (panel a), 0.1 (panel b), 0.5 (panel c), 0.9 (panel d). First I can note that an overall lowering of τ values occurs, as i_0 increases. In other words, changes in the maximum slope of the potential cause modifications in the height of the barriers (see Fig. 4.2). The presence of two absorbing barriers allows to take into account the complete evolution of the phase particle from the initial state. Considering highly tilted potential profile (panel c of Fig. 4.2), the particle rolls down exclusively overcoming the right barrier. Instead, with small value of the initial bias current (panel a of Fig. 4.2), the possibility of escaping over the left-side barrier causes interesting phenomena. In particular, for

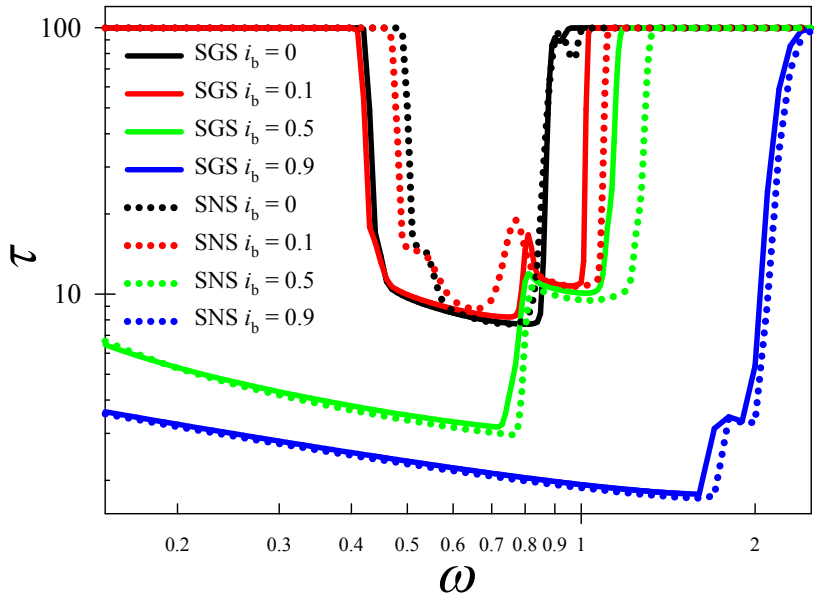

Figure 4.4: MFPT as a function of ω, for $\gamma = 10^{-4}$, $\tau_c = 0.0$, and different initial values of the bias current: $i_0 = 0.0, 0.1, 0.5, 0.9$. Solid and dotted lines represent results for a graphene-based JJ (indicated as GJJ) and a normal JJ (indicated as NJJ), respectively.

$i_0 = 0.0$, the height of the left and right barriers takes on the same values within an oscillation period, so that the particle can escape through the left or right barrier with equal probability. In all panels of Fig. (4.3) it is evident a nonmonotonic behaviour, characterized by a minimum, which indicates the presence of a *resonant activation* (RA) phenomenon [3, 4, 123–130]. This effect is robust enough to be detected in a large range of γ values, even if it tends to be suppressed (the minimum in the curves of MFPT *vs* ω is less pronounced) as the intensity, γ, of thermal fluctuations increases. In particular, two different kinds of RA can be distinguished:

- the *dynamic resonant activation*, which occurs as the external driving frequency is close to the natural characteristic frequency of the system, that is the plasma frequency of the JJ [71, 72, 131];
- the *stochastic resonant activation*, which occurs for driving frequency close to the inverse of the average escape time at the minimum, i.e. the mean escape time over the potential barrier in the lowest configuration [9, 30].

The dynamic RA is evident only in the absence of noise source ($\gamma = 0$) and in quasi-deterministic regime ($\gamma \ll 1$), when the dynamics depends mainly by the profile of the washboard potential of the system. Increasing the noise intensity, the stochastic RA tends to overcome every dynamic RA effect. Fig. 4.4 shows the behaviour of the MFPT *vs* ω, with the noise intensity fixed at such a value ($\gamma = 10^{-4}$) that the dynamic RA effect can be clearly observed and studied as a function of the initial bias current i_0. More in detail, Fig. 4.4 displays results obtained for graphene-based (solid lines) and normal (dotted lines) JJs for $\gamma = 10^{-4}$. The MFPT values in correspondence of the RA minima are almost junction-type independent, even if the RA valleys for normal JJ are shifted towards higher frequencies. In particular, the dynamic RA minima for small i_0 become narrower passing from SGS to SNS junction. In Fig. 4.4, for $i_0 = 0.0$ a single-minimum dynamic RA is present in $\omega_{dRA}^{0.0} \simeq 0.81$. The RA effect becomes more structured, slightly increasing the initial bias current. Indeed, for $i_0 = 0.1$ the same effect occurs with the

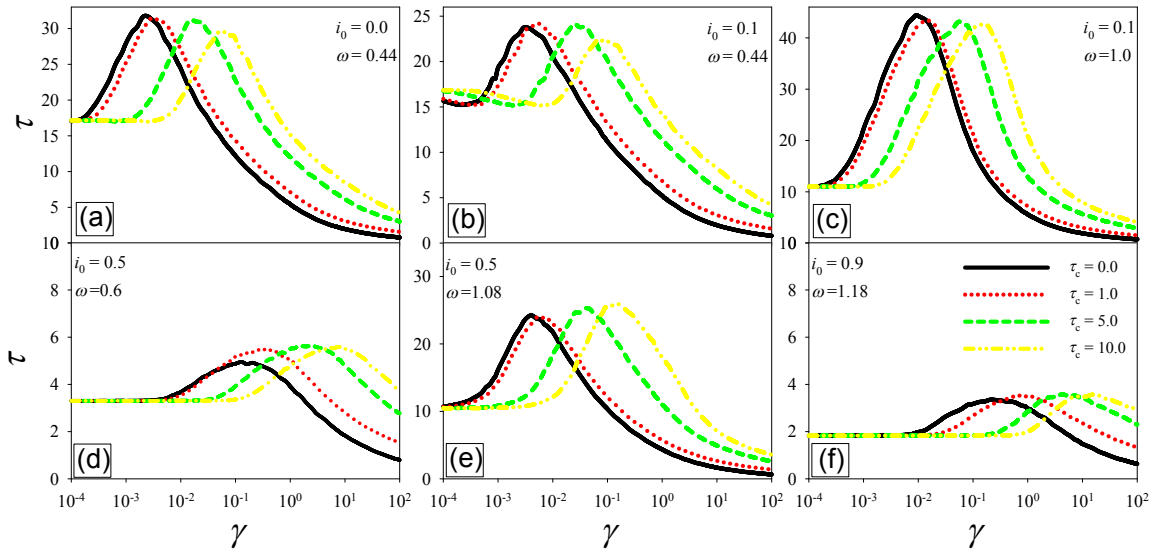

Figure 4.5: MFPT as a function of γ, for different values of ω, i_0 and τ_c. In detail: a $i_0 = 0$, $\omega = 0.44$; b $i_0 = 0.1$, $\omega = 0.44$; c $i_0 = 0.1$, $\omega = 1.0$; d $i_0 = 0.5$ and $\omega = 0.6$; e $i_0 = 0.5$, $\omega = 1.08$; f $i_0 = 0.9$, $\omega = 1.18$. The legend in panel d refers to all pictures.

presence of two minima located at $\omega_{dRA}^{0.1} \simeq 0.75, 0.95$ (see Fig. 4.4). These minima are connected with two resonance phenomena occurring in the system. Specifically, the oscillating potential can "tune" with the plasma oscillations for two different values of ω, one corresponding to escape events towards left, which occur at the lowest slope, $i(t) = i^-$, the other one corresponding to escape events towards right, which occur at the highest slope, $i(t) = i^+$. This double-resonance effect can be further explained, noting that non-vanishing values of the initial bias current ($i_0 \neq 0$) introduce an asymmetry, e.g. with $i_0 = 0.1$ the highest and lowest slope are respectively $\left|i_b^+\right| = 0.8$ and $\left|i_b^-\right| = 0.6$. For these configurations the plasma frequencies, calculated according to Eq. (4.4), are $\omega_P^{0.1}(i_b^+) \simeq 0.77$ and $\omega_P^{0.1}(i_b^-) \simeq 0.90$. These values, even if they do not coincide, are very close to the frequencies $\omega_{dRA}^{0.1}$ for which the RA minima are observed. The small discrepancies between $\omega_{dRA}^{0.1}$ and the two frequencies $\omega_P^{0.1}(i_b^+)$ and $\omega_P^{0.1}(i_b^-)$ can be related to the fact that the conventional JJ plasma frequency was used. Due to the symmetry of the potential for $i_0 = 0.0$ respect to the horizontal position, the minima observed for $i_0 = 0.1$ seem to merge in the larger minimum located, for vanishing bias current, at $\omega_{dRA}^{0.0} \simeq 0.81$ (see Fig. 4.4). Indeed in this situation, the highest and lowest slope have the same absolute value, $\left|i_b^+\right| = \left|i_b^-\right| = 0.7$. Accordingly, in these configurations the plasma frequencies take on values $\omega_P^{0.0}(i_b^+) = \omega_P^{0.0}(i_b^-) \simeq 0.85$, very close to that for which the RA minimum is observed.

The suppression of the dynamic RA, as the noise intensity increases, is evident in the curves obtained for $i_0 = 0.1$. In particular, the stochastic RA emerges at $\gamma_{sRA}^{0.1} \simeq 0.005$, with the minimum located in $\omega_{sRA}^{0.1} \simeq 0.7$. Using these small values of bias current, a trapping phenomenon occurs for $\omega \geq 1$. These trapping phenomena however disappear for higher values of the noise intensity. For $i_0 = 0.5, 0.9$ the potential is tilted enough to lose the wells structure, in the lowest configuration. If $i_0 = 0.5$ the double-minimum dynamic RA is still present around the frequencies $\omega_{dRA}^{0.5} \simeq 0.72, 1.02$, but the MFPT value in the first RA minimum is smaller than that calculated for $i_0 = 0.1$. This is due to the fact that for $i_0 = 0.5$ the virtual particle, i.e. the phase difference between the wave functions of the two superconductors, is able to leave the potential well in a shorter time, escaping through the right potential barrier. The slope $i_0 = 0.5$ in fact is sufficient to

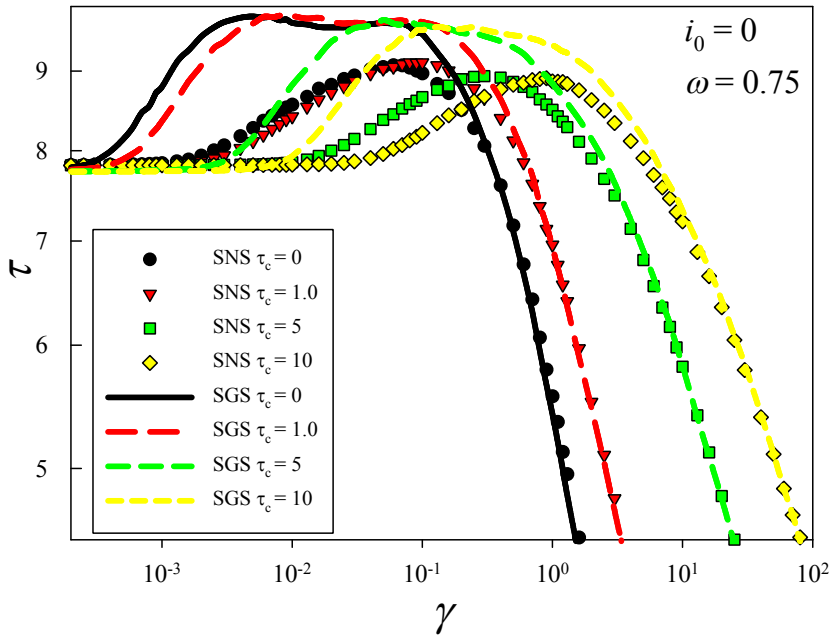

Figure 4.6: MFPT as a function of γ, for $\omega = 0.75$, $i_0 = 0.0$, and different values the noise correlation time: $\tau_c = 0.0, 1.0, 5, 10$. Lines and symbols represent results for a normal JJ (NJJ) and a graphene-based JJ (GJJ), respectively.

produce a right-side escape event already after a quarter of an oscillation period (indeed $\tau \simeq \mathrm{T}_p/4$), whereas for $i_0 = 0.1$ the particle needs one complete oscillation to pass the same barrier. On the other hand, the values of τ in the second RA valley for $i_0 = 0.1$ and $i_0 = 0.5$ are almost equal, since the particle needs more than one complete oscillation (for both slopes $\tau \simeq \mathrm{T}_p + 3\mathrm{T}_p/4$) to escape from the left potential barrier.

Setting $i_0 = 0.9$, the dynamic RA is just hinted and only the minimum around $\omega_{dRA}^{0.9} \simeq 1.6$, corresponding to a highly sloping potential, is evident. For high potential slopes, trapping phenomena at high frequencies are still present. Specifically they appear for frequencies larger than the following threshold values: $\omega_{thr}^{0.5} \simeq 1.2$ and $\omega_{thr}^{0.9} \simeq 2.4$. Increasing the value of the bias current, the right potential barrier decreases. As a consequence, trapping phenomena can occur only if the potential oscillates at higher frequencies. Furthermore, the parabolic approximation (linearization of the potential at the bottom of the well) used to calculate the plasma frequency (see Eq. (4.4)) fails for a highly tilted potential.

In all panels of Fig. 4.3 the presence of another noise induced effect, known as *noise enhanced stability* (NES) [4, 10, 54–58, 133–141] can be noted. Indeed the curves of τ *vs* γ are characterized by a nonmonotonic behavior with the presence of a maximum.More in detail, can be noted that the τ *vs* γ behaviour shows the presence of NES for any frequency taken in an interval around the different frequencies $\omega_{dRA}^{i_0}$. This suggests that the origin of this nonmonotonic effect can lie in the resonance phenomenon, involving the plasma frequency, previously discussed about the RA effect. Specifically, for $i_0 = 0.0$ this effect occurs for $\omega_{NES} \in [0.43 - 0.87]$. For each value $i_0 = 0.1, 0.5$ of the bias current, there are two $\omega_{dRA}^{i_0}$ frequencies and, correspondingly, two different ranges of frequencies giving evidence of NES effects.
In detail: $\omega_{NES}^{(1)} \in [0.42 - 0.78]$ and $\omega_{NES}^{(2)} \in [0.84 - 1.02]$ for $i_0 = 0.1$, and $\omega_{NES}^{(1)} \in [0.24 - 0.77]$ and $\omega_{NES}^{(2)} \in [0.97 - 1.14]$ for $i_0 = 0.5$.
Using highly tilted potential, i.e. $i_0 = 0.9$, there is only one RA minimum and, according

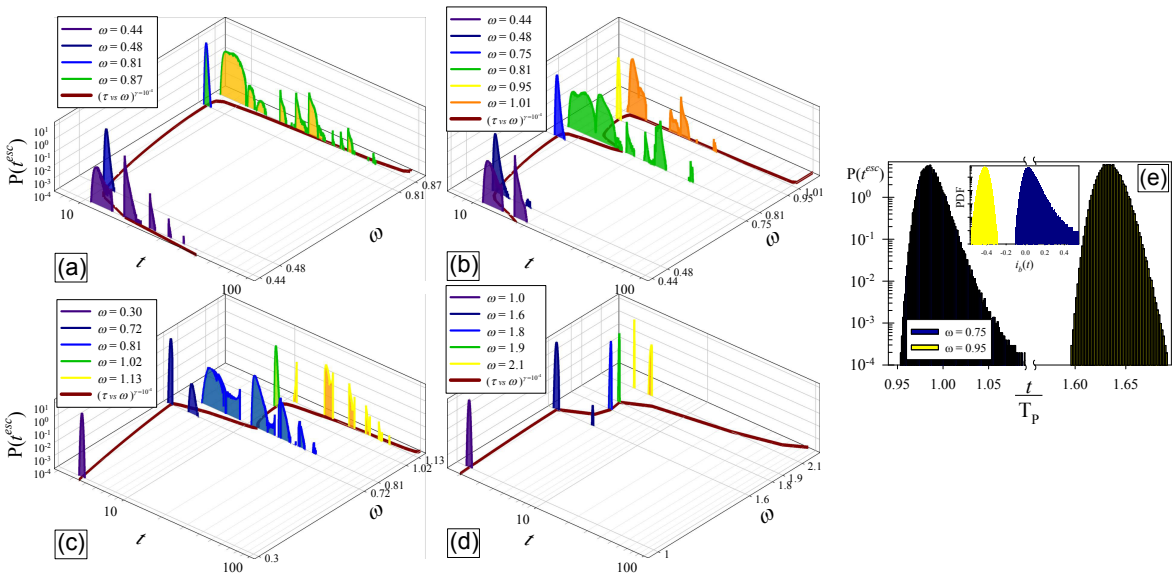

Figure 4.7: Panels a, b, c and d: PDFs as a function of the time t, varying ω. Every picture is obatined fixing the values of $\gamma = 10^{-4}$, $\tau_c = 0$ and $i_0 = \{\mathrm{a}i_0 = 0,\ \mathrm{b}i_0 = 0.1,\ \mathrm{c}i_0 = 0.5,\ \mathrm{d}i_0 = 0.9\}$. The MFPT *versus* ω curves corresponding to the dynamic RA effects (see solid lines in Fig. 4.4) are also shown. The PDF and t axes are logarithmic. Panel e: Semi-log plot of the PDFs as a function of the time t, normalized to the washboard oscillation period T_p, setting $i_0 = 0.1$ and $\omega = \omega_{dRA}^{0.1} = \{0.75, 0.95\}$. The inset shows the same PDF data in function of the bias current $i_b(t)$.

to the correspondence previously observed, only one range of frequencies ($\omega_{NES} \in [0.4-2.4]$) for which the NES phenomenon is found. According to this analysis, the curves of Fig. 4.5, obtained for different values of the noise correlation time ($\tau_c = 0.0, 1.0, 5, 10,$) show the presence of NES for values of ω chosen in the intervals given above. In all curves, as τ_c increases, the maxima are shifted towards higher values of the noise intensity. Moreover, the MFPT values around the NES maxima tend to slightly reduce for low slopes (small values of i_0) of the oscillating potential (panels a, b and c of Fig. 4.5) and to increase for high slopes (panels d, e and f of the Fig. 4.5).

These features, i.e. the shift towards higher frequencies and modification in the maxima of MFPT for increasing values of τ_c, are present also in a conventional JJ. In Fig. 4.6, where $i_0 = 0.0$ and $\omega = 0.75$, it is possible to observe that for a normal JJ respect to a graphene junction:

- i) the NES maxima are broadener;
- ii) the phase particle remains confined in the potential well for longer time, i.e. the τ values are slightly higher;
- iii) the NES effect appears for lower noise intensities.

Conversely, the behaviors of normal and graphene JJs coincide for larger values of the noise intensity γ, since the specific potential profile becomes irrelevant due to the strength of random fluctuations.

4.4 Probability Density Functions

To deeply understand the behavior of the MFPT, I expand further the theoretical analysis discussing the PDFs of the switching times $P\left(t^{esc}\right)$. The distributions of the escape times is often studied in many unstable physical systems, in which noise enhanced

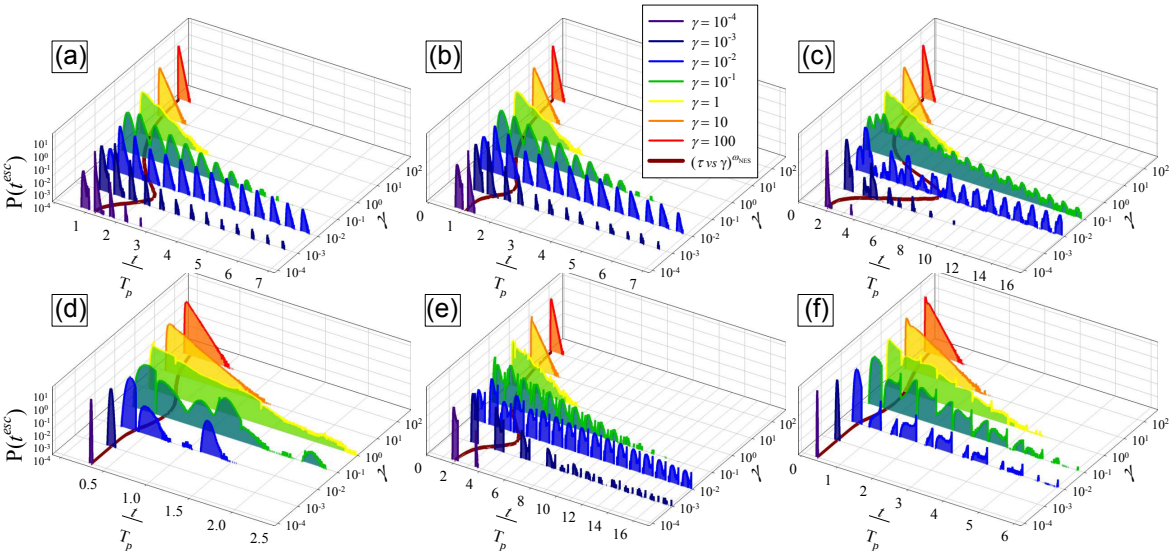

Figure 4.8: PDF as a function of the time t, normalized to the washboard oscillation period T_p, varying γ. Every picture is obatined fixing the values of ω, i_0 and $\tau_c = 0$. In detail: a $i_0 = 0$, $\omega = 0.44$; b $i_0 = 0.1$, $\omega = 0.44$; c $i_0 = 0.1$, $\omega = 1.0$; d $i_0 = 0.5$ and $\omega = 0.6$; e $i_0 = 0.5$, $\omega = 1.08$; f $i_0 = 0.9$, $\omega = 1.18$. Every picture shows also the MFPT *versus* γ curve corresponding to NES effect (see solid lines in Fig. 4.5) obtained using the same values for the other parameters. The PDF and γ axes are logarithmic. The legend in panel b refers to all pictures.

of stability [54] and resonant activation [123] are observed. The analisys of PDF data supports investigations in many frameworks, as financial market data [197–199], polimer dynamics [200, 201] and other biological systems [202].
The parameters of the system and noise source are set in such a way to put in evidence nonmonotonic effects in the MFPT data. Every PDF is constructed performing $N_{exp} = 10^7$ numerical realizations (experiments), and each curve is normalized to unity. Whenever possible, the time t was normalized to the oscillation period T_p. This allow to compare the passage times with the different slopes taken on by the potential during its oscialltory motion.

The panels a, b, c and d of Fig. 4.7 show $P(t^{esc})$ as a function of time t, for different values of the bias current $i_0 = \{$a) 0, b) 0.1, c) 0.5, d) 0.9$\}$. These results allow to explore the switching dynamics in correspondence of peculiar points of τ *vs* ω curves (see solid lines on the t-ω planes of Fig. 4.7 and in Fig. 4.4), calculated for $\gamma = 10^{-4}$. Setting $\omega = \omega_{dRA}^{i_0}$, the resonance-like dynamics results in single-peack PDFs, centered around the MFPT values. This suggests that, in all numerical realizations, the phase particle tends to follow almost the same trajectory to escape from the initial metastable state. In particular, the panel e of Fig. 4.7 shows the PDF calculated setting $\omega = \omega_{dRA}^{0.1} = \{0.75, 0.95\}$, as a function of the normalized time t/T_p. As already noted, setting $\omega = 0.75$, that is the value corresponding to the first dynamic RA minimum, the particle tends to escape through the right barrier after almost one oscillation of the washboard potential. Conversely, setting $\omega = 0.95$, that is in correspondence of the second dynamic RA minimum, the left-side escapes occur when $t \simeq 1.6T_p$. These peaks show asymmetry and fat tails. The asymmetry is more pronunced in low frequency data, because the time that the washboard spends in the configurations supporting the escape events get longer reducing the oscillation frequency. The inset in the panel e of Fig. 4.7 shows the PDFs plotted as a function of the bias current $i_b(t)$ to compare, at least qualitatively, these data with the switching current probability $P(I_c)$, often studied in the JJ framework. The shape of these single peak PDFs recalls the thermally

activated switching current distribution in SGS systems (see Refs. [16, 190]). The PDFs for frequencies within the dynamic RA minima are still formed by single peaks, but tend to broaden moving from $\omega = \omega_{dRA}$ (see panels a and b of Fig. 4.7). Far from these frequencies, that is when the τ values grow, the PDFs show multi-peaks structures, suggesting that the trajectories followed by the phase particle in the various experiments are very different from each other. This occurs also for $\omega = 0.81$ and $i_0 = \{0.1, 0.5\}$, that is in correspondence of the narrow maximum located beetwen the two RA minima (see panels b and c). In high frequency experiments, trapping phenomena occurs. In particular, for $i_0 = 0$ and $\omega = 0.87$ almost 21% of the experiments give entrapment, whereas for $i_0 = 0.1$ and $\omega = 1.01$ this occurs in $\sim 2\%$ of the experiments. Increasing i_0, the width of the peaks reduces, but the multi-peak structures in high frequency PDFs are still evident as well as the trapping phenomena. In detail, setting $i_0 = 5$ and $\omega = 1.13$, the probability that the phase particle undergoes a trapping is $\sim 4\%$, and for $i_0 = 9$ and $\omega = 2.1$ is $\sim 23\%$. Panels a - f of Fig. 4.8 show $P\left(t^{esc}\right)$ as a function of the normalized time t/T_p obtained setting system and noise parameters in analogy with those set in panels a - f of Fig. 4.5, that is: panel a $i_0 = 0$, $\omega = 0.44$, panel b $i_0 = 0.1$, $\omega = 0.44$, panel c $i_0 = 0.1$, $\omega = 1.0$, panel d $i_0 = 0.5$ and $\omega = 0.6$, panel e $i_0 = 0.5$, $\omega = 1.08$ and panel f $i_0 = 0.9$, $\omega = 1.18$. These PDFs allow to explore the NES effects put in evidence in Fig. 4.5 (see solid curves on the t-ω plane of panels of Fig. 4.8). The creation of NES maxima is due to the possibility that random fluctuations confine the particle inside the well, also when the washboard is in optimal configurations for escape events. In correspondence of the NES maxima, the PDFs are composed by long regular sequences of sharp peaks with decreasing amplitude. Multi-peak distributions of escape times with exponentially decaying envelopes characterize other experimental analises [54].
For small potential slopes (see panels a, b and c) the peaks have exponential decay and are well spaced. For $\gamma \leq 10^{-1}$ these sequences are formed by two peaks per period, corresponding to right- and left-side escapes. Increasing the noise amplitude, that is for $\gamma \geq 1$, the peaks tend to get lower and broaden, up to merge into a larger single distribution. The low frequency PDFs (panels a, b and d) for $\gamma = 1$, 10 and 100 show peaks spreading over almost 2, 1 and 0.5 periods, respectively. In higher frequency PDFs (panels c, e and f) the width of these peak is twice, that is they spread over almost 4, 2 and 1 periods for $\gamma = 1$, 10 and 100, respectively. The PDFs in the panel d don't show regularity because, the potential is very sloped and its frequency is not enough to cause the particle staying in the intial state for long time. Panels e and f regard again highly tilted potentials, but the frequency is high enough to trap for long times the phase particle inside the initial well, generating interesting periodic peak structures. Every period contains two peaks, the first one narrow, due to the right-side escapes, the second one strongly asymmetric and wavy shaped, representing the left-side escapes (in panel e the two peaks are so close to appear as one).

4.5 Conclusions

I explored the influence of thermal fluctuations on the behavior of a ballistic graphene-based Josephson junction in the short-junction regime. In particular, I analyzed how random fluctuations affect the lifetime of the superconductive state in an underdamped current-biased JJ. The analysis was performed within the framework of the resistively and capacitively shunted junction (RCSJ) model, using a proper non-sinusoidal current-phase relation, characteristic of graphene. Specifically I investigated the mean first passage time (MFPT) of the phase particle, i.e. the phase difference across the junction, initially placed in a minimum of the tilted washboard-like potential. In particular, I studied the

MFPT as a function of different parameters of the system and external perturbations, i.e. Gaussianly distributed random fluctuations and periodical driving signal. I found nonmonotonic behavior of the lifetime, τ, of the superconductive state as a function of the noise intensity γ, driving frequency ω and fixing the initial value of the bias current i_0. These results indicate the presence of noise induced phenomena, such as *stochastic resonant activation* (RA) and *noise enhanced stability* (NES) with different features, strongly depending on the initial value, i_0, of the bias current. In particular, I observed ranges of parameters in which MFPT show evidence of *dynamic* and *stochastic* RA, including a multi-minimum RA effect in the low-noise-intensity regime. Finally, I observed changes in the behaviour of MFPT, when the white noise source is replaced by a coloured noise source with different values of the correlation time τ_c. The study is integrated by the probability density function analisys of the escape times, to relate the MFPT behavior with the trajectories covered by the phase particles to escape from the metastable state.

Our study provides information on the role played by random (both thermal and correlated) fluctuations in the switching dynamics from the superconductive state to the resistive one of a graphene-based JJ. The results obtained can help to better understand the role of fluctuations in the electrodynamics of new generation graphene-based superconductive devices, such as Josephson junctions, Josephson sensors, dc-SQUIDs and gate-tunable phase qubits, contributing to improve their performances.

In conclusion this work, which is well placed in the framework of the nonequilibrium statistical mechanics, due to the presence of an emerging material, such as graphene, with unique electrical properties, presents relevant and interesting results from several points of view.

Chapter 5

Conclusions

The macroscopic quantities that can be experimentally measured in Josephson junctions are directly related to their microscopic order parameter φ. Thus, the study the dynamics of φ allows us to study the electrodynamics of the junction. The order parameter can be depicted as a "phase particle" in a metastable state. The permanence or the escape from this metastable state defines the superconducting properties of the system. This work sheds light on the phase dynamics of two kind of Josephson junction (JJ): a long-overlap JJ and a graphene-based JJ. This work can be divided in three principal sections: an analysis of the effects of Gaussian and non-Gaussian noise sources on the mean lifetime of the superconducting state in long JJ, the investigation of a method to generate and identify breathers in properly excited long JJ and the study of a particular type of junction, composed by two superconducting electrodes suspended on a graphene layer.

The influence of both thermal fluctuations and external non-Gaussian noise sources on the temporal characteristics of long-overlap JJs was investigated. Different α-stable (or Lévy) distributions affecting the superconducting lifetime of long current-biased Josephson junctions are considered. The study is developed within the framework of the sine-Gordon equation. Specifically, the mean switching time (MST) of the phase difference across the junction, from a minimum of the tilted washboard potential, as a function of different parameters of the system and external random and periodical driving signals, is analyzed. Nonmonotonic behaviors of the superconducting lifetime τ as a function of noise intensity γ, driving frequency ω and junction length L are found. In particular, it is observed that the behaviour of the MST is affected by noise induced phenomena such as *stochastic resonant activation* and *noise enhanced stability*, with different characteristics depending on both the bias current distribution along the junction and the length of the superconducting device. The analysis of the MST as a function of the junction length reveales that the *soliton dynamics* plays a crucial role in the switching dynamics from the superconducting to resistive state. In more detail, the relation between creation and propagation of solitons and different features of the mean switching time is studied. This analysis has demonstrated the existence of two different dynamical regimes. One, occurring for short junction, is characterized by the movement of the phase string as a whole. The latter, occurring for junctions whose size exceeds a critical length, in which the kink (or antikink) creation is allowed. Finally, choosing an inhomogeneous distribution of the bias current along the junction, the cells located at the junction edges behave as generators of solitons. In these conditions the escape from the metastable superconducting state is strongly affected by the soliton dynamics. The contemporaneous presence of Cauchy-Lorentz and thermal noise sources induces modifications in the soliton dynamics and noise induced effects observed in the transient dynamics of JJs in the presence of non-Gaussian noise sources. Besides oscillating pairs

of soliton-antisoliton (*breathers*) induced by the noise have been observed.

The results of this work, which are important to understand the physics of the fluctuations in long-overlap Josephson junctions to improve the performance of these devices, can shed light on the general context of the nonequilibrium statistical mechanics. In fact, JJs are good candidates for probing relevant physics issues in metastable systems [8]. Moreover, the mean switching time from one of the metastable states of the potential profile encodes information on the non-Gaussian background noise. Therefore, the statistical analysis of the switching times of JJs can be used to analyze weak signals in the presence of an unknown non-Gaussian background noise.

The breathers generation and their propagation in a long JJ externally irradiated by a suitable excitation, as a function of the maximum amplitude A and the frequency ω of the exciting signal, is studied. The analysis is computationally developed in the framework of the damped and biased continuous sine-Gordon equation, using a sinusoidal pulse with amplitude $A(t)$ smoothly increasing/reducing during the switching on/off regimes of the pulse, according to Gaussian profiles. To include the environmental influence, a Gaussian white noise source is inserted into the model. Follow the Geniet and Leon results [12] about the nonlinear supratransmission (NST) in a discrete sine-Gordon chain, different kinds of *bifurcation diagrams* are constructed, plotting the dispersion of the phase values, of a references cell, and the energy injected into the system as a function of A and ω. These diagrams clearly shows in (A, ω) parameters space the presence of an area in which no energy flows into the medium, that is without NST, while in the rest of the (A, ω) space the energy is allowed to travel through the junction by means of SG nonlinear excitations: kinks, antikinks, breathers and plasma waves. When NST occurs, a new peculiar localization of the breathers in (A, ω) *branches* is evident. The density of these breathers-branches on a (A, ω) parametric space is strongly dependent on the duration of the pulse, the applied bias current and the damping of the system. Increasing the pulse duration more energy is pumped into the system and the energetic conditions that are necessary to excite a breather, are hardly satisfied. Therefore, breather-branches tend to disappear increasing the pulse duration. Similarly, increasing the applied bias current the breather-branches tend to vanish, because the current stretchs a breather up to split it into a kink-antikink couple. The damping parameter has also to carefully set, because while an appropriate value favors the breathers formation a too high damping value rapidly annihilate generated breathers. The deterministic analysis is improved including a white noise contribute, to evaluate the percentage of breathers resistent to thermal effects. Combinations of (A, ω) values exists,for which breathers are created with high probability, despite of the noise influence.

This study fills the void left by the absolute lack of experimental works devoted to the breathers detection in long JJ. Many impediments affect their detection, from the difficulty in efficently generating and trapping them, to the lack of macroscopic experimental evidence of breathers motion in a junction (neither sign on the I-V characteristic or magnetic flux associated with them). The detection of breathers mode in a LJJ is an open challenge in the context of the long junctions.

The influence of thermal fluctuations on the behavior of a ballistic graphene-based Josephson junction in the short-junction regime is explored. In particular, the analysis was performed within the framework of the resistively and capacitively shunted junction model, using a proper non-sinusoidal current-phase relation which is characteristic of graphene. Specifically, the mean first passage time (MFPT) of the phase particle as a function of different parameters of the system and external perturbations, i.e. Gaussianly distributed random fluctuations and periodical driving signal, is studied. Nonmonotonic behaviors of the lifetime of the superconductive state appear as a function of the noise intensity γ, driving frequency ω and fixing the initial value of the bias current i_0. These

results indicate the presence of noise induced phenomena, such as *resonant activation* (RA) and *noise enhanced stability* (NES) with different features, strongly depending on the initial value, i_0, of the bias current. In particular, we observed ranges of parameters in which MFPT show evidences of *dynamic* and *stochastic* RA, including a multi-minimum RA effect in the low-noise-intensity regime. Finally, changes in the behaviour of MFPT are observed when the white noise source is replaced by a coloured noise source with different values of the correlation time τ_c. The study is integrated by the probability density function analisys of the escape times, to relate the MFPT behavior with the trajectories covered by the phase particles to escape from the metastable state.
Our study provides information on the role played by random (both thermal and correlated) fluctuations in the switching dynamics from the superconductive state to the resistive state of a graphene-based JJ. The results obtained can help to better understand the role of fluctuations in the electrodynamics of new generation graphene-based superconductive devices, such as Josephson junctions, Josephson sensors, dc-SQUIDs and gate-tunable phase qubits, contributing to improve their performances.
In conclusion, this analysis, which is well placed in the framework of the nonequilibrium statistical mechanics, due to the presence of an emerging material, such as graphene, with unique electrical properties, presents relevant and interesting results from several points of view.

Appendices

Appendix A

Algorithm for the simulation of the α-stable distribution

A.1 Stable Variables and Distributions

Stable random variables follow the so-called α-stable distributions. These distributions are very important because, as stated by the Central Limit Theorem, they constitute the limiting laws of normalized sums of independent, identically distributed random variables. The stable distributions are described by their characteristic function $\phi(k)$, that is the Fourier transform of the distribution function $P(X)$ of the random variable X:

$$\log \phi(k) = \begin{cases} -\sigma^\alpha |k|^\alpha \{1 - i\beta \frac{k}{|k|} \tan \frac{\pi\alpha}{2}\} + i\mu k, & \alpha \neq 1 \\ -\sigma |k| \{1 + i\beta \frac{k}{|k|} \frac{2}{\pi} \log |k|\} + i\mu k, & \alpha = 1 \, . \end{cases} \tag{A.1}$$

where $\alpha \in (0, 2]$, $\beta \in [-1, 1]$, $\sigma > 0$ and $\mu \in R$. An α-stable distribution is denoted by $S_\alpha(\sigma, \beta, \mu)$. $X \sim S_\alpha(\sigma, \beta, \mu)$ indicate a random variable with distribution characterized by Lévy index, or characteristic exponent, α, scale parameter σ, asymmetry parameter, or skewness, β and location parameter μ. When $\sigma = 1$ and $\mu = 0$ the distribution is called standard stable. The probability density function $P(X)$ of stable random variables exist and are continuous. Only few of these distributions are known in closed form, they are reported in table A.1.

Distribution	α	β
Gaussian $S_2(\sigma, 0, \mu)$	2	0
Cauchy-Lorentz $S_1(\sigma, 0, \mu)$	1	0
Lévy-Smirnov $S_{1/2}(\sigma, 1, \mu)$	1/2	1
Lévy-Smirnov (reflected)$S_{1/2}(\sigma, -1, \mu)$	1/2	-1

Table A.1: Stable distributions and corresponding values of the characteristic parameters.

A.2 Simulation Algorithm

The computer simulation of α-standard stable variables is performed following the Chambers-Mallows-Stuck method [120]. The simulation of a random variable $X \sim S_\alpha(1, \beta, 0)$ with scaling parameter $\sigma = 1$ and location parameter $\mu = 0$ for $\alpha \in (0, 2]$ and $\beta \in [-1, 1]$, is obtained with the following steps:

- generate a random variable V uniformly distributed on $(-\frac{\pi}{2}, \frac{\pi}{2})$ and an independent exponential random variable W with mean 1;
- for $\alpha \neq 1$ compute

$$X = S_{\alpha,\beta} \times \frac{\sin(\alpha(V + B_{\alpha,\beta}))}{(cos(V))^{1/\alpha}} \times \left(\frac{cos(V - \alpha(V + B_{\alpha,\beta}))}{W} \right)^{\frac{(1-\alpha)}{\alpha}} \tag{A.2}$$

where:

$$B_{\alpha,\beta} = \frac{\arctan(\beta \tan \frac{\pi\alpha}{2})}{\alpha} \tag{A.3}$$

$$S_{\alpha,\beta} = \left(1 + \beta^2 \tan^2 \frac{\pi\alpha}{2}\right)^{\frac{1}{2\alpha}} \tag{A.4}$$

- for $\alpha = 1$ compute

$$X = \frac{2}{\pi} \left(\left(\frac{\pi}{2} + \beta V \right) \tan V - \beta \log \left(\frac{W \cos V}{\frac{\pi}{2} + \beta V} \right) \right) \tag{A.5}$$

Appendix B

Numerical solution of the sine-Gordon equation

The dynamics of Long Josephson junctions is described by the sine-Gordon equation. The sine-Gordon equation is a second-order partial differential equation:

$$\beta\varphi_{tt} + \varphi_t - \varphi_{xx} = i(x,t) - \sin\varphi. \tag{B.1}$$

with boundary conditions given by:

$$\varphi_x(0,t) = \varphi_x(L,t) \equiv \eta. \tag{B.2}$$

In what follow, $\eta = 0$ in equation (B.2). The numerical integration of equation (B.1) is performed using an implicit finite-difference method. In order to do this, first the long junction is divided into many small sections of length $\Delta x = h = L/N$, where N is the number of sections and L is the length of the junction. Then, the time was divided into many short time intervals $\Delta t = k = T/M$ where T and M are the observation time and the number of intervals, respectively. The partial derivative are approximated using the Euler formalism. The phase $\varphi(x,t)$ is denoted $\varphi_n^m = \varphi(nh, mk)$ where $x = nh$, $t = mk$, n and m are the discrete space and time index, respectively. The expression for the partial derivative of equation (B.1) are derived:

$$\begin{aligned}
\varphi_t &= \frac{1}{2k}(\varphi_n^{m+1} - \varphi_n^{m-1}) + O(k^2),\\
\varphi_x &= \frac{1}{2h}(\varphi_{n+1}^{m} - \varphi_{n-1}^{m}) + O(h^2),\\
\varphi_{tt} &= \frac{1}{k^2}(\varphi_n^{m+1} - 2\varphi_n^{m} + \varphi_n^{m-1}) + O(k^2),\\
\varphi_{xx} &= \frac{1}{2h^2}(\varphi_{n+1}^{m+1} - 2\varphi_n^{m+1} + \varphi_{n-1}^{m+1} + \varphi_{n+1}^{m-1} - 2\varphi_n^{m-1} + \varphi_{n-1}^{m-1}) + O(h^2 + k^2).
\end{aligned}$$

The ranges of variation of indexes n and m are $n = 1, 2, ...N$ and $m = 1, 2, ...M$. Neglecting the terms $O(k^2)$, $O(h^2)$, $O(h^2 + k^2)$ and substituting the expression for the partial derivative in the sine-Gordon equation (B.1), a system of equations is obtained under the variation of n and m:

$$\begin{aligned}
&c_1\varphi_{n+1}^{m+1} + c_2\varphi_n^{m+1} + c_1\varphi_{n-1}^{m+1} =\\
&= -c_1(\varphi_{n+1}^{m-1} + \varphi_{n-1}^{m-1}) + c_3\varphi_n^{m-1} \quad + \quad c_4\varphi_n^m + c_5(\sin\varphi_n^m - i(nh, mk)),
\end{aligned}$$

$$n = 1, 2, ...N, \qquad m = 1, 2, ...M,$$

where:

$$c_1 = -k^2, \quad c_2 = 2\beta h^2 + h^2 k + 2k^2,$$
$$c_3 = -2\beta h^2 + h^2 k - 2k^2, \quad c_4 = 4\beta h^2, \quad c_5 = 2h^2 k^2.$$

Using the derived expressions for the partial derivative, the boundary conditions B.2 are written in the form:

$$\begin{aligned} \frac{\varphi_2^m - \varphi_0^m}{2h} = 0, \quad for \quad \varphi_x(0,t) = 0, \\ \frac{\varphi_{N+1}^m - \varphi_{N-1}^m}{2h} = 0, \quad for \quad \varphi_x(L,t) = 0, \end{aligned} \tag{B.3}$$

where $x = 0$ corresponds to $n = 1$ and $x = L$ to $n = N$. From expressions B.3, it is derived:

$$\varphi_2^m = \varphi_0^m, \quad and \quad \varphi_{N+1}^m - \varphi_{N-1}^m. \tag{B.4}$$

The expressions of equations B.3 in correspondence of $n = 1$ and $n = N$ are obtained substituting the conditions B.4 in B.3:

$$\begin{aligned} for \quad n = 1, \quad 2c_1\varphi_2^{m+1} + c_2\varphi_1^{m+1} = \\ = -c_1(\varphi_2^{m-1} + \varphi_0^{m-1}) + c_3\varphi_1^{m-1} + c_4\varphi_1^m \quad + \quad c_5(\sin\varphi_1^m - i(nh, mk)), \\ for \quad n = N, \quad 2c_1\varphi_{N-1}^{m+1} + c_2\varphi_N^{m+1} = \\ = -c_1(\varphi_{N+1}^{m-1} + \varphi_{N-1}^{m-1}) + c_3\varphi_N^{m-1} + c_4\varphi_N^m \quad + \quad c_5(\sin\varphi_N^m - i(nh, mk)). \end{aligned} \tag{B.5}$$

To take into account the colored noise signals in the system B.3, an expression of the Ornstein-Uhlenbeck process in terms of finite increments was derived. The finite increment, $\Delta\zeta$, of the Ornstein-Uhlenbeck process (equation (4.17)) is written as:

$$\Delta\zeta = -\frac{\zeta(n,m)}{\tau_c}k - \frac{1}{\tau_c h\sqrt{2\gamma hk}}. \tag{B.6}$$

where τ_c and γ are the correlation time and the colored noise intensity, respectively. The expression for the Ornstein-Uhlenbeck process at the *m-th* time step is then given by:

$$\zeta(n,m) = \zeta(n,m-1) + \Delta\zeta. \tag{B.7}$$

Considering expressions B.6 and B.7, then and m range of variation, the system B.3 and the boundary conditions B.5 become:

$$\begin{aligned} for \quad n = 2, ...N-1, \quad m = 1, 2, ...M, \\ c_1\varphi_{n+1}^{m+1} + c_2\varphi_n^{m+1} + c_1\varphi_{n-1}^{m+1} = -c_1(\varphi_{n+1}^{m-1} + \varphi_{n-1}^{m-1}) + c_3\varphi_n^{m-1} + \\ c_4\varphi_n^m + c_5(\sin\varphi_n^m - i(nh, mk)) + 2h^2k^2\zeta(n,m)W, \\ for \quad n = 1, \quad m = 1, 2, ...M, \\ 2c_1\varphi_2^{m+1} + c_2\varphi_1^{m+1} = -c_1(\varphi_2^{m-1} + \varphi_0^{m-1}) + c_3\varphi_1^{m-1} + \\ c_4\varphi_1^m + c_5(\sin\varphi_1^m - i(nh, mk)) + 2h^2k^2\zeta(1,m)W, \\ for \quad n = N, \quad m = 1, 2, ...M, \\ 2c_1\varphi_{N-1}^{m+1} + c_2\varphi_N^{m+1} = -c_1(\varphi_{N+1}^{m-1} + \varphi_{N-1}^{m-1}) + c_3\varphi_N^{m-1} \\ +c_4\varphi_N^m + c_5(\sin\varphi_N^m - i(nh, mk)) + 2h^2k^2\zeta(N,m)W. \end{aligned} \tag{B.8}$$

where W represents a Wiener process with zero mean value and variance equal to one. Solving the system B.10 corresponds to calculate the values φ_n^{m+1} in each point $n = 1, 2...N$ at time $m+1$, with initial condition given by the values φ_n^m and φ_n^{m-1} where $n = 1, 2...N$. The matrix representing the system B.10 has non-zero elements only in the major, upper minor and lower minor diagonals. This tridiagonal matrix has a form given by:

$$\begin{Vmatrix} c_2 & 2c_1 & 0 & \dots & 0 \\ c_1 & c_2 & c_1 & \dots & 0 \\ \vdots & \ddots & \ddots & \ddots & \vdots \\ 0 & \dots & c_1 & c_2 & c_1 \\ 0 & \dots & 0 & 2c_1 & 2c_2 \end{Vmatrix} \begin{Vmatrix} \varphi_1^{m+1} \\ \varphi_2^{m+1} \\ \vdots \\ \varphi_{N-1}^{m+1} \\ \varphi_N^{m+1} \end{Vmatrix} = \begin{Vmatrix} A_1 \\ A_2 \\ \vdots \\ A_{N-1} \\ A_N \end{Vmatrix}, \tag{B.9}$$

where

$$\begin{aligned} A_n = -c_1(\varphi_{n+1}^{m-1} + \varphi_{n-1}^{m-1}) + c_3\varphi_n^{m-1} + \\ c_4\varphi_n^m + c_5(\sin\varphi_n^m - i(nh, mk)) + 2h^2k^2\zeta(n, m)W, \\ for \quad n = 2, ...N-1, \quad m = 1, 2, ...M, \end{aligned}$$

$$\begin{aligned} A_1 = -c_1(\varphi_2^{m-1} + \varphi_0^{m-1}) + c_3\varphi_1^{m-1} + \\ c_4\varphi_1^m + c_5(\sin\varphi_1^m - i(nh, mk)) + 2h^2k^2\zeta(1, m)W, \\ for \quad n = 1, \quad m = 1, 2, ...M, \end{aligned} \tag{B.10}$$

$$\begin{aligned} A_N = -c_1(\varphi_{N+1}^{m-1} + \varphi_{N-1}^{m-1}) + c_3\varphi_N^{m-1} \\ +c_4\varphi_N^m + c_5(\sin\varphi_N^m - i(nh, mk)) + 2h^2k^2\zeta(N, m)W. \\ for \quad n = N, \quad m = 1, 2, ...M. \end{aligned}$$

The system B.9 is solved using the tridiagonal algorithm that is a simplified form of Gaussian elimination. The solutions corresponds to the phase values, φ_n^{m+1}, calculated in each point x $(n = 1, 2...N)$ of the phase string at the time *m+1*. The initial conditions chosen in the simulation are $\varphi_n^m = \arcsin i_0$ and $\varphi_n^{m-1} = \arcsin i_0$ for $n = 1, 2...N$.

Appendix C

Current-phase relation and critical current in graphene

The principal steps to obtain a correct current phase relation for graphene based JJ are outlined hereafter [16, 186, 189]. The above considerations apply to short junction in sense of proximity effect, $L \ll \xi$, where ξ is the superconducting coherence length.

From thermodinamic considerations, the equilibrium Josephson current is related to the free energy F, knowing its dependences on the phase difference across the junction, according to the equation:

$$I_S(\varphi) = \frac{2e}{\hbar}\frac{dF}{d\varphi}. \tag{C.1}$$

Starting from the Bogolubov-de Gennes (BdG) approach, Bardeen *et al* [203] derived the expression for F:

$$F = -2T\sum_n ln\left[2\cosh\left(\frac{\varepsilon_n}{2T}\right)\right] + \int d^dr|\Delta|^2/V \tag{C.2}$$

resulting in a generalization of the formula used in BCS model, for the case $\Delta = const$. The sum over n have a correspondence on the free energy calculations for an ensamble of ferminons with energy ε_n. As in the Hartree-Fock approximation, this term counts the interation twice, so that the other term, $\int d^dr|\Delta|^2/V$ corrects this double counting. Differentiating Eq. C.2

$$I_S = -\frac{4e}{\hbar}\sum_{\varepsilon_n<\Delta}\frac{d\varepsilon_n}{d\varphi}\tanh\frac{\varepsilon_n}{2T} - \frac{8eT}{\hbar}\int_\Delta^\infty d\varepsilon\ ln\left[2\cosh\frac{\varepsilon}{2T}\right]\frac{d\rho}{d\varphi} \tag{C.3}$$

obtained considering that the bulk energy $\propto |\Delta|^2$ is independent of the phase φ. The sum over n was devided into:

- the sum over the discrete positive eigenvalues $\varepsilon_n(\varphi)$ $(n = 1, 2, ...)$ of BdG equations,
- the integration over the continuos spectrum with density of states $\rho(\varepsilon, \varphi)$.

Eq. contains a factor 2 taking into account the two valleys in graphene. The state with $\varepsilon > \Delta$ contribute to the Josephson current [204], but their contribute to I_S can be negleted respect the contribution coming from the Andreev bounds state, with energy below the gap $\varepsilon < \Delta$. Considering a supercondutor-graphene system, the Andreev levels can be found from the BdG equations, in the form [186]

$$[(ihv\boldsymbol{\sigma}\cdot\boldsymbol{\partial} - \mu)\otimes\tau_z]\,\vec{\psi} = \varepsilon\vec{\psi} \tag{C.4}$$

where $\vec{\psi}^T = (\psi_e, \psi_h)$ is the electron (hole) wave functionin a vector, dot product is defined as $\boldsymbol{\sigma} \cdot \boldsymbol{\partial} = \sigma_x \partial_x + \sigma_y \partial_y$, and the symbol $\otimes$ indicates direct matrices product between the isospin (σ) and the electron-hole space (τ).

Chemical potential μ is measured respect to the Dirac points, so that $\mu = 0$ corresponds to undoped graphene. At the SG interfaces, located in $\mathbf{r}_\pm = (\pm L/2, y)$, the electron-like and hole-like wavefunctions are related each other by Andreev processes. Mathematically this can be expressed as

$$\psi_h(\mathbf{r}_-) = U(\varepsilon)\,\psi_e(\mathbf{r}_-), \quad \psi_h(\mathbf{r}_+) = U^{-1}(\varepsilon)\,\psi_e(\mathbf{r}_+) \tag{C.5}$$

$$U(\varepsilon) = \exp(-i\varphi/2 + i\beta\sigma_x), \quad \beta = \arccos(\varepsilon/\Delta). \tag{C.6}$$

Assuming *hard wall boundary conditions* in the y-direction, the k_y-component of the particle wave vector become quantized $k_y = q_n = (n + 1/2)\pi/W$. From the Fourier trasfomation of Eq. C.4, the *dispersion relation for the Andreev levels* is

$$\cos\varphi = \left(\cos^2\chi + \frac{\sin^2\chi}{\cos^2\chi}\right)\cos 2\beta - \sin^2\chi\tan^2\gamma \tag{C.7}$$

where $\chi = kL$, $k = (\mu/\hbar v)\cos\gamma$, $\gamma = \arcsin(\hbar v q_n(\mu)$.

Considering

$$\varepsilon_n(\varphi) = \Delta\sqrt{1 - |t_n|^2\sin^2(\varphi/2)} \tag{C.8}$$

where $|t_n|^2$ is the transmission coefficent in the n^{th} transversal channel

$$|t_n|^2 = \frac{k_n^2}{k_n^2\cos(k_nL) + (\mu/\hbar v)^2\sin^2(k_nL)}, \qquad k_n = \sqrt{1 - |t_n|^2\sin^2(\varphi/2)}, \tag{C.9}$$

Eq. C.7 can be solved analitically.

At the Dirac point, $k_n \to iq_n$, all channels are evanescent, and

$$|t_n|^2 = \frac{1}{\cosh^2(q_nL)}. \tag{C.10}$$

Knowing Eq. C.8, Eq.C becomes [189]

$$I_S(\varphi) = \frac{e\Delta^2}{\hbar}\sum_{\varepsilon_n<\Delta}\frac{|t_n|^2\sin\varphi}{\varepsilon_n(\varphi)}\tanh\frac{\varepsilon_n(\varphi)}{2T}. \tag{C.11}$$

Close to the neutrality points, that is when $\mu \ll E_{Th}$, where $E_{Th} = \hbar v/L$ is the *Thouless energy*, Eq. C.10 is a good approximation for the transmission coefficent. Moreover, if $W \gg L$ the summation in Eq. C.11 can be replaced by an integration, that is $\sum_n \to \frac{W}{\pi L}\int_0^\infty dx$ with $q_nL \to x$. Using a dimensionless variable $z = \sqrt{1 - \sin^2(\varphi/2)/\cosh^2 x}$, the Eq. C.11 becomes:

$$I_S(\varphi) = \frac{2e\Delta_0(T)W}{\pi\hbar L}\int_{\cos(\varphi/2)}^1 dz\,\frac{\cos(\varphi/2)\tanh\frac{z\Delta_0(T)}{2T}}{\sqrt{z^2 - \cos^2(\varphi/2)}}. \tag{C.12}$$

The temperature dependence for the gap $|\Delta| = \Delta_0(T)$ for s-wave superconductors is:

$$\ln\frac{\Delta_0(0)}{\Delta_0(T)} = 2\sum_{n=1}^{\infty}(-1)^{n+1}K_0\left[n\frac{\Delta_0(T)}{k_BT}\right], \tag{C.13}$$

where $K_0(x)$ is the zero order Bessel function, $\Delta_0(0) = (e^\gamma/\pi)k_BT_c = 0.567k_BT_c$ and this γ is the Euler's constant. There is no analytical expression for the integral in Eq. C.12, except for the zero temperature limit [186, 205]:

$$I_S(\varphi) = \frac{e\Delta_0(0)W}{\pi\hbar L}\cos(\varphi/2)\ln\left(\frac{1+\sin(\varphi/2)}{1-\sin(\varphi/2)}\right). \tag{C.14}$$

This equation, calculated in the ballistic limit of graphene, coincides with the results of Kulik and Omelyanchuk for disordered SNS junction [205]. For the longer junctions case, $L \gg W$, all transmission are exponentially suppressed, $|t_n|^2 \approx e^{-q_nL}$, and the summation in C.11 reduces to a geometrical progression to the leading order in $|t_n|^2$, resulting in:

$$I_S(\varphi) = \frac{e\Delta}{\hbar}\tanh\left(\frac{\Delta}{2T}\right)e^{-\pi L/W}\sin\varphi = I_c(T)\sin\varphi. \tag{C.15}$$

Considering high doping, $E_{Th} \ll \mu \ll \Delta$, full expression for t_n is necessary to calculate $I_S(\varphi)$. In this case, there is no analytical expression for $I_S(\varphi)$ but the critical current can be estimates as:

$$I_C \simeq N_{ch}\frac{e\Delta}{\hbar}, \quad N_{ch} = \frac{\mu W}{\pi\hbar v} \tag{C.16}$$

where N_{ch} is the number of propagating transversal channel.

Bibliography

[1] A. Scott, *Encyclopedia of nonlinear science* (Routledge, 2004).

[2] W. Buckel and R. Kleiner, *Superconductivity: Fundamentals and Applications*, Physics (Wiley-VCH, 2004) p. 52.

[3] C. R. Doering and J. C. Gadoua, Physical review letters **69**, 2318 (1992).

[4] A. A. Dubkov, N. V. Agudov, and B. Spagnolo, Physical Review E **69**, 061103 (2004).

[5] A. V. Gordeeva, A. L. Pankratov, and B. Spagnolo, International Journal of Bifurcation and Chaos **18**, 2825 (2008).

[6] G. Augello, D. Valenti, A. L. Pankratov, and B. Spagnolo, The European Physical Journal B-Condensed Matter and Complex Systems **70**, 145 (2009).

[7] G. Augello, *Transient dynamics of short and long Josephson junction*, Ph.D. thesis, Universitá degli studi di Palermo, Palermo (2010).

[8] G. Sun, N. Dong, G. Mao, J. Chen, W. Xu, Z. Ji, L. Kang, P. Wu, Y. Yu, and D. Xing, Physical Review E **75**, 021107 (2007).

[9] C. Pan, X. Tan, Y. Yu, G. Sun, L. Kang, W. Xu, J. Chen, and P. Wu, Physical Review E **79**, 030104 (2009).

[10] D. Valenti, C. Guarcello, and B. Spagnolo, Physical Review B **89**, 214510 (2014).

[11] G. Augello, D. Valenti, and B. Spagnolo, The European Physical Journal B-Condensed Matter and Complex Systems **78**, 225 (2010).

[12] F. Geniet and J. Leon, Journal of Physics: Condensed Matter **15**, 2933 (2003).

[13] F. Geniet and J. Leon, Physical review letters **89**, 134102 (2002).

[14] B. Bodo, S. Morfu, P. Marquié, and B. Essimbi, Journal of Statistical Mechanics: Theory and Experiment **2009**, P01026 (2009).

[15] N. Mizuno, B. Nielsen, and X. Du, Nature communications **4** (2013).

[16] U. Coskun, M. Brenner, T. Hymel, V. Vakaryuk, A. Levchenko, and A. Bezryadin, Physical review letters **108**, 097003 (2012).

[17] X. Du, I. Skachko, and E. Y. Andrei, Physical Review B **77**, 184507 (2008).

[18] H. B. Heersche, P. Jarillo-Herrero, J. B. Oostinga, L. M. Vandersypen, and A. F. Morpurgo, Nature **446**, 56 (2007).

[19] C. English, D. Hamilton, C. Chialvo, I. Moraru, N. Mason, and D. Van Harlingen, arXiv preprint arXiv:1305.0327 (2013).

[20] F. Miao, W. Bao, H. Zhang, and C. N. Lau, Solid State Communications **149**, 1046 (2009).

[21] G. Wendin and V. Shumeiko, Low Temperature Physics **33**, 724 (2007).

[22] J. H. Kim, R. P. Dhungana, and K.-S. Park, Physical Review B **73**, 214506 (2006).

[23] A. Zorin, E. Tolkacheva, M. Khabipov, F.-I. Buchholz, and J. Niemeyer, Physical Review B **74**, 014508 (2006).

[24] A. Berkley, H. Xu, M. Gubrud, R. Ramos, J. Anderson, C. Lobb, and F. Wellstood, Physical Review B **68**, 060502 (2003).

[25] C. Wu, Y. Chou, W. Kuo, J. Chen, L. Wang, J. Chen, K. Chen, U. Sou, H. Yang, and J. Jeng, Nanotechnology **19**, 315304 (2008).

[26] E. Levenson-Falk, R. Vijay, N. Antler, and I. Siddiqi, Superconductor Science and Technology **26**, 055015 (2013).

[27] H. Grabert, Physical Review B **77**, 205315 (2008).

[28] D. Urban and H. Grabert, Physical Review B **79**, 113102 (2009).

[29] G. Filatrella and V. Pierro, Physical Review E **82**, 046712 (2010).

[30] P. Addesso, G. Filatrella, and V. Pierro, Physical Review E **85**, 016708 (2012).

[31] P. Reimann, C. Van den Broeck, H. Linke, P. Hänggi, J. Rubi, and A. Pérez-Madrid, Physical review letters **87**, 010602 (2001).

[32] A. A. Dubkov and B. Spagnolo, Physical Review E **72**, 041104 (2005).

[33] H. Xu, A. Berkley, R. Ramos, M. Gubrud, P. Johnson, F. Strauch, A. Dragt, J. Anderson, C. Lobb, and F. Wellstood, Physical Review B **71**, 064512 (2005).

[34] B. Huard, H. Pothier, N. O. Birge, D. Esteve, X. Waintal, and J. Ankerhold, Annalen der Physik **16**, 736 (2007).

[35] T. Novotnỳ, Journal of Statistical Mechanics: Theory and Experiment **2009**, P01050 (2009).

[36] Q. Le Masne, H. Pothier, N. O. Birge, C. Urbina, and D. Esteve, Physical review letters **102**, 067002 (2009).

[37] L. Billings, M. I. Dykman, and I. B. Schwartz, Physical Review E **78**, 051122 (2008).

[38] J. Peltonen, A. Timofeev, M. Meschke, T. Heikkilä, and J. Pekola, Physica E: Low-dimensional Systems and Nanostructures **40**, 111 (2007).

[39] J. Tobiska and Y. V. Nazarov, Physical review letters **93**, 106801 (2004).

[40] H. Grabert and U. Weiss, Physical review letters **53**, 1787 (1984).

[41] B. D. Josephson, Physics Letters **1**, 251 (1962).

[42] P. Anderson and J. Rowell, Physical Review Letters **10**, 230 (1963).

[43] A. Drozdov, M. Eremets, and I. Troyan, arXiv preprint arXiv:1412.0460 (2014).

[44] J. Bardeen, L. N. Cooper, and J. R. Schrieffer, Physical Review **108**, 1175 (1957).

[45] S. Shapiro, Physical Review Letters **11**, 80 (1963).

[46] N. Pedersen and A. Davidson, Applied Physics Letters **39**, 830 (1981).

[47] P. Bruzzone, Superconductor Science and Technology **10**, 919 (1997).

[48] R. Gross and A. Marx, "Applied superconductivity: Josephson effect and superconducting electronics," http://www.wmi.badw.de/teaching/Lecturenotes/AS/AS_Chapter2.pdf (2005).

[49] Y. Aharonov and D. Bohm, Physical Review **115**, 485 (1959).

[50] P. A. Lee and A. D. Stone, Physical review letters **55**, 1622 (1985).

[51] R. B. Laughlin, Physical Review B **23**, 5632 (1981).

[52] R. B. Laughlin, Physical Review Letters **50**, 1395 (1983).

[53] P. W. Anderson, Physical review **109**, 1492 (1958).

[54] R. Mantegna and B. Spagnolo, Phys. Rev. Lett. **76**, 563 (1996).

[55] N. Agudov and B. Spagnolo, Physical Review E **64**, 035102 (2001).

[56] A. Fiasconaro, B. Spagnolo, and S. Boccaletti, Physical Review E **72**, 061110 (2005).

[57] B. Spagnolo, N. Agudov, and A. Dubkov, Acta Phys. Pol. B **35**, 1419 (2004).

[58] B. Spagnolo, A. Dubkov, A. Pankratov, E. Pankratova, A. Fiasconaro, and A. Ochab-Marcinek, Acta Phys. Pol. B **38**, 1925 (2007).

[59] G. Augello, D. Valenti, and B. Spagnolo, International Journal of Quantum Information **6**, 801 (2008).

[60] K. Fedorov and A. Pankratov, Physical Review B **76**, 024504 (2007).

[61] K. Fedorov, A. L. Pankratov, and B. Spagnolo, International Journal of Bifurcation and Chaos **18**, 2857 (2008).

[62] A. Barone and G. Paterno, *Physics and applications of the Josephson effect* (Wiley, 1982).

[63] E. Montroll and M. Shlesinger, Nonequilibrium Phenomena II: From Stochastics to Hydrodynamics (1984).

[64] M. F. Shlesinger, G. M. Zaslavsky, and U. Frisch, in *Levy flights and related topics in Physics*, Vol. 450 (1995).

[65] B. Dybiec and E. Gudowska-Nowak, Physical Review E **69**, 016105 (2004).

[66] M. R. Souryal, E. G. Larsson, B. Peric, and B. R. Vojcic, Signal Processing, IEEE Transactions on **56**, 266 (2008).

[67] J. Ankerhold, Physical review letters **98**, 036601 (2007).

[68] E. V. Sukhorukov and A. N. Jordan, Physical review letters **98**, 136803 (2007).

[69] M. Köpke and J. Ankerhold, New Journal of Physics **15**, 043013 (2013).

[70] Y. Yu and S. Han, Physical review letters **91**, 127003 (2003).

[71] M. H. Devoret, J. M. Martinis, D. Esteve, and J. Clarke, Physical review letters **53**, 1260 (1984).

[72] M. H. Devoret, J. M. Martinis, and J. Clarke, Physical review letters **55**, 1908 (1985).

[73] M. Castellano, G. Torrioli, C. Cosmelli, A. Costantini, F. Chiarello, P. Carelli, G. Rotoli, M. Cirillo, and R. Kautz, Physical Review B **54**, 15417 (1996).

[74] S. Han, Y. Yu, X. Chu, S.-I. Chu, and Z. Wang, Science **293**, 1457 (2001).

[75] Y. Yu, Y. Zhang, W. Qiu, S. Li, S. Han, and Z. Wang, Superconductor Science and Technology **15**, 555 (2002).

[76] A. A. Dubkov, B. Spagnolo, and V. V. Uchaikin, International Journal of Bifurcation and Chaos **18**, 2649 (2008).

[77] P. Lomdahl, O. Soerensen, and P. L. Christiansen, Physical Review B **25**, 5737 (1982).

[78] Y. Zhang, D. Winkler, P.-Å. Nilsson, and T. Claeson, Physical Review B **51**, 8684 (1995).

[79] K. Likharev, Dynamics of Josephson Junctions and Circuits (1986).

[80] A. Ustinov, Physica D: Nonlinear Phenomena **123**, 315 (1998).

[81] M. Büttiker and R. Landauer, Physical Review A **23**, 1397 (1981).

[82] D. W. McLaughlin and A. C. Scott, Physical Review A **18**, 1652 (1978).

[83] B. Dueholm, E. Joergensen, O. Levring, R. Monaco, J. Mygind, N. Pedersen, and M. Samuelsen, Magnetics, IEEE Transactions on **19**, 1196 (1983).

[84] A. Abdumalikov Jr, M. Fistul, and A. Ustinov, Physical Review B **72**, 144526 (2005).

[85] J. Pfeiffer, M. Schuster, A. Abdumalikov Jr, and A. Ustinov, Physical review letters **96**, 034103 (2006).

[86] K. G. Fedorov, M. V. Fistul, and A. V. Ustinov, Physical Review B **84**, 014526 (2011).

[87] A. L. Pankratov, A. V. Gordeeva, and L. S. Kuzmin, Physical review letters **109**, 087003 (2012).

[88] M. A. García-Ñustes and J. A. González, Physical Review E **86**, 066602 (2012).

[89] J. H. Kim, B.-R. Ghimire, and H.-Y. Tsai, Physical Review B **85**, 134511 (2012).

[90] D. R. Gulevich, M. Gaifullin, and F. Kusmartsev, The European Physical Journal B-Condensed Matter and Complex Systems **85**, 1 (2012).

[91] J. Frenkel and T. Kontorova, Izv. Akad. Nauk, Ser. Fiz. **1**, 137 (1939).

[92] P. Caudrey, J. Gibbon, J. Eilbeck, and R. Bullough, Physical Review Letters **30**, 237 (1973).

[93] R. K. Bullough and P. J. Caudrey, *The soliton and its history* (Springer, 1980).

[94] R. Hirota, Journal of the Physical Society of Japan **33**, 1459 (1972).

[95] M. J. Ablowitz, D. J. Kaup, A. Newell, and H. Segur, Physical Review Letters **30**, 1262 (1973).

[96] G. Lamb Jr, Physics Letters A **48**, 73 (1974).

[97] G. C. Wick, Reviews of Modern Physics **27**, 339 (1955).

[98] M. Samuelsen and S. Vasenko, Journal of applied physics **57**, 110 (1985).

[99] W. Szajnowski and J. Wynne, Signal Processing Letters, IEEE **8**, 151 (2001).

[100] A. V. Chechkin, V. Y. Gonchar, J. Klafter, and R. Metzler, Advances in chemical physics **133**, 439 (2006).

[101] R. Metzler and J. Klafter, Physics reports **339**, 1 (2000).

[102] V. V. Uchaikin, Physics-Uspekhi **46**, 821 (2003).

[103] A. Dubkov, A. La Cognata, and B. Spagnolo, Journal of Statistical Mechanics: Theory and Experiment **2009**, P01002 (2009).

[104] B. J. West and W. Deering, Physics Reports **246**, 1 (1994).

[105] D. W. Sims, E. J. Southall, N. E. Humphries, G. C. Hays, C. J. Bradshaw, J. W. Pitchford, A. James, M. Z. Ahmed, A. S. Brierley, M. A. Hindell, *et al.*, Nature **451**, 1098 (2008).

[106] A. Reynolds, Ecology **89**, 2347 (2008).

[107] A. Reynolds, Journal of Physics A: Mathematical and Theoretical **42**, 434006 (2009).

[108] D. Brockmann, L. Hufnagel, and T. Geisel, Nature **439**, 462 (2006).

[109] R. N. Mantegna and H. E. Stanley, Nature **376**, 46 (1995).

[110] M. Shlesinger, Lecture Notes in Physics Vol. 450 (1971).

[111] P. D. Ditlevsen, Geophysical Research Letters **26**, 1441 (1999).

[112] W. A. Woyczynski, *Lévy Processes: Theory and Applications*, edited by O. E. Barndorff-Nielsen, T. Mikosch, and S. I. Resnick (Birkhauser, Boston, 2001, 2001) p. 241.

[113] J. Bertoin, Lévy Processes (1996).

[114] K. Sato, *Lévy processes and infinitely divisible distributions* (Cambridge university press, 1999).

[115] B. Gnedenko and A. Kolmogorov, Limit Distributions for Sums of Independent Random Variables (1954).

[116] M. Nußbaum, Biometrische Zeitschrift **17**, 126 (1975).

[117] A. Khintchine and P. Lévy, C. R. Acad. Sci. Paris **202** (1936).

[118] A. Ya. Khintchine, Limit Distributions for the Sum of Independent Random Variables (1938).

[119] W. Feller, Wiley series in probability and mathematical statistics. (1971).

[120] R. Weron, Statistics & Probability Letters **28**, 165 (1996).

[121] J. M. Chambers, C. L. Mallows, and B. Stuck, Journal of the American Statistical Association **71**, 340 (1976).

[122] A. N. Malakhov and A. L. Pankratov, Advances in Chemical Physics **121**, 357 (2002).

[123] R. N. Mantegna and B. Spagnolo, Physical review letters **84**, 3025 (2000).

[124] R. Mantegna and B. Spagnolo, Le Journal de Physique IV **8**, Pr6 (1998).

[125] P. Pechukas and P. Hänggi, Physical review letters **73**, 2772 (1994).

[126] M. Marchi, F. Marchesoni, L. Gammaitoni, E. Menichella-Saetta, and S. Santucci, Physical Review E **54**, 3479 (1996).

[127] B. Dybiec and E. Gudowska-Nowak, Journal of Statistical Mechanics: Theory and Experiment **2009**, P05004 (2009).

[128] S. Miyamoto, K. Nishiguchi, Y. Ono, K. M. Itoh, and A. Fujiwara, Physical Review B **82**, 033303 (2010).

[129] Y. Hasegawa and M. Arita, Physics Letters A **375**, 3450 (2011).

[130] A. Fiasconaro and B. Spagnolo, Physical Review E **83**, 041122 (2011).

[131] J. M. Martinis, M. H. Devoret, and J. Clarke, Physical Review B **35**, 4682 (1987).

[132] A. V. Gordeeva and A. L. Pankratov, Journal of Applied Physics **103**, 103913 (2008).

[133] P. D'Odorico, F. Laio, and L. Ridolfi, Proceedings of the National Academy of Sciences of the United States of America **102**, 10819 (2005).

[134] P. I. Hurtado, J. Marro, and P. Garrido, Physical Review E **74**, 050101 (2006).

[135] R. Mankin, E. Soika, A. Sauga, and A. Ainsaar, Physical Review E **77**, 051113 (2008).

[136] M. Yoshimoto, H. Shirahama, and S. Kurosawa, The Journal of chemical physics **129**, 014508 (2008).

[137] A. Fiasconaro and B. Spagnolo, Physical Review E **80**, 041110 (2009).

[138] M. Trapanese, Journal of Applied Physics **105**, 07D313 (2009).

[139] A. Fiasconaro, J. J. Mazo, and B. Spagnolo, Physical Review E **82**, 041120 (2010).

[140] J.-h. Li and J. Łuczka, Physical Review E **82**, 041104 (2010).

[141] A. A. Smirnov and A. L. Pankratov, Physical Review B **82**, 132405 (2010).

[142] H. A. Kramers, Physica **7**, 284 (1940).

[143] V. Mel'Nikov, Physics reports **209**, 1 (1991).

[144] P. Hänggi, P. Talkner, and M. Borkovec, Reviews of Modern Physics **62**, 251 (1990).

[145] J. Hirsch, B. Huberman, and D. Scalapino, Physical Review A **25**, 519 (1982).

[146] B. Spagnolo, A. Fiasconaro, *et al.*, Acta Physica Polonica B **43**, 1169 (2012).

[147] A. V. Chechkin, V. Y. Gonchar, J. Klafter, and R. Metzler, EPL (Europhysics Letters) **72**, 348 (2005).

[148] A. V. Chechkin, O. Y. Sliusarenko, R. Metzler, and J. Klafter, Physical Review E **75**, 041101 (2007).

[149] L. Brillouin, *Wave propagation in periodic structures: electric filters and crystal lattices* (McGraw-Hill, New York, 1946).

[150] W. Chen and D. Mills, Physical review letters **58**, 160 (1987).

[151] E. A. Ostrovskaya and Y. S. Kivshar, Physical review letters **90**, 160407 (2003).

[152] A. S. Desyatnikov, E. A. Ostrovskaya, Y. S. Kivshar, and C. Denz, Physical review letters **91**, 153902 (2003).

[153] P. J. Louis, E. A. Ostrovskaya, C. M. Savage, and Y. S. Kivshar, Physical Review A **67**, 013602 (2003).

[154] S. John and J. Wang, Physical review letters **64**, 2418 (1990).

[155] B. Essimbi and D. Jäger, Journal of Physics D: Applied Physics **39**, 390 (2006).

[156] M. Scalora, J. P. Dowling, C. M. Bowden, and M. J. Bloemer, Physical review letters **73**, 1368 (1994).

[157] J. Leon and A. Spire, Physics Letters A **327**, 474 (2004).

[158] D. Taverner, N. Broderick, D. Richardson, R. Laming, and M. Ibsen, Optics letters **23**, 328 (1998).

[159] J. Leon, Physics Letters A **319**, 130 (2003).

[160] J. Leon, Physical Review E **70**, 056604 (2004).

[161] R. Khomeriki, Physical review letters **92**, 063905 (2004).

[162] R. Khomeriki, S. Lepri, and S. Ruffo, Physical Review E **70**, 066626 (2004).

[163] B. Bodo, S. Morfu, P. Marquié, and M. Rosse, Electronics letters **46**, 123 (2010).

[164] J. Macías-Díaz and A. Puri, Physics Letters A **366**, 447 (2007).

[165] K. T. V. Koon, J. Leon, P. Marquie, and P. Tchofo-Dinda, Physical Review E **75**, 066604 (2007).

[166] P. Anghel-Vasilescu, J. Dorignac, F. Geniet, J. Leon, and M. Taki, Physical review letters **105**, 074101 (2010).

[167] P. Binder, D. Abraimov, A. Ustinov, S. Flach, and Y. Zolotaryuk, Physical review letters **84**, 745 (2000).

[168] P. Binder and A. Ustinov, Physical Review E **66**, 016603 (2002).

[169] A. Ustinov, in *Nonlinearity and Disorder: Theory and Applications* (Springer, 2001) pp. 173–187.

[170] M. Schuster, D. Abraimov, A. Zhuravel, and A. Ustinov, in *Proceedings of the Third Conference: Localization and Energy Transfer in Nonlinear Systems: June 17-21 2002, San Lorenzo de El Escorial, Madrid* (World Scientific, 2003) p. 344.

[171] K. Segall, P. Williams, O. Svitelskiy, D. Edwards, N. Zhelev, G. Brummer, and J. J. Mazo, Phys. Rev. B **90**, 064502 (2014).

[172] B. Bodo and S. Morfu, in *Noise and Fluctuations (ICNF), 2013 22nd International Conference on* (IEEE, 2013) pp. 1–4.

[173] P. Lomdahl, O. Olsen, and M. R. Samuelsen, Physical Review A **29**, 350 (1984).

[174] S. Johnson and A. Biswas, Communications in Theoretical Physics **59**, 664 (2013).

[175] K. S. Novoselov, A. K. Geim, S. Morozov, D. Jiang, Y. Zhang, S. Dubonos, I. Grigorieva, and A. Firsov, science **306**, 666 (2004).

[176] B. Uchoa and A. C. Neto, Physical review letters **98**, 146801 (2007).

[177] A. Fedorov, N. Verbitskiy, D. Haberer, C. Struzzi, L. Petaccia, D. Usachov, O. Vilkov, D. Vyalikh, J. Fink, M. Knupfer, *et al.*, Nature communications **5** (2014).

[178] C. Girit, V. Bouchiat, O. Naaman, Y. Zhang, M. Crommie, A. Zettl, and I. Siddiqi, Nano letters **9**, 198 (2009).

[179] Ç. Girit, V. Bouchiat, O. Naaman, Y. Zhang, M. Crommie, A. Zettl, and I. Siddiqi, physica status solidi (b) **246**, 2568 (2009).

[180] J. Voutilainen, M. A. Laakso, and T. T. Heikkilä, Journal of Applied Physics **107**, 064508 (2010).

[181] X. Du, D. E. Prober, H. Vora, and C. B. Mckitterick, Graphene and 2D Materials **1** (2014).

[182] A. C. Neto, F. Guinea, N. Peres, K. S. Novoselov, and A. K. Geim, Reviews of modern physics **81**, 109 (2009).

[183] C. Beenakker, Physical review letters **97**, 067007 (2006).

[184] M. Titov, A. Ossipov, and C. W. Beenakker, Physical Review B **75**, 045417 (2007).

[185] M. Maiti and K. Sengupta, Physical Review B **76**, 054513 (2007).

[186] M. Titov and C. W. Beenakker, Physical Review B **74**, 041401 (2006).

[187] J. G. Lambert, S. A. Carabello, and R. C. Ramos, Applied Superconductivity, IEEE Transactions on **21**, 734 (2011).

[188] D. Jeong, J.-H. Choi, G.-H. Lee, S. Jo, Y.-J. Doh, and H.-J. Lee, Physical Review B **83**, 094503 (2011).

[189] I. Hagymási, A. Kormányos, and J. Cserti, Physical Review B **82**, 134516 (2010).

[190] G.-H. Lee, D. Jeong, J.-H. Choi, Y.-J. Doh, and H.-J. Lee, Physical review letters **107**, 146605 (2011).

[191] J.-H. Choi, G.-H. Lee, S. Park, D. Jeong, J.-O. Lee, H.-S. Sim, Y.-J. Doh, and H.-J. Lee, Nature communications **4** (2013).

[192] P. G. De Gennes, *Superconductivity of Metals and Alloys* (Benjamin, New York, 1966).

[193] P. Brouwer and C. Beenakker, Chaos, Solitons Fractals **8**, 1249 (1997).

[194] J. Tworzydło, B. Trauzettel, M. Titov, A. Rycerz, and C. W. J. Beenakker, Phys. Rev. Lett. **96**, 246802 (2006).

[195] I. Hagymási, (private communication) (2014), the Fig.1(a) of the Ref. [189] shows data only for $T/T_c = 0, 0.53, 0.71$. The proof about the temperature-indipendent behavior of $i(\varphi)$ for $T/T_c \lesssim 0.25$ is the result of private communications with the author.

[196] C. W. Gardiner, *Handbook of Stochastic Methods* (Springer-Verlag, Berlin, 2004) p. 106.

[197] G. Bonanno, D. Valenti, and B. Spagnolo, The European Physical Journal B-Condensed Matter and Complex Systems **53**, 405 (2006).

[198] D. Valenti, B. Spagnolo, and G. Bonanno, Physica A: Statistical Mechanics and its Applications **382**, 311 (2007).

[199] G. Bonanno, D. Valenti, and B. Spagnolo, Phys. Rev. E **75**, 016106 (2007).

[200] N. Pizzolato, A. Fiasconaro, and B. Spagnolo, International Journal of Bifurcation and Chaos **18**, 2871 (2008).

[201] N. Pizzolato, A. Fiasconaro, D. P. Adorno, and B. Spagnolo, Physical biology **7**, 034001 (2010).

[202] B. Spagnolo, S. Spezia, L. Curcio, N. Pizzolato, A. Fiasconaro, D. Valenti, P. Lo Bue, E. Peri, and S. Colazza, The European Physical Journal B-Condensed Matter and Complex Systems **69**, 133 (2009).

[203] J. Bardeen, R. Kümmel, A. Jacobs, and L. Tewordt, Physical Review **187**, 556 (1969).

[204] A. Levchenko, A. Kamenev, and L. Glazman, Physical Review B **74**, 212509 (2006).

[205] I. Kulik and A. Omelyanchuk, JETP Lett **21**, 96 (1975).